Nanocoax Arrays for Sensing Devices

Author: Binod Rizal

Boston College

The Graduate School of Arts and Sciences

Department of Physics

Nanocoax Arrays for Sensing Devices

a dissertation by

BINOD RIZAL

submitted in partial fulfillment of the requirements

for the degree of

Doctor of Philosophy

August 2014

Nanocoax Arrays for Sensing Devices

By: Binod Rizal

Advisor: Prof. Michael J. Naughton

Abstract

We have adapted a nanocoax array architecture for high sensitivity, all-electronic, chemical and biological sensing. Arrays of nanocoaxes with various dielectric annuli were developed using polymer replicas of Si nanopillars made via soft lithography. These arrays were implemented in the development of two different kinds of chemical detectors. First, arrays of nanocoaxes constructed with different porosity dielectric annuli were employed to make capacitive detectors for gaseous molecules and to investigate the role of dielectric porosity in the sensitivity of the device. Second, arrays of nanocoaxes with partially hollowed annuli were used to fabricate three-dimensional electrochemical biosensors within which we studied the role of nanoscale gap between electrodes on device sensitivity. In addition, we have employed a molecular imprint technique to develop a non-conducting molecularly imprinted polymer thin film of thickness comparable to size of biomolecules as an “artificial antibody” architecture for the detection of biomolecules.

Acknowledgements

The present work could not have been brought to its present level of study without the help, guidance and support of many people. First, I would like to express my deep and sincere gratitude to my supervisor and mentor, Prof. Michael J. Naughton. His encouragement, guidance and support throughout my graduate studies enabled me to develop a deep and comprehensive understanding of the subject matter and to succeed in the great achievement of completing my dissertation. I would like to express my sincere thanks to Prof. Thomas C. Chiles for his great support and inspiration throughout this work.

I would like to thank committee members Prof. Cyril P. Opeil S. J. and Dr. Michael J. Burns for reviewing this dissertation. Many thanks go to Dr. Michael J. Burns and Dr. Timothy Connolly for their help during the experimental stages and teaching me several experimental techniques. Further, I thank Mr. Svet Simidjiyski for his assistance with many mechanical and electrical systems throughout the experiments. I also extend my thanks all the faculty members, staff members and graduate students of the physics department at Boston College.

I would not have found success in this thesis work without the skilled hands and efforts of the members of the cleanroom of Boston College. I am particularly grateful to Mr. Steve Shepard and Dr. Greg McMahon for their immense help and training for the fabrication of micro/nanodevices. I would like to thank Prof. Naughton's lab members Dr. T. Kirkpatrick, Dr. F. Ye, Dr. J. M. Merlo, Michelle M. Archibald, Jeff Naughton, Aaron Rose, Nathan Nesbitt, Chaobin Yang, Yitzi Calm, and Luke D'Imperio. My special thanks go to Michelle M. Archabild for her help in experimental works and Luke D'Imperio for initial grammatical corrections of this dissertation.

I owe my loving thanks to my wife Muna and daughter Bina for their love and support. I will always be indebted to my parents for keeping me in their thoughts and prayers to god and of their wishes for success and joy in my life. I dedicate this dissertation to them.

Table of Contents

List of Figures

Chapter 1

Chapter 2

Chapter 3

Chapter 4

Chapter 5

Chapter 1

Nanocoax

1.1 Introduction

A nanocoax is a nanoscopic analog of a conventional coaxial cable or wire that consists of a metallic core, a cylindrical dielectric sleeve, and a solid or braided cylindrical outer metal shield. Conventional coaxial wires have been used to transmit signals essentially since the mid-19th century [1,2]. The evolution of microelectronics technology, including the shrinking of devices and integrated circuit components, has included the miniaturization of coaxial structures to micro- and nanoscale dimensions. This reduction in the size of coaxial structures may offer advantages to existing technologies and benefit the exploration and development of new technologies. After the successful synthesis and characterization of nanoscale-structures including nanorods, wires, and tubes, there has been interest in the realization of multilayer, coaxial nanostructures such as nanocoaxes [3–9]. Different forms of nanocoaxial structures have been realized with various permutations between metals, semiconductors, and dielectrics for the core, shield, and annulus. This review focuses on nanocoax structures having a general metal – nonmetal – metal structure. That is, we consider coaxes that have annuli filled with any nonmetal, meaning solid, liquid, or gas, dielectric/insulator, or semiconductor. A nanocoax structure is created by adding these components, namely dielectric or semiconducting annulus and metallic shield, in a radial direction onto a metallic, or at least highly conducting, nanowire or nanopillar, which serves as the core of the structure, as shown in Figure 1.1.

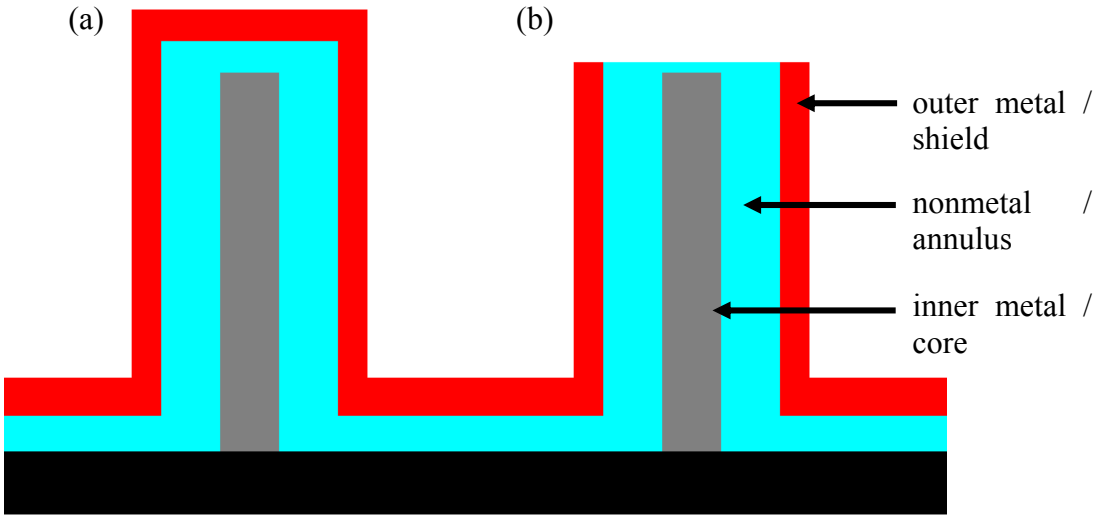

Figure 1.1 Illustration of different components of (a) a closed and (b) an open-ended nanocoax.

By combining the different nanoscale layers of materials with a common axis in a radial direction, electronic and optical devices possessing various interesting functions have been created.

Over the last decade, a number of studies have been completed that explore optical properties of nanoscale subwavelength structures and their fundamental applications, in order to understand near-field optics and to construct photonic devices [10–16]. Among the different subwavelength structures that have been analyzed, the nanocoax is of particular interest, as this structure is considered to have high transmittance to visible light and is a promising structure for deep-subwavelength, low-loss propagation of plasmonic and photonic radiation modes at optical and infrared frequencies [12,14,16]. The nanocoax geometry already has been employed in a variety of applications including photovoltaic (PV) solar cells, optical nanoantennas, negative index materials, and light-emitting fibers [17–31]. For example, the ability of a nanocoax to have its dielectric replaced with a semiconducting / PV material allows for the absorption or generation of light as it propagates along its axis, yet have photogenerated electrical current flow radially between the inner and outer metals. This allows, in principle, for increases in solar cell and photodiode efficiency [23–31]. In this structure, efficiency of transport (or collection of charge carriers) and absorption of light can be controlled by simply varying the radial thickness of the PV material and the height of the coax. Because the PV layer can be extremely thin and still absorb light, this structure is amenable to polymer and organic solar cells as well [30,31].

A nanocoax PV array can also have unique biological sensing applications. The architecture can potentially be used in a high resolution optoelectronic retinal prosthetic

system to provide electrical stimulation of the retina and produce visual percepts in blind or visually-impaired patients suffering from, e.g., macular degeneration or retinitis pigmentosa [32].Other optical phenomena, such as surface plasmons and electromagnetic oscillations at the interface between a dielectric and a conductor of a nanocoax, could make it possible to overcome the diffraction limit of light in the field of optical imaging [33].

The unique applications of the nanocoax are not necessarily due to new physical properties introduced by the structure. The large surface area and associated nanoscale gap between electrodes render possible some very useful applications in areas other than sensing, such as in energy storage devices. For example, because the capacitance of a capacitor depends on the surface area of its electrodes and the distance between them, a significant increase in capacitance of a capacitive storage device can be achieved by building arrays of densely-packed, high aspect ratio nanocoax-based dielectric capacitors, as the coaxial geometry optimizes both enabling parameters [34–36]. Similarly, in the case of electric double layer (EDL) capacitors, the capacitance is directly proportional to the effective surface area of its electrodes [37]. The surface area of the electrodes can be increased using a hollow or high-K dielectric nanocoax architecture that facilitates high capacity capacitors in a small volume. In other energy storage devices, such as batteries, the conversion and storage capacity depends upon chemical interactions that occur at the electrode-electrolyte interface and the transport of ions between electrodes. In such cases, beside the aforementioned effect of high electrode surface area, nanoscale structures can facilitate an increase in the transport rate of ions between electrodes, which can enhance the efficiency and cycling performance of the devices [38]. In such cases, beside the

aforementioned effect of high electrode surface area, nanoscale structures can facilitate an increase in the transport rate of ions between electrodes, which can enhance the efficiency and cycling performance of the devices.

The high surface area per unit volume makes the nanocoax structure a strong candidate for chemical and biological sensing applications and provides a way to scale the active sensing volume. The nanocoax structure renders possible spatially-resolved biological sensing because the size of an individual nanocoax is comparable to or smaller than that of many biological systems. A combination of 3D nanocoax structures and innovative signal transduction technologies can improve the limit of detection and sensitivity capabilities that exist in nanostructured sensors [39–41]. In particular, a nanocoax structure with a porous dielectric or partially hollow cavity annulus is emerging as a promising candidate for sensitive electrical, optical and electrochemical sensors [42–44].

We introduced the nanocoax structure and reviewed its potential application in optics, energy conversion and storage, and sensing devices. In this dissertation, we will be employing unique properties of the nanocoaxial structure for making miniaturized bio/chemical sensors. The fabrication of arrays of nanocoax structure using polymer nanopillars made via soft lithography will be discussed in Chapter 2 and details of sensing performances of the arrays will be discussed in Chapters 3, 4 and 5.

References

[1] W. Thomson, Philos. Mag. Ser. 4 **9**, 531 (1855).

[2] G. C. Leighton and D. R. Woodford, Am. Teleph. Telegr. Co. **47**, (1968).

[3] X. Huang, S. Neretina, and M. A. El-Sayed, Adv. Mater. **21**, 4880 (2009).

[4] L. J. Lauhon, M. S. Gudiksen, D. Wang, and C. M. Lieber, Nature **420**, 57 (2002).

[5] S. Barth, F. Hernandez-Ramirez, J. D. Holmes, and A. Romano-Rodriguez, Prog. Mater. Sci. **55**, 563 (2010).

[6] M. F. L. D. Volder, S. H. Tawfick, R. H. Baughman, and A. J. Hart, Science **339**, 535 (2013).

[7] T. Mikolajick, A. Heinzig, J. Trommer, S. Pregl, M. Grube, G. Cuniberti, and W. M. Weber, Phys. Status Solidi RRL – Rapid Res. Lett. **7**, 793 (2013).

[8] C. Zhang, Y. Yan, Y. S. Zhao, and J. Yao, Annu. Rep. Sect. C Phys. Chem. **109**, 211 (2013).

[9] K. Suenaga, Y. Zhang, and S. Iijima, Appl. Phys. Lett. **76**, 1564 (2000).

[10] F. I. Baida and D. Van Labeke, Phys. Rev. B **67**, 155314 (2003).

[11] J. A. Porto, F. J. García-Vidal, and J. B. Pendry, Phys. Rev. Lett. **83**, 2845 (1999).

[12] P. B. Catrysse and S. Fan, Appl. Phys. Lett. **94**, 231111 (2009).

[13] T. W. Ebbesen, H. J. Lezec, H. F. Ghaemi, T. Thio, and P. A. Wolff, Nature **391**, 667 (1998).

[14] J. Rybczynski, K. Kempa, A. Herczynski, Y. Wang, M. J. Naughton, Z. F. Ren, Z. P. Huang, D. Cai, and M. Giersig, Appl. Phys. Lett. **90**, 021104 (2007).

[15] A. A. E. Saleh and J. A. Dionne, Phys. Rev. B **85**, 045407 (2012).

[16] J. M. Merlo, F. Ye, B. Rizal, M. J. Burns, and M. J. Naughton, Opt. Express **22**, 14148 (2014).

[17] K. P. Lim, C. W. Lee, G. Singh, and Q. Wang, J. Nanophotonics **7**, 070598 (2013).

[18] A. Ndao, A. Belkhir, R. Salut, and F. I. Baida, Appl. Phys. Lett. **103**, 211901 (2013).

[19] S. P. Burgos, R. de Waele, A. Polman, and H. A. Atwater, Nat. Mater. **9**, 407 (2010).

[20] M. Iwanaga, N. Ikeda, and Y. Sugimoto, Phys. Rev. B **85**, 045427 (2012).

[21] R. de Waele, S. P. Burgos, A. Polman, and H. A. Atwater, Nano Lett. **9**, 2832 (2009).

[22] A. Weber-Bargioni, A. Schwartzberg, M. Cornaglia, A. Ismach, J. J. Urban, Y. Pang, R. Gordon, J. Bokor, M. B. Salmeron, D. F. Ogletree, P. Ashby, S. Cabrini, and P. J. Schuck, Nano Lett. **11**, 1201 (2011).

[23] R. E. Camacho, A. R. Morgan, M. C. Flores, T. A. McLeod, V. S. Kumsomboone, B. J. Mordecai, R. Bhattacharjea, W. Tong, B. K. Wagner, J. D. Flicker, S. P. Turano, and W. J. Ready, JOM **59**, 39 (2007).

[24] Y. Zhang, Wang, and A. Mascarenhas, Nano Lett. **7**, 1264 (2007).

[25] H. Zhou, A. Colli, A. Ahnood, Y. Yang, N. Rupesinghe, T. Butler, I. Haneef, P. Hiralal, A. Nathan, and G. A. J. Amaratunga, Adv. Mater. **21**, 3919 (2009).

[26] M. J. Naughton, K. Kempa, Z. F. Ren, Y. Gao, J. Rybczynski, N. Argenti, W. Gao, Y. Wang, Y. Peng, J. R. Naughton, G. McMahon, T. Paudel, Y. C. Lan, M. J. Burns, A. Shepard, M. Clary, C. Ballif, F.-J. Haug, T. Söderström, O. Cubero, and C. Eminian, Phys. Status Solidi RRL – Rapid Res. Lett. **4**, 181 (2010).

[27] T. Paudel, J. Rybczynski, Y. T. Gao, Y. C. Lan, Y. Peng, K. Kempa, M. J. Naughton, and Z. F. Ren, Phys. Status Solidi A **208**, 924 (2011).

[28] B. Weintraub, Y. Wei, and Z. L. Wang, Angew. Chem. Int. Ed. **48**, 8981 (2009).

[29] J. Kim, A. J. Hong, J.-W. Nah, B. Shin, F. M. Ross, and D. K. Sadana, ACS Nano **6**, 265 (2012).

[30] S. Kassegne, K. Moon, P. Martín-Ramos, M. Majzoub, G. Őzturk, K. Desai, M. Parikh, B. Nguyen, A. Khosla, and P. Chamorro-Posada, J. Micromechanics Microengineering **22**, 115015 (2012).

[31] H. Sun, H. Li, X. You, Z. Yang, J. Deng, L. Qiu, and H. Peng, J. Mater. Chem. A **2**, 345 (2013).

[32] M. J. Naughton, US8588920 B2 (19 November 2013).

[33] M. J. Naughton, K. J. Kempa, and Z. Ren, US7623746 B2 (24 November 2009).

[34] P. Banerjee, I. Perez, L. Henn-Lecordier, S. B. Lee, and G. W. Rubloff, Nat. Nanotechnol. **4**, 292 (2009).

[35] Z. Liu, Y. Zhan, G. Shi, S. Moldovan, M. Gharbi, L. Song, L. Ma, W. Gao, J. Huang, R. Vajtai, F. Banhart, P. Sharma, J. Lou, and P. M. Ajayan, Nat. Commun. **3**, 879 (2012).

[36] K. B. Shelimov, D. N. Davydov, and M. Moskovits, Appl. Phys. Lett. **77**, 1722 (2000).

[37] E. Frackowiak, Phys. Chem. Chem. Phys. **9**, 1774 (2007).

[38] P. G. Bruce, B. Scrosati, and J.-M. Tarascon, Angew. Chem. Int. Ed. **47**, 2930 (2008).

[39] G. Shen, P.-C. Chen, K. Ryu, and C. Zhou, J. Mater. Chem. **19**, 828 (2009).

[40] R. M. Penner, Annu. Rev. Anal. Chem. **5**, 461 (2012).

[41] J. Li, Y. Lu, Q. Ye, M. Cinke, J. Han, and M. Meyyappan, Nano Lett. **3**, 929 (2003).

[42] W. Kubo and S. Fujikawa, Nano Lett. **11**, 8 (2011).

[43] H. Zhao, B. Rizal, G. McMahon, H. Wang, P. Dhakal, T. Kirkpatrick, Z. Ren, T. C. Chiles, M. J. Naughton, and D. Cai, ACS Nano **6**, 3171 (2012).

[44] B. Rizal, M. M. Archibald, T. Connolly, S. Shepard, M. J. Burns, T. C. Chiles, and M. J. Naughton, Anal. Chem. **85**, 10040 (2013).

Chapter 2

Fabrication of Nanocoax

2.1 Introduction

Several approaches have been used for synthesizing nanostructures including nanotubes, nanowires and nanopillars [1–6]. Certain fabrication steps are then added to form multi-component nanocoax structures. The components of a nanocoax, namely the core, annulus and shield, are made by changing parameters, materials and methods during its fabrication process. In recent years, a number of technologies such as arc discharge, laser ablation, thermal evaporation, physical vapor deposition (PVD), plasma enhance chemical vapor deposition (PECVD), chemical vapor deposition (CVD), atomic layer deposition (ALD), focus ion beam (FIB), electrochemical deposition, and chemical synthesis have been used to make nanocoax structures. Here, the fabrication processes of nanocoaxes are categorized into two groups, template-free and templated methods, based on starting structures.

Template-free methods do not require any scaffold as the core of the coax structure itself provides the support for its other two layers, whereas in the template method, predefined nanostructures such as nanopores or nanopillars can be used as supportive templates for subsequent layers forming nanocoaxes.

In the case of template-free methods, Metallic nanowires and nanotubes can been used as cores of a nanocoax. Particularly, carbon fiber is one of the more commonly incorporated materials for core of nanocoax structures [7–11].

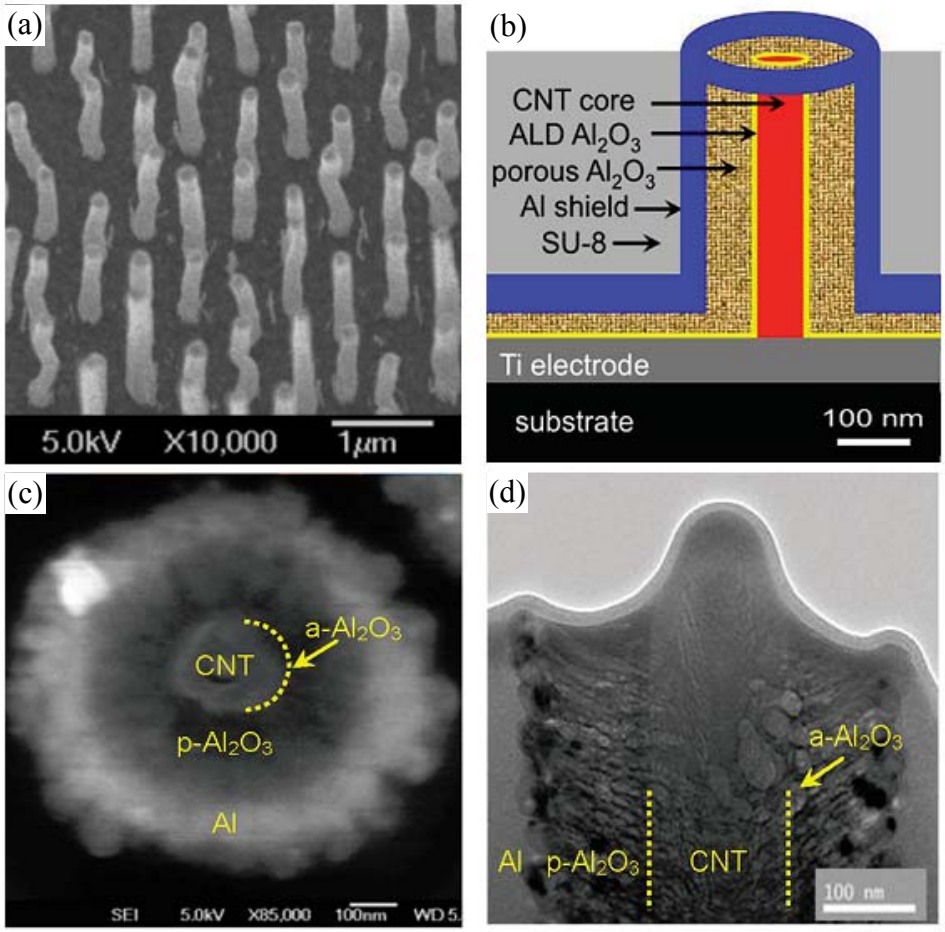

Figure 2.1.1(a) SEM image of CNTs used to fabricate nanocoax arrays. (b) Schematic of the cross-section of a nanocoax. (b) SEM image of top view of an open ended-nanocoax. (c) TEM image of cross-sectional view of a nanocoaxial capacitor with ~150 nm diameter inner electrode of CNT, ~ 10 nm and ~100 nm thick layers of nonporous (a-Al_2O_3) and porous (p-Al_2O_3) alumina, respectively and ~ 250 nm thick outer electrode of Al. From [10].

Initially, to make arrays of nanocoax, we also used arrays of vertically align carbon nanotubes (CNT) as shown in Figure 2.1.1 (a). To fabricate arrays of the nanocoax, we deposited Al_2O_3 and Al layers on the CNT array. We often removed the top end of the coax to make an open-ended nanocoax structure depending on how it was to be used as a sensing device. Figures 2.1 (b)-(d) show the schematic, scanning electron microscope (SEM) and transmission electron microscopy (TEM) images of single nanocoax from arrays identical open-eneded CNT-Al_2O_3-Al [10]. While the vertically align CNT has been employed in different fields [10,12–14], its synthesis process is laborious and time-consuming [6]. The CNT arrays have a honeycomb (kagome) pattern, rather than the optimal hexagonal close packed pattern. Moreover, the alignment of the CNTs was not straight as shown in Figure 2.1.1 (a). This results in low yields of the fabrication process of nanocoax arrays, especially in case of hollow cavity nanocoax arrays. In order to increase the density and improve the reproducibility and alignment issues associated with CNT-based fabrication process, we have used hexagonal close-packed polymer (SU-8) nanopillar arrays to make arrays of nanocoax [15]. The nanopillar arrays of polymer were made using soft lithography technique [5].

2.2 Soft Lithography

Soft Lithography (SL) is an unconventional, but one of the most convenient and economical, ways of fabricating different nonreentrant nanopatterns with feature sizes ranging from nanometers to micrometers [16]. The principle of SL processes is quite simple, making it a promising technology for high throughput nanoscale pattering such as roll-to-roll fabrication.

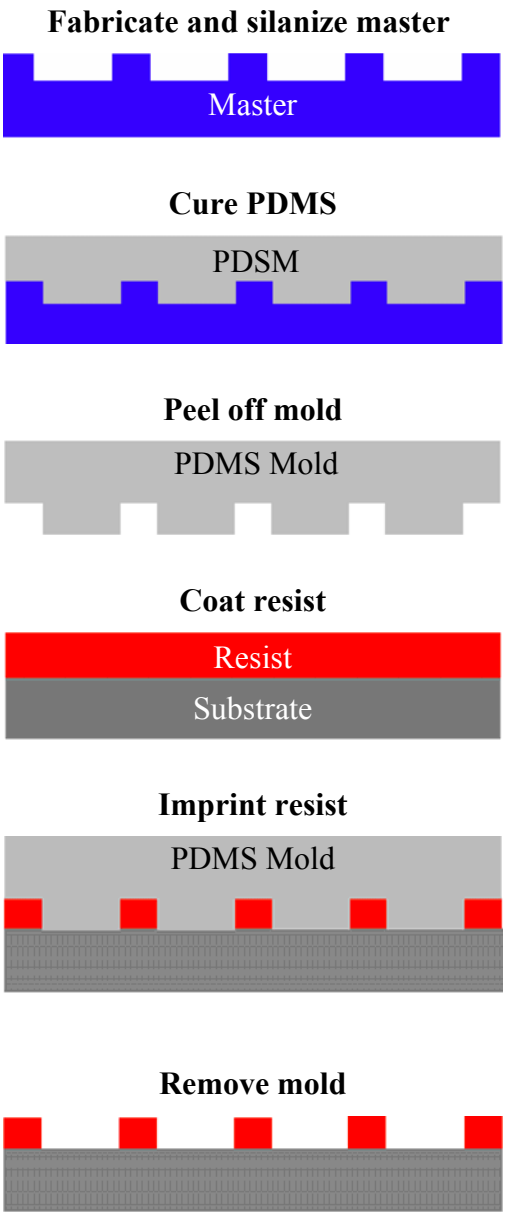

Figure 2.2.1 Schematic of steps in soft lithography.

Figure 2.2.1 shows schematics of SL technique. SL processes use a mold made from a material with small Young's modulus (~1 MPa), such as poly(dimethylsiloxane) (PDMS), but can also be a metal with a large modulus like Ni (~200GPa), which is often done in manufacturing situations, and that contains three-dimensional nanoscale features on its surface to emboss into a soft polymer material cast on a substrate under controlled temperature and pressure conditions. A SL mold is generally prepared by photo-chemically or thermally curing a monomer onto a master template, or by electroplating a metal onto a master template. The master is typically made using photolithography or electron-beam lithography. Here, we employ the SL technique to make polymeric (SU-8) replicas of silicon nanopillar (SiNP) arrays.

2.2.1 Preparation of Master

In this work, a Si substrate with arrays of NP on its surface was used as a SL master. The master was prepared by a combination of thermal oxidation and reactive ion etching of silicon substrates that were photolithographically patterned. Typical SiNP dimensions were 2 μm height and 200 nm diameter, in hexagonal close-packed arrays with periodicity/pitch between 0.9 and 1.5 μm, on substrates containing 10 x 20 mm^2 areas of Silicon nanopillar (SiNP) arrays. Different shaped pillars such as vertical, conical and sloped cross-section pillars were prepared with similar average dimensions were provided to Boston College by Solasta, Inc. Pillar arrays obtained were not directly used as masters for the SL technique. Instead, piranha cleaning was used to first clean the arrays. For the cleaning, SiNP arrays were exposed to a 3:1 (by volume) mixture of sulfuric acid (96%) and hydrogen peroxide (30%) (J. T. Baker) at 200 ^oC for 15 min. Immediately after cleaning, a thin layer of release coating was applied on the surface of the master. This

release coating reduces the surface energy of the master and hence promotes peel-off of mold from master during the preparation of the mold. To apply a release coating, the master was immersed in a solution containing 1H,1H,2H,2H-perfluorodecyltrichlorosilane (FDTS) (96%) and n-heptane (99%) (Alfa Aesar) in the ratio 1:1000 (by volume) followed by immediate transfer of the master to acetone (99.5%) for another 5 min then baked for 5 min at 110 ^{o}C on a hot plate. The thickness of the thin film of FDTS was measured using ellipsometry (J.A. Woollam VASE). The measured value the thickness of the coating, 1.76 nm ± 0.12 nm is comparable to the previously-reported value for a single layer of FDTS 1.6 nm [17].

2.2.2 Preparation of Mold

To make an elastomeric mold a commercial PDMS product, Sylgard 184 from Dow Corning, was used. The mixture of Sylgard 184 base and a curing agent in the ratio 10:1 (by weight) was mixed thoroughly. The mixed PDMS was then degassed using a bell–jar desiccator connected to a vacuum pump for 30 min, which removes air bubbles generated during the mixing process. About 5 g of degassed PDMS was then poured onto the Si master placed at the center of a petri dish (48 mm internal diameter and 7 mm height, BD Flacon 50 x 9 mm style) as shown in Figure 2.2.2 (a). Air bubbles generated due to the pouring of PDMS on the master were removed by degassing of PDMS for another 10 min. Then this PDMS prepolymer was cured at room temperature for 12 hours followed by a 1 hour bake on a hot plate at 90 ^{o}C. The PDMS mold was then peeled-off from its master and extra PDMS outside the boundary of the master was removed. The mold was then treated with release coating using the same processes as was used for the master and for imprinting in subsequent steps. Typical thickness of the PDMS mold was ~2 mm.

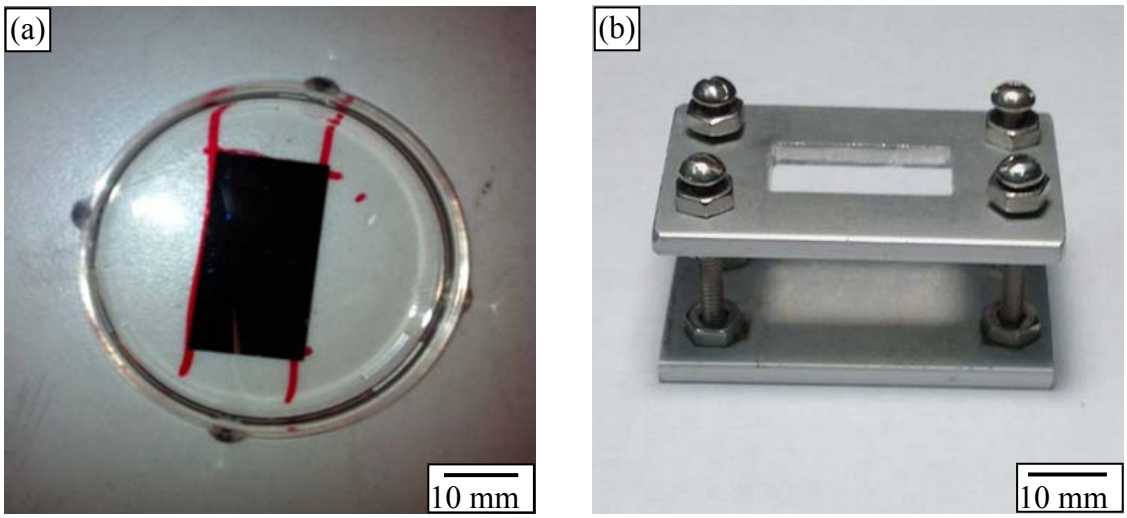

Figure 2.2.2 (a) SiNP arrays mounted on petri dish and embedded into PDMS. Red color marks are the reference lines used to align the master close to the center of the dish. (b) Home made clamp device with window on the upper plate to pass UV-light and used in the SL process.

2.2.3 Imprint of Polymer

SU-8 2002 (MicroChem Corp.) was used as an imprinting polymer because of its relatively low glass transition temperature (55 ^{o}C) in an uncured state [18], low volume shrinkage coefficient, and wide range of operating temperatures (up to 230 ^{o}C for fully cured SU-8) [19].A thin film of SU-8 was spin-coated onto a piranha-cleaned Si wafer or glass substrate with 10 x 20 mm^2 area, at 500 rpm with acceleration of 110 rpm/s for 6 s, then at 3000 rpm at 550 rpm/s for 36 s using a Laurell Spin Processor (Model WS-400A-6NPP-LITE). The polymer film was soft baked at 65 ^{o}C for 1 min and then at 95 ^{o}C for at least 2 min to remove any residual solvent. The film was cooled to room temperature and then a PDSM mold was placed on top of it. To ensure conformal contact between the mold and the film, an overpressure of ~1 bar was applied between them using a home-made device, as shown in Figure1.2.1 (b).

The mold and SU-8 were then held at 95 ^{o}C on a hot plate for 5 min and exposed to UV light (λ = 365 nm) in a mask aligner (MA6, Karl Suss) at 12 mW/cm^2 for 90 s. A post-expose bake was then done for 300 s and the sample was allowed to cool to room temperature. The PDMS mold was slowly and carefully peeled off the substrate without any dragging such that the SU-8 structures should remain on the supporting substrate. This SL process is very efficient as a single Si master can be used to make many molds (>100), while a single mold can be used to make many replicas (>50) without any cleaning requirement. Figure 2.2.3 shows scanning electron microscope (SEM) images of a representative Si-NP master / PDMS stamp / SU-8 replica set. In the next section, we will introduce several different nanostructures fabricated via SL process.

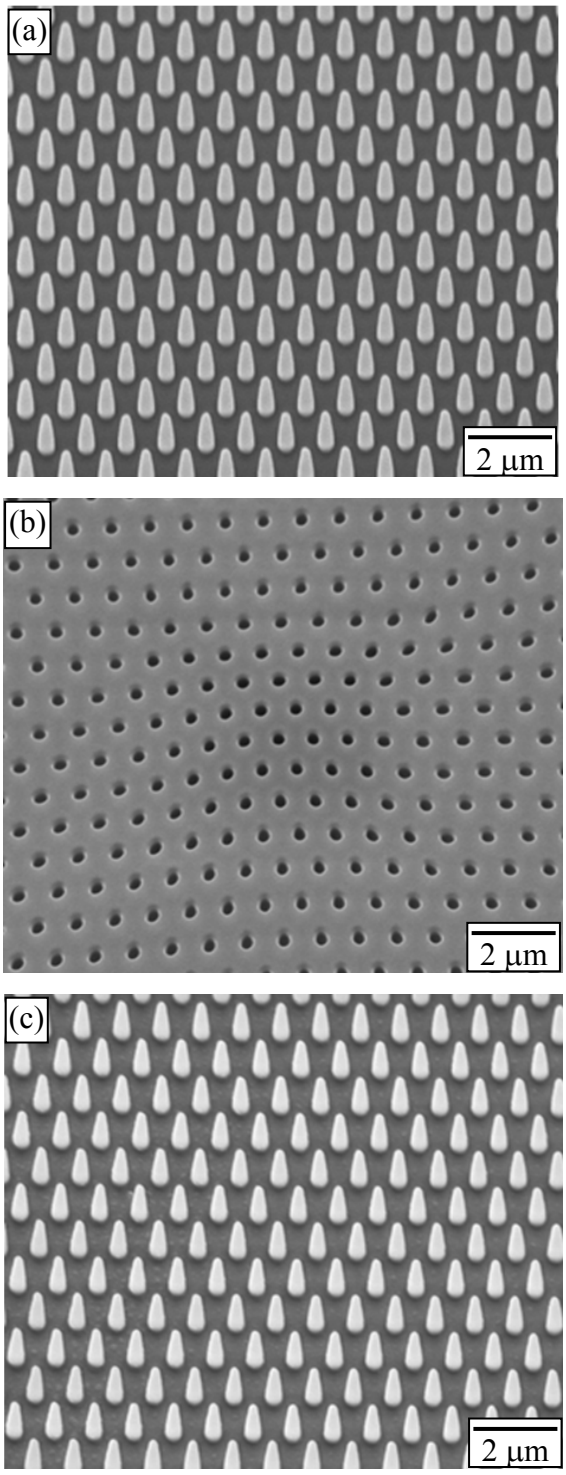

Figure 2.2.3 SEM images of the SL process. (a) Arrays of 2 μm-tall conical shaped Si nanopillars of period 900 nm used as a master. (b) PDMS mold of the master. (c) SU-8 replica of the master.

2.3 Fabrication of Soft Lithography-Based Nanostructures

2.3.1 Hollow Metallic Nanocylinders

The simplest nanopillar array-based structure to fabricate, aside from nanopillars themselves, is a cylinder. SL has been used to fabricate arrays of nanocylinders of different metals of various radii and pitches [15,20,21]. To make structures as those shown in Figure 2.3.1, we metalized SU-8 nanopillar arrays using a PVD system (usually sputter deposition, although thermal and electron beam evaporation can be employed, albeit with reduced conformality) followed by mechanical polishing to remove metal only from the tops of the nanopillars, and reactive ion etching (RIE) to remove the polymer from the core of the pillar. A detailed description of the fabrication process of such structures and their optical properties will be provided in Appendix I.

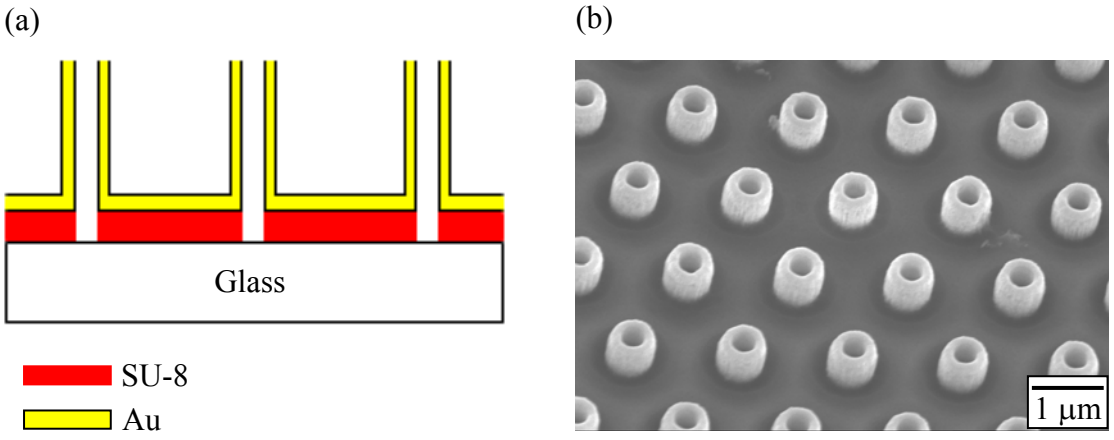

Figure 2.3.1 (a) Schematic and (b) SEM image of a hollow Au cylinder array of pitch 1.3 μm, with 300 nm inner radius and 1.8 μm height.

2.3.2 Nanocoax Arrays

Fabrication processes for nanocoaxial structures start from the metallization of arrays of polymer nanopillars imprinted on a substrate using the SL processes. Figure 3.3.2 represents the steps involved to fabricate a nanocoax array from an array of metalized nanopillars. A thin film (~150 nm) of Cr or Au was deposited on the SU-8 pillar array (to later serve as the coax inner conductor) using sputter deposition (AJA International) with 200 W dc power. The thickness of the sputtered metal coating on vertical nanostructure is not uniform. We found more conformal coating of metal occurred on a conical than on straight vertical structure. Typically, the thickness of the metal on the wall of the conical pillar was one third of the thickness of the metal on the floor. After the initial metallization, we deposit a dielectric layer. We deposited two kinds of dielectrics, porous and nonporous, using different methods. At the initial stages in the development of the nanocoax we attempted to make nanocoax arrays with porous dielectric annuli. However, we never succeeded to make a working device as we always ended up with electrical shorts between the coax electrodes. This could be due to conductive paths formed by coating of the outer electrode's metal through the pores of the porous dielectric during its deposition process. To overcome this issue, we deposited a thin layer of a nonporous dielectric on the metallized nanopillar prior to the deposition of the porous dielectric. An initial coating onto the metallized nanopillars of 10 nm thick nonporous Al_2O_3 was deposited by atomic layer deposition (ALD) (Savannah S100, Cambridge Nanotech) to prevent potential shortages between the inner and outer coax electrodes. For ALD of Al_2O_3, we used trimethylaluminum as a precursor and a deposition temperature of 200 ^{0}C. Following ALD, reactive sputtering was employed to deposit 100 nm thick (radial direction) of porous Al_2O_3. Reactively sputtered deposition of Al_2O_3 was done by

introducing O_2 gas in ratio 1:6 to Ar during deposition of Al at room temperature. Of the two deposition methods, ALD gave more conformal coatings of dielectric on vertical structures. In some cases, we used plasma enhanced chemical vapor deposition (PECVD) to deposit 100-200 nm thick films of porous SiO_2. The PECVD of SiO_2 was performed in a Plasma-Therm Versaline chemical vapor deposition system using a gas mixture with ratio SiH_4/N_2O: 2/9 at 200^oC. We found that this produces a deposition rate of SiO_2 of ~42 nm/min. Finally, we deposited an outer metal film of Cr of thickness 100-200 nm to make a complete nanocoax structure. For chemical sensing, an open ended coax array was made. Figures 2.3.2 and 2.3.3 show the steps involved and corresponding SEM images for this fabrication process for open ended nanocoax, respectively. Open ended nanocoaxes are obtained by removing the top part of the outer metal of the coax by mechanical polishing. Before polishing, support for each nanocoax was provided by a second SU-8 layer. The second layer of SU-8 of a thickness comparable to or greater than the height of the nanocoaxes was spin-coated onto this newly- formed coax array, at 500 rpm with acceleration of 110 rpm/s for 6 s, then at 3000 rpm at 550 rpm/s for 36 s using a Laurell Spin Processor followed by UV exposure at 12 mW/cm^2 for 90 s and a hard bake at 200 ^oC for 1 h.

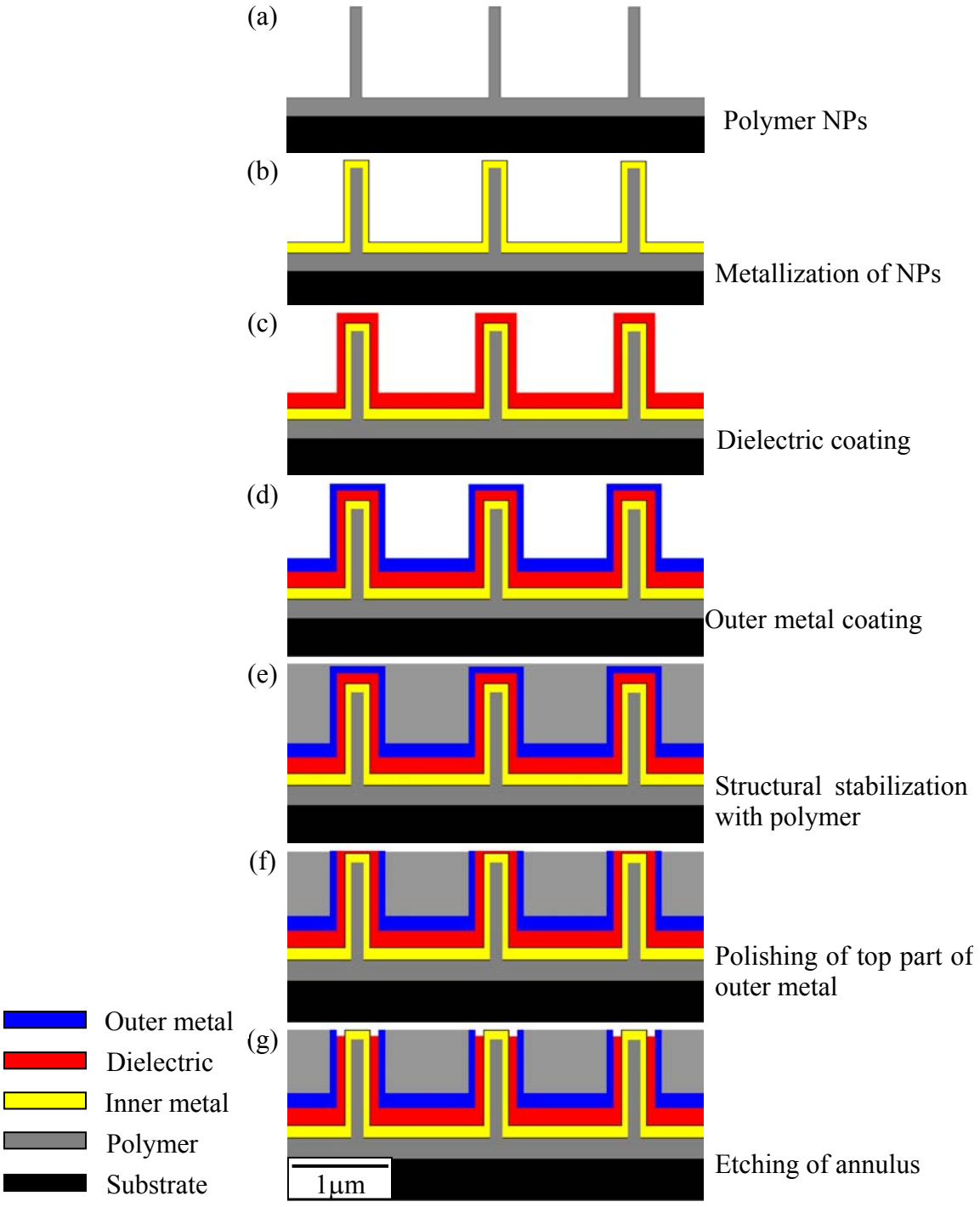

Figure 2.3.2 Schematic representations of fabrication process for nanocoax arrays. (a) Polymer nanopillar arrays, (b) Inner metal coating, (b) dielectric coating, (c) outer metal coating, (d) polymer coating, (e) mechanical polishing and (f) dielectric etching.

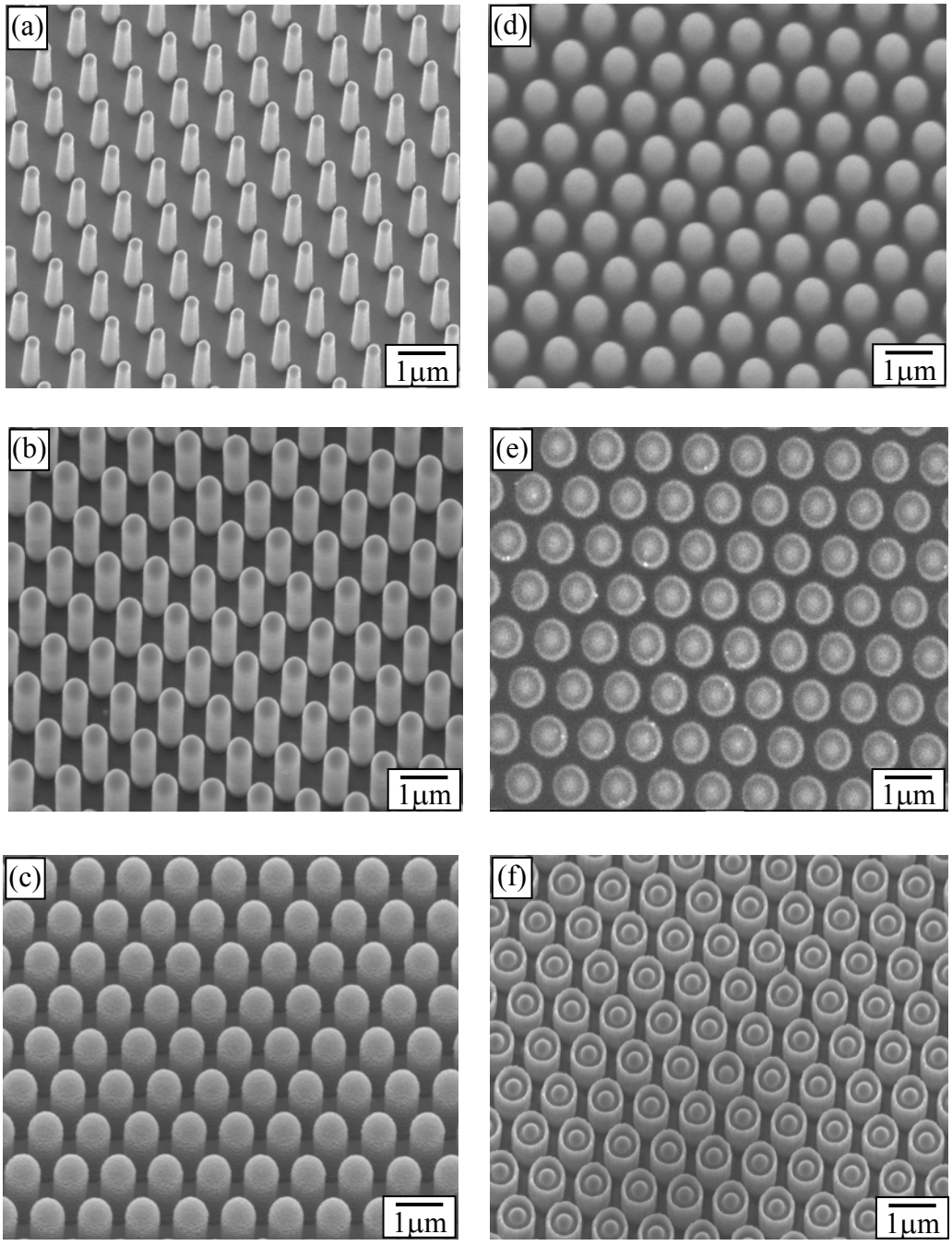

Figure 2.3.3 SEM images of the fabrication process for open ended nanocoax structure of 1.3 μm pitch and 2 μm height. (a) Inner metal Cr or Au coating, (b) dielectric Al_2O_3 coating,(c) outer metal Cr coating, (d) SU-8 coating, (e) mechanical polishing and (f) dielectric etching.

A mechanical polisher (Vibromet 2, Buehler) with a suspension of 50 nm diameter alumina nanoparticles was used for 2.5 h to remove the top part of the outer metal of the coax. This results in arrays of open-ended nanocoaxes, consisting of 0.685 x 10^6 coaxial capacitor units/mm^2. We then removed the uppermost part of the dielectric from the annuli of coaxes using dry etching methods. For dry etching, we used reactive ion etching (RIE). The RIE was performed in a Plasma-Therm Versaline inductively-coupled reactive ion etch (ICP-RIE) system for 2 min with flow 20 SCCM of CF_4 at 0.5 Pa pressure, 200 W power and 355 V self-bias conditions. We found that this produces an etch rate of ~200 nm/min for the SiO_2 and ~20 nm/min for the Al_2O_3. This RIE process also removed the supporting polymer. This etching process also helps us to clean the sample by removing the alumina nanoparticles which were attached on coaxes during the mechanical polish.

We sought to increase the porosity, and thereby molecules access into porous dielectric annulus of nanocoax arrays. To do so we attempted to make the arrays with alternating thin layers of two different porous dielectrics in the annulus followed by the selective etching of one of the two dielectrics. For this we sputter deposited alternative layers of porous Al_2O_3 and SiO_2 for the annulus and then we removed the SiO_2 using RIE. Figure 2.3.4 shows SEM images of the arrays of the nanocoax with alternative layers of two different dielectrics in the annulus.

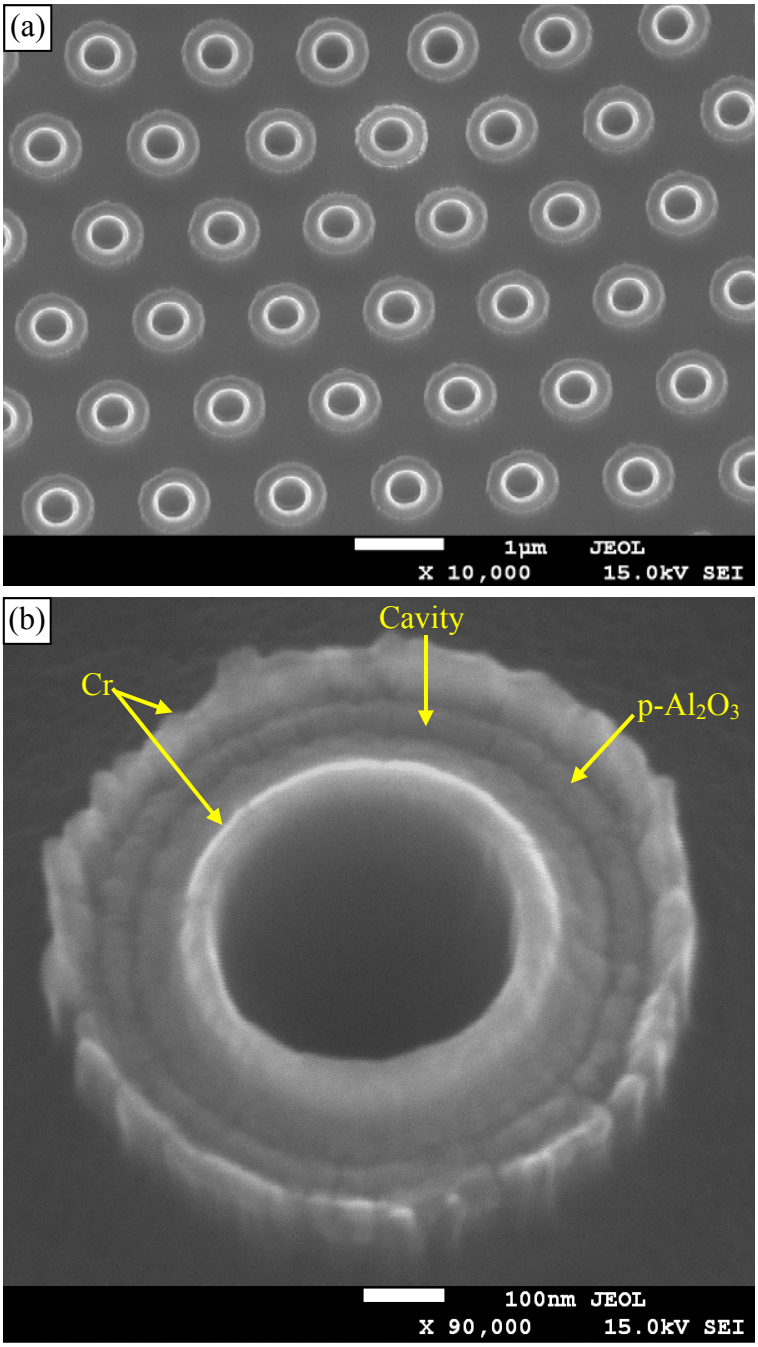

Figure 2.3.4 (a) SEM image of arrays of nanocoax with alternative layers porous (p-Al_2O_3) alumina and cavities made by etching SiO_2 from the annulus. (b) SEM image of top view of a nanocoax seen in (a) with ~40 nm and ~20 nm thick alternative layers of p-Al_2O_3 and cavities, respectively, in the annulus. The hole at the core of the coax is due to etching of the supporting SU-8 NP.

We also fabricated arrays of hollow cavity annulus nanocoax arrays by etching the dielectric of open-ended nanocoax arrays with nonporous dielectric annulus as shown in Figure 2.3.5(a).This etching process opens a cavity between the coax inner and outer electrodes. A nonporous dielectric Al_2O_3 at the annuli of the nanocoaxes with Au and Cr inner and outer electrodes, respectively, was etched to a time-controlled depth at room temperature at a rate of ~20 nm/h by immersion in Transetch-N solution. Figure 2.3.5 (b) shows SEM image of an arrays nanocoax of 1.3 μm pitch, 200 nm annulus thickness, and 500 nm annulus depth. We have fabricated similar arrays with annulus thickness ranging from 50 to 400 nm by etching the dielectric of the nanocoaxes with corresponding annuli width. Figure 2.3.6 shows SEM images of the arrays of nanocoax of annuli width between 100 and 400 nm.

Arrays of nanocoax with porous dielectric and hollow annulus were fabricated to be used as capacitive and electrochemical sensors, respectively. Details about measurement techniques and performance of nanocoax-based capacitive sensors will be discussed in Chapter 3. The performance of nanocoax-based electrochemical sensors will be discussed in Chapters 4 and 5.

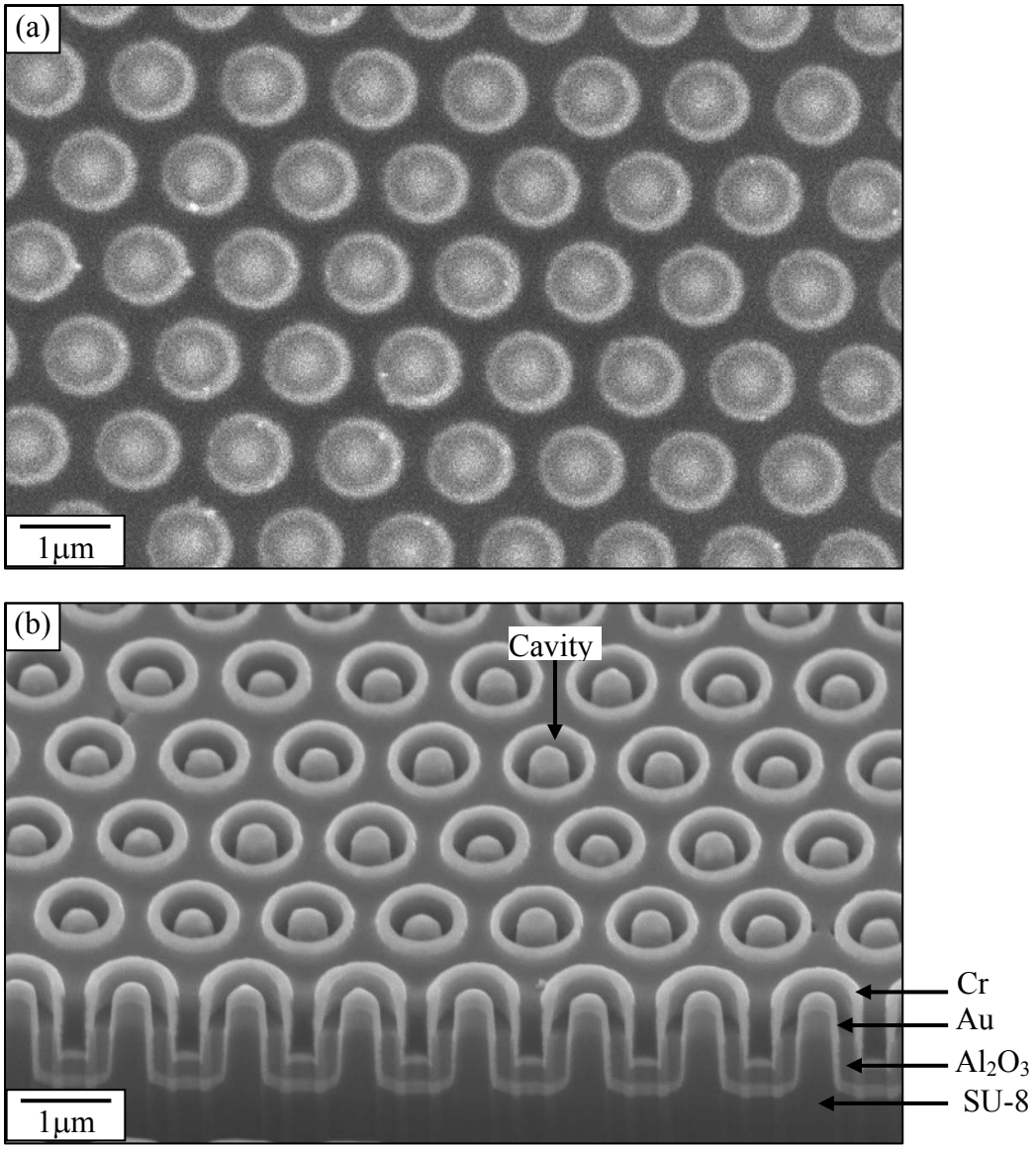

Figure 2.3.5 SEM image of arrays of (a) open-ended nanocoax with nonporous dielectric annulus, (b) partially hollow nanocoax of 1.3 μm pitch, 200 nm annulus thickness, and 500 nm annulus depth with Au inner and Cr outer electrodes. Bottom portion in (b) shows a cross-section of one row of the arrays, prepared by FIB milling.

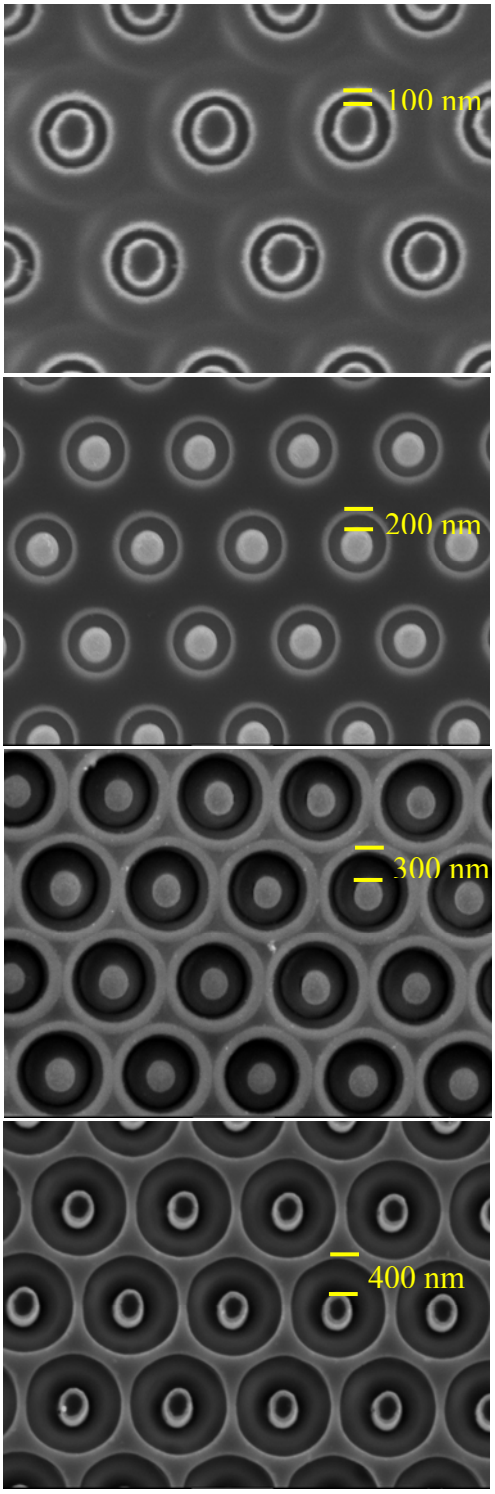

Figure 2.3.6 SEM images of nanocoax structures of 1.3 μm pitch and 500 nm annulus depth with different annulus thickness, from top to bottom: 100 nm, 200 nm, 300 nm and 400 nm.

2.3.3 Nanotriax Arrays

Nanotriax structure is similar to nanocoax structure where the central metallic core is surrounded by two metallic sheath layers insulated from each other as shown in Figure 2.3.7 (a). In the nanotriax the outermost metallic sheath circumferentially surrounds the "nanocoax" thus providing a local shield or allowing the middle metal layer to be used for active 'guarding' for each nanocoax [22]. Because of this guarding the nanotriax structure may help to minimize or eliminate noise associated with nanocoax-based devices, or in active guarding, eliminate the capacitance of the coax itself from the measurement. Besides, using the three electrodes of a nanotraix as working, counter and reference electrodes it can be developed to make an electrochemical cell.

To fabricate the nanotriax, a thin film (~50 nm) of nonporous Al_2O_3 was deposited on arrays of Cr-Al_2O_3-Cr and Au-SiO_2-Cr coaxial structures of diameter ~650 nm. Finally, we deposited an outer metal film of Cr of thickness ~150 nm to make a complete nanotriax structure. Open-ended nanotriaxes were obtained by removing the top part of the outer metals and dielectrics by using the mechanical polisher for ~6 hrs. To make arrays of hollow cavity annulus nanotriax, SiO_2 dielectric was removed from open-ended Au-SiO_2-Cr-Al_2O_3-Cr nanotriax arrays. Figure 2.3.7 (b) and (c) show SEM images of arrays of nanotriax with porous dielectric and hollow cavity annulus, respectively. The effectiveness of the nanotriax structure on the performance of nanocoax based capacitive sensors will be mentioned in Chapter 3.

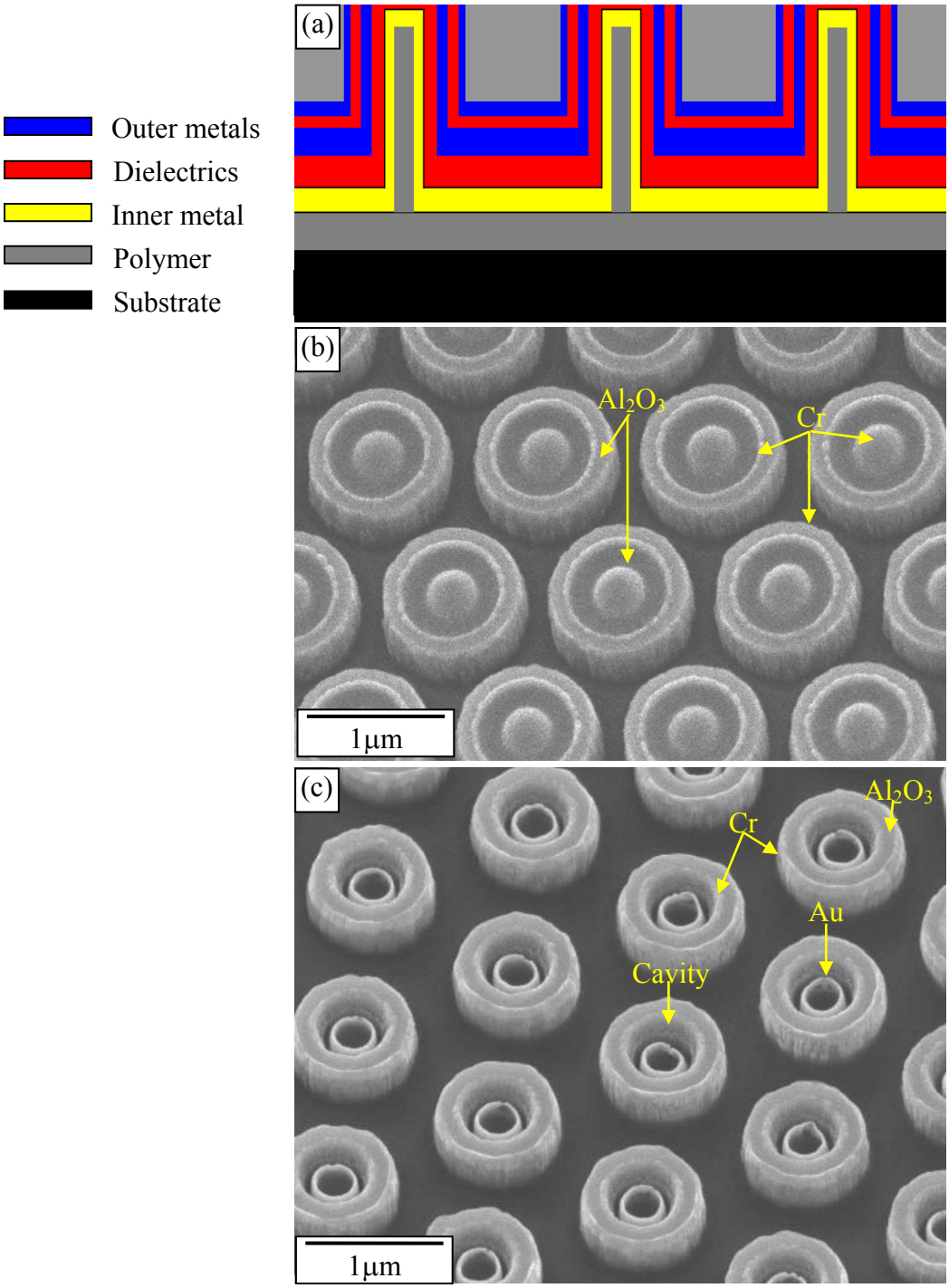

Figure 2.3.7 (a) Schematic of open-ended nanotriax array. SEM image of arrays of nanotriax with (b) Cr electrodes and Al_2O_3 annulus, and (c) with partially hollow cavity nanotriax of ~500 nm annulus depth with Au inner electrode and outer Cr electrodes are isolated by Al_2O_3. The hole at the core of the coax is due to etching of the supporting SU-8 NP.

Summary

Recent research has demonstrated the numerous advances in the development of reliable and economical methods for the preparation of nanostructures made from different materials. Although a different template-free method, such as the use of carbon nanotubes, is a direct route for the fabrication of the nanocoaxial structure, the use of a lithographically patterned structure provides a more economical and reproducible way to make nanodevices. In this chapter, we have introduced the fabrication processes for nanocoax and nanotriax structures using polymer replicas of Si nanopillar arrays made via soft lithography process. The polymer replicas were used as a starting point for the fabrication of the coax and triax arrays having porous, nonporous and cavity annulus.

References

[1] S. Barth, F. Hernandez-Ramirez, J. D. Holmes, and A. Romano-Rodriguez, Prog. Mater. Sci. **55**, 563 (2010).

[2] T. Mikolajick, A. Heinzig, J. Trommer, S. Pregl, M. Grube, G. Cuniberti, and W. M. Weber, Phys. Status Solidi RRL – Rapid Res. Lett. **7**, 793 (2013).

[3] A. J. Mieszawska, R. Jalilian, G. U. Sumanasekera, and F. P. Zamborini, Small Weinh. Bergstr. Ger. **3**, 722 (2007).

[4] Y. Xia, P. Yang, Y. Sun, Y. Wu, B. Mayers, B. Gates, Y. Yin, F. Kim, and H. Yan, Adv. Mater. **15**, 353 (2003).

[5] Y. Xia and G. M. Whitesides, Annu. Rev. Mater. Sci. **28**, 153 (1998).

[6] Yan Chen, Z Hong Lin Wang, Jin Song Yin, David J.Johnson, and R.H. Prince, Chemical Physics Letters **272**, 178 (1997)

[7] K. Suenaga, Y. Zhang, and S. Iijima, Appl. Phys. Lett. **76**, 1564 (2000).

[8] R. E. Camacho, A. R. Morgan, M. C. Flores, T. A. McLeod, V. S. Kumsomboone, B. J. Mordecai, R. Bhattacharjea, W. Tong, B. K. Wagner, J. D. Flicker, S. P. Turano, and W. J. Ready, JOM **59**, 39 (2007).

[9] H. Zhou, A. Colli, A. Ahnood, Y. Yang, N. Rupesinghe, T. Butler, I. Haneef, P. Hiralal, A. Nathan, and G. A. J. Amaratunga, Adv. Mater. **21**, 3919 (2009).

[10] H. Zhao, B. Rizal, G. McMahon, H. Wang, P. Dhakal, T. Kirkpatrick, Z. Ren, T. C. Chiles, M. J. Naughton, and D. Cai, ACS Nano **6**, 3171 (2012).

[11] J. E. Jang, S. N. Cha, Y. J. Choi, D. J. Kang, T. P. Butler, D. G. Hasko, J. E. Jung, J. M. Kim, and G. A. J. Amaratunga, Nat. Nanotechnol. **3**, 26 (2008).

[12] T. Paudel, J. Rybczynski, Y. T. Gao, Y. C. Lan, Y. Peng, K. Kempa, M. J. Naughton, and Z. F. Ren, Phys. Status Solidi A **208**, 924 (2011).

[13] D. Cai, L. Ren, H. Zhao, C. Xu, L. Zhang, Y. Yu, H. Wang, Y. Lan, M. F. Roberts, J. Chuang, M. J. Naughton, Z. Ren, and T. C. Chiles, Nat. Nanotechnol. **5**, 597 (2010).

[14] J. Rybczynski, K. Kempa, A. Herczynski, Y. Wang, M. J. Naughton, Z. F. Ren, Z. P. Huang, D. Cai, and M. Giersig, Appl. Phys. Lett. **90**, 021104 (2007).

[15] B. Rizal, F. Ye, P. Dhakal, T. C. Chiles, S. Shepard, G. McMahon, M. J. Burns, and M. J. Naughton, in *Nano-Opt. Enhancing Light-Matter Interact. Mol. Scale*, edited by B. D. Bartolo and J. Collins (Springer Netherlands, 2013), pp. 359–370.

[16] Y. Xia and G. M. Whitesides, Angew. Chem. Int. Ed. **37**, 550 (1998).

[17] J. Choi, K. Sakurai, and T. Kato, Surf. Interface Anal. **42**, 1373 (2010).

[18] T. Choi, J.-H. Jang, C. K. Ullal, M. C. LeMieux, V. V. Tsukruk, and E. L. Thomas, Adv. Funct. Mater. **16**, 1324 (2006).

[19] R. Feng and R. J. Farris, J. Micromechanics Microengineering **13**, 80 (2003).

[20] D. J. Lipomi, M. A. Kats, P. Kim, S. H. Kang, J. Aizenberg, F. Capasso, and G. M. Whitesides, ACS Nano **4**, 4017 (2010).

[21] Q. Xu, R. Perez-Castillejos, Z. Li, and G. M. Whitesides, Nano Lett. **6**, 2163 (2006).

[22] Paul Horowitz and Winfield Hill, *The Art of Electronics 2nd Ed*, (Cambridge University Press, Cambridge UK, 1989) pages 1013-1015

Chapter 3

Nanocoax for Chemical Sensing

3.1 Introduction

Chemical sensors have attracted extensive research interest due to the perceived virtues of sensitive, rapid response, and stable sensors for the detection and identification of target chemicals and biological agents. The perceived value of such sensors is for use in environmental monitoring, threat detection, and clinical diagnostics. Generally speaking, there are several basic criteria for an efficient sensing system: (i) high sensitivity and selectivity, (ii) fast response and recovery times, (iii) low analyte consumption, (iv) low operating temperature, (v) temperature independence and (vi) performance stability [1]. Advances in micro/nanotechnologies have created huge potential to build highly sensitive, low cost, and portable chemical sensors with low power consumption. Schemes involving nanopores, nanowires, microcantilevers, and microcavities have reportedly achieved highly sensitive molecular detection [2–6]. Regardless of the sensing principle, most of the sensors are based on adsorption and desorption of molecules on the surface of a sensing material. By increasing the contact area of the interface between the analyte and sensing material, the sensitivity can be significantly enhanced [1] although it must be noted that sensitivity without a way to provide selectivity is of limited value. Commonly used materials for the detection of molecules include vapor-sensitive polymers, semiconducting metal oxides, and other mesoporous materials such as alumina, silica and titania [7–10].

The extremely high surface to volume ratio and porous structure of some nanomaterials is ideal for the adsorption and storage of gaseous molecules [1]. Therefore, gas sensors based on nanomaterials, such as carbon nanotubes (CNTs), nanowires, nanofibers, and nanoparticles, have been investigated widely [1,11–15]. For example, gated single-walled carbon nanotubes (CNT) have been used to detect NO_2 and NH_3 gases to parts-per-million (ppm) levels in Ar [16], while resistivity changes have been observed in graphene microcrystals [17] upon exposure to those same gases, with a projected limit of detection (LOD) of ~1 part-per-billion (ppb). Nanostructured metal oxide films [10,18] have been used in a large category of sensors that have shown high sensitivity to chemicals. For example, SnO_2 semiconductor metal-oxide sensors have a reported capability of ethanol detection down to ppb levels [19]. Another structure, such as an array of nanomechanical resonators, demonstrated ppb level sensitivity for the detection of the chemical warfare agent stimulant diisoproply methylphosphonate [20]. Generally, the types of sensors mentioned so far are 2D structures with individual sensing units lying on a planar substrate; this can severely limit access of target molecules to the sensing element. Moreover, fabricating a large number of such individual sensors is a serial process which requires sophisticated lithographic techniques and can therefore be very time-consuming. Usually, temperatures of several hundred of degrees centigrade and detection times of minutes are required to achieve the reported sensitivities, and the selectivity is poor. Here, we demonstrate the use of a nanocoaxial 3D architecture for sensitive, room temperature, rapid response, and all electronic bio/chemical capacitive detection.

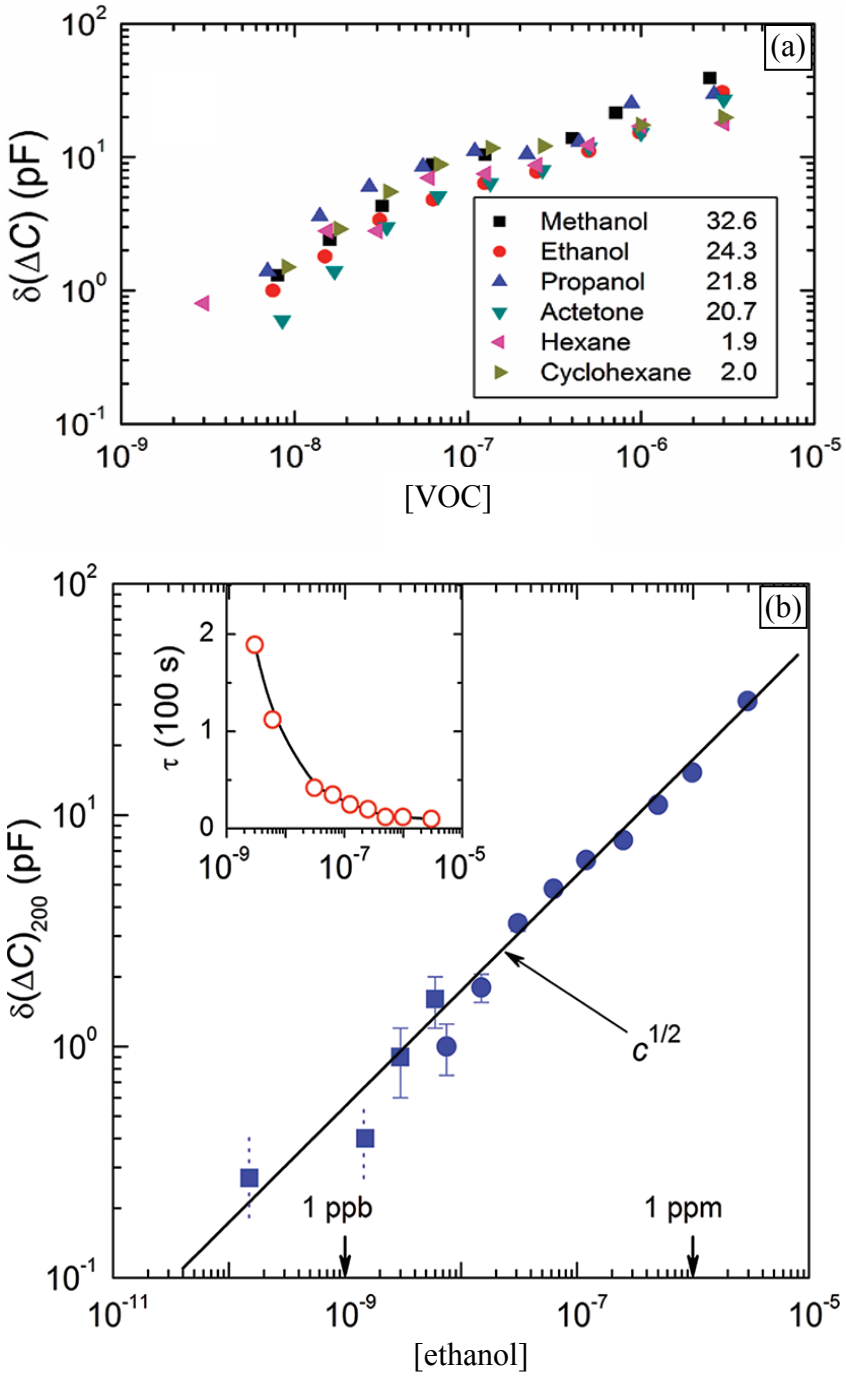

Figure 3.1.1 (a) Concentration-dependent response of nanocoax-based capacitive gas sensor for various volatile organic compounds. Numbers in the figure legends are the values of relative permittivity ε_r of the chemicals. (b) Performance of the nanocoaxial sensors for the detection of ethanol molecules diluted with N_2 gas. The average response of coax after subtraction of N_2 background and recorded 200 s after ethanol application $\delta(\Delta C)_{200}$, versus the concentrations of ethanol. Inset: derived time constant for the different concentrations of ethanol. From [21].

The high surface area per unit volume of the nanocoaxial structure makes it a natural candidate for chemical and biological sensing and provides a way to scale the sensing volume. These features of the nanocoax have been successfully applied in a gas sensor. We have used an array of vertically aligned nanoscale coaxial electrodes constructed with porous dielectric coax annuli around CNT cores to make a highly sensitive capacitive detector for non-specific detection of chemicals [21]. The performance of the device was investigated for the detection of different concentrations of volatile organic compounds diluted in N_2 gas, as can be seen in Figure 3.1.1 (a). While the sensitivity of CNT-based nanocoaxial gas sensors is impressive, the starting CNT structure has some issues which were already mentioned in Chapter 2. In order to improve the issues associated CNT-based fabrication process, we have used soft lithography to prepare polymer nanopillar arrays as a scaffold to make arrays of nanocoaxes. Arrays of nanocoaxes with various dielectric annuli were employed to understand the role of the porosity of the dielectric annulus in these nanocoax-based capacitive gas sensors. The capacitive sensing performance of a partially hollowed annulus nanocoax array for the detection of biomolecules in aqueous media was also investigated. In this Chapter, we describe the working principle, and the experimental set up for open-ended nanocoax arrays as a capacitive gas sensor. Furthermore, we show why the 3D nanocoax configuration with various dielectrics is beneficial for gas sensing applications versus the various 2D/planar architectures.

3. 2 Working Principle of Capacitive Gas Sensor

The capacitance of each nanocoax can be calculated according to the equation:

$$C_{coax} = \frac{2\pi l \varepsilon_0 \varepsilon_r}{ln(\frac{r_2}{r_1})}$$

where r_1 and r_2 are the outer and inner radii of the inner and outer electrodes, respectively l is the length or height of the nanocoax, ε_0 is the free space permittivity which equals 8.85 pF/m, ε_r is the dielectric constant of the dielectric in between the electrodes. The capacitance of the nanocoax arrays also includes a contribution from the planar areas between coaxes and which can be expressed as:

$$C_{planar} = \frac{S \varepsilon_0 \varepsilon_r}{d}$$

where S is the area overlapped by the two electrodes, and d is the thickness of the dielectric (which is not necessarily the same value as r_2-r_1).

The total capacitance of the array of coaxes is thus that of a parallel combination:

$$C = C_{coax} + C_{planar}$$

$$C = C_0 \varepsilon_r$$

where $C_0 = \frac{2\pi l \varepsilon_0}{ln(\frac{r_2}{r_1})} + \frac{S \varepsilon_0}{d}$ is the capacitance for such an array of nanocoax with vacuum dielectric.

When we exposed an array of nanocoaxes to a target molecule, those molecules enter into the annuli of the array (e.g., via diffusion and chemical and/or physical adsorption) and cause changes in the effective dielectric constant ($\Delta\varepsilon_r$) of the circuit and hence the capacitance (ΔC) of the array i.e.,

$$\Delta C = C_0 \Delta\varepsilon_r$$

A change in the capacitance indicates the presence of the target molecules and the magnitude of the change should be proportional to the number and dielectric properties of the target molecules. Furthermore, an oscillatory field excites molecules within the annulus of the coaxes and they respond differently at their own characteristic frequencies. Thus a capacitance measurement across a range of frequencies, i.e. dielectric spectrum, can potentially provide information about the species in the annuli of the device which can potentially be used to identify which bio/chemical molecules infiltrated the dielectric.

3.3 Experimental Setup

Measurements to test the performance of these capacitive gas sensors were carried out using two homemade chambers connected with a gas dilution system and a capacitance bridge. In the early stages of the experiment, we used a so-called first generation (1G) chamber as shown in Figure 3.3.1. Later, we tried to improve the quality of the chamber by decreasing its volume, integrating a heater and temperature sensor and using less outgassing materials and named this a second generation (2G) chamber. In addition to minimizing the required volume of the analyte, decreasing the volume of the chamber can facilitate more rapid purging and pumping.

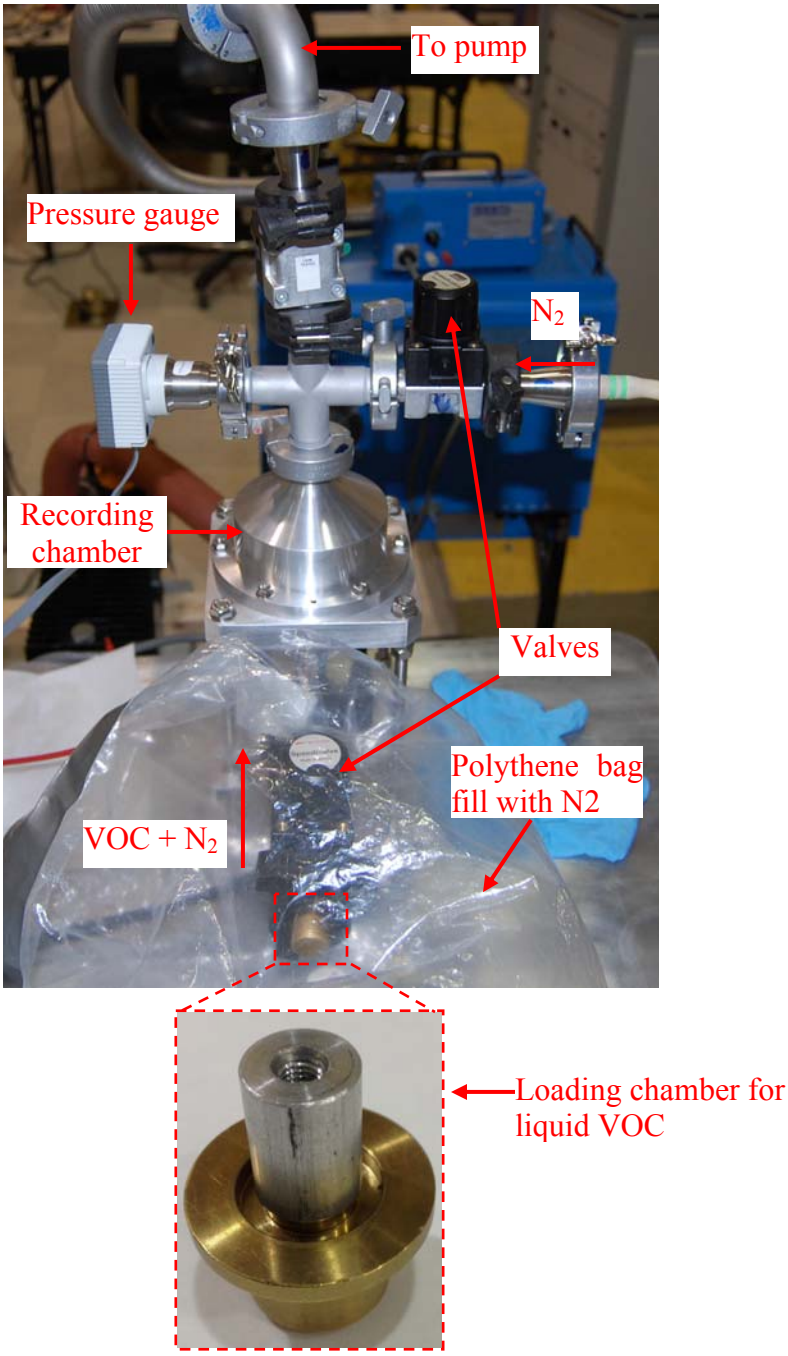

Figure 3.3.1 Gas dilution system and Al chamber used in 1G chamber. Liquid VOC was loaded on the loading chamber in N_2 environment created inside the polythene bag and then vaporized inside the chamber.

Integration of the chamber and heater made the 2G chamber capable of studying the temperature dependence on the performance of the sensing devices. Both chambers are air-tight with valves for a gas inlet, pumping port, and exhaust inlet. For the dilution of chemicals, in the 1G chamber we directly vaporized a known volume of liquid VOC and N_2 gas into the evacuated chamber. In the 2G chamber, stock gases commercially prepared at ~3 parts per million (ppm) in N_2 were further diluted by ultra high purity N_2 from the same manufacturer. The concentration of VOC was determined in the 1G chamber by the amount of liquid VOC vaporized and in the 2G chamber by the flow rate ratio of the chemical gas and the dilutant N_2 gas controlled by MKS Instruments mass flow controllers (MFC) (MFC of range 10 or 500 standard cubic centimeters per minute) plumbed into a stainless steel manifold. The chambers were connected with exhaust valves and a pump. Figures 3.3.2 (a) and 3.3.3 show schematic diagrams and the experimental set up of the 2G chamber connected with the gas dilution system. A pin socket was used to make electrical connections between the electrodes of the sensor, heater and thermometer in the chamber to a capacitance bridge, power supply, and temperature controller located outside chamber, respectively. Figure 3.3.2 (b) shows a schematic diagram of a capacitance measuring bridge. The capacitance of the unknown, C_X, can be balanced by a calibrated variable standard capacitor C_S.

(a)

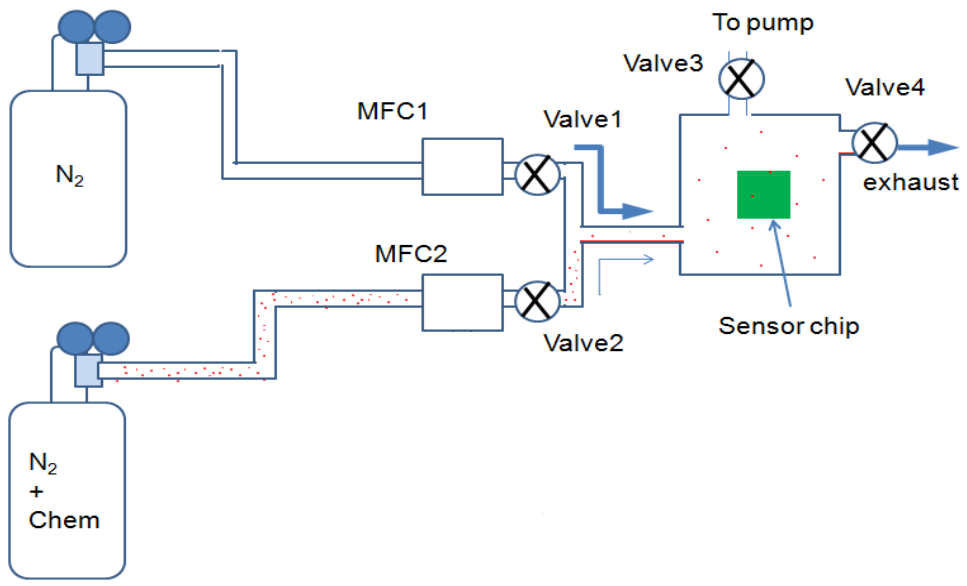

(b)

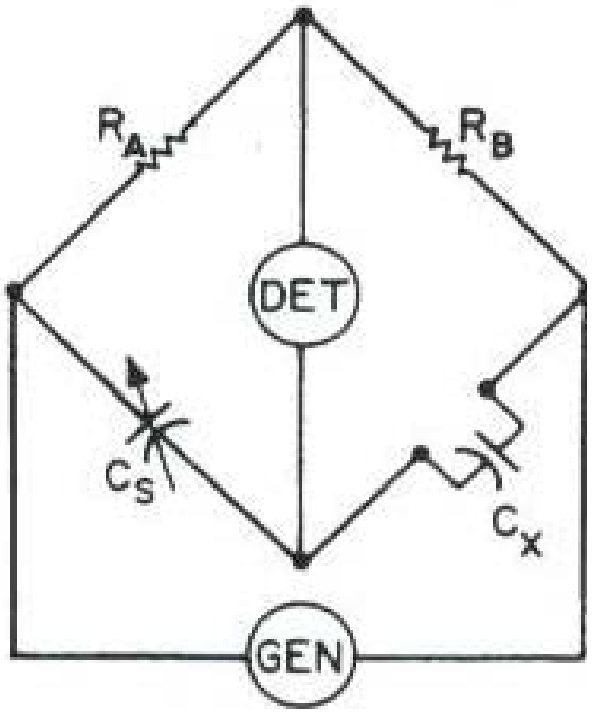

Figure 3.3.2 Schematic diagrams of (a) experimental setup showing integration of gas dilution system and the chamber and (b) an elementary capacitance measuring bridge. Here, "DET" and "GEN" stands for detector and generator connected to the bridge.

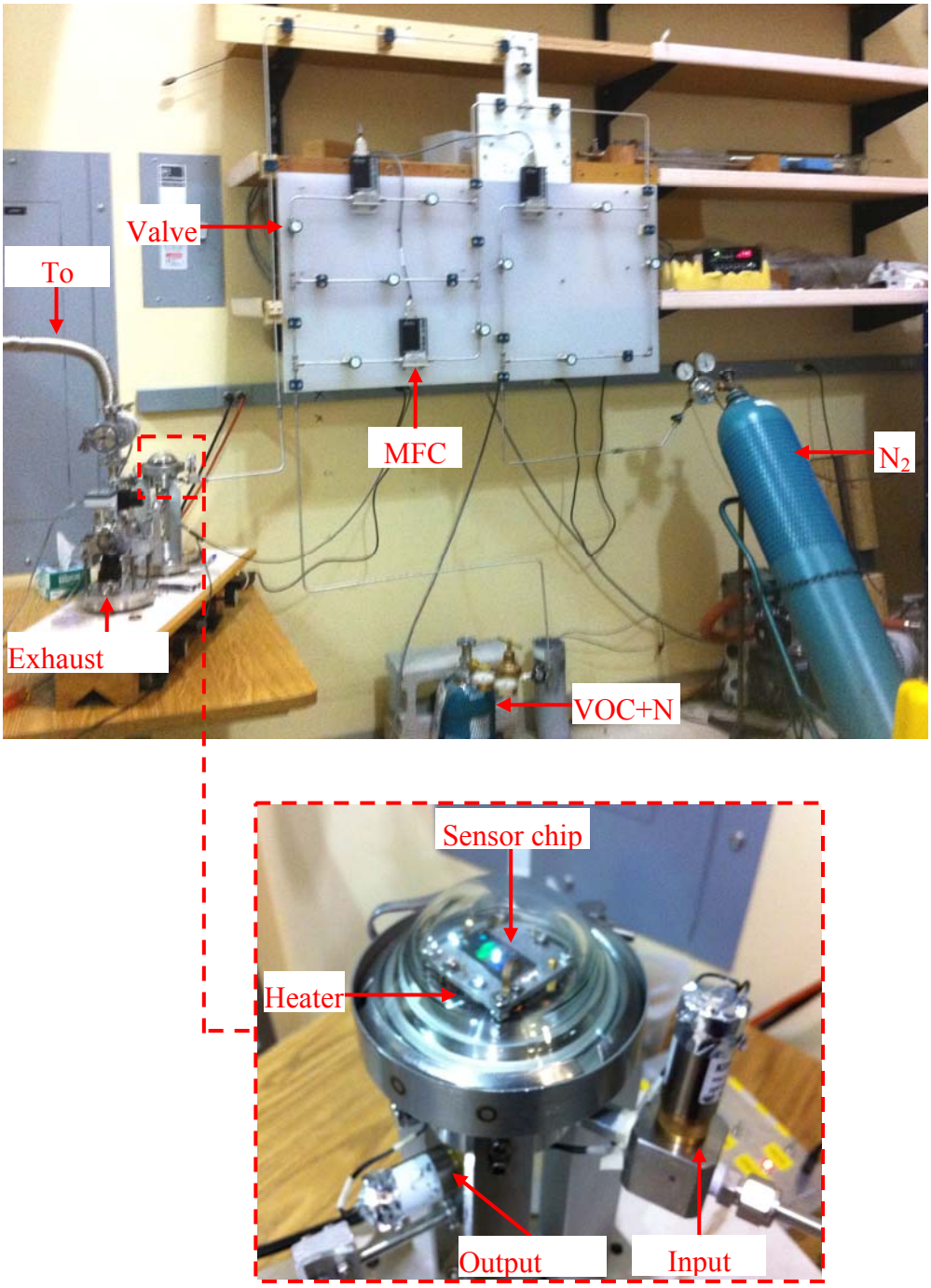

Figure 3.3.3 Stainless steel gas dilution system and glass chamber used for the present work. The cylinder containing commercially prepared VOC of concentration ~3 ppm in N_2 gas were connected with another cylinder containing ultra high purity N_2.

To measure the unknown capacitance of the nanocoax arrays, a General Radio Model 1616 (GR 1616) high precision capacitance bridge and a Stanford Research model 830 lock in amplifier (LIA) were used with the following settings: voltage 0.1 V, frequency 10 Hz, time constant 300 ms. Here we choose the lowest limit of working frequency (10 Hz) of the GR 1616 as capacitive contributions dominate over the resistive part at low frequency. The LIA, which contains an internal AC source, served as a signal generator and detector. The standard variable capacitor of the GR 1616 was used to find a value or a deviation, in the value of the capacitance of the unknown sensor capacitance. The temperature of the platform used to hold a sensor chip inside the chamber was recorded by using a Si diode (Lakeshore, DT-47-ET-13). A Lakeshore Model 331 temperature controller was used to supply power to the heater and to measure the temperature of the platform. The measurement procedures for both chamber systems were as follows: (1) Establish all electrical and pneumatic connections, close chamber, and evacuate system until the capacitance and pressure stabilize to a base value. Base value of the capacitance depends on the number of nanocoax and dielectric materials at the annulus of the coax. The typical base value of C was ~1 nF. The base value of the pressure was different for two different chambers and its typical values were ~1 mbar and ~10 μbar for 1G and 2G chambers, respectively. (2) Balance the capacitance bridge (capacitance and dissipation) using the standard method as mentioned in the GR 1616 operating manual. (3) Initially, to clean chamber or to remove residue of the analyte after exposure with single concentration of analyte, we purged and pumped the chamber three times with N_2. (4) Introduce the mixture of the chemical and N_2 at the different designated concentrations and (5) In the 1G chamber there was no flow of VOC+N_2, and pressure of the chamber

during the data recording was ~ 1 bar, whereas in the 2G chamber, we maintained ~1 bar with or without flow of (i.e. dynamic or static) of VOC+N_2 during data recording. Here we used the dynamic condition to predict the performance of the device in a real monitoring environment and static condition to know the LOD of the devices as the devices were found to be most sensitive in the static condition [21].

In the present work, we used the 1G chamber system to study the effect of porosity of the dielectric on the performance of the capacitive gas sensors and the 2G chamber system was used to determine the limit of detection of the sensor.

3.4 Sensor Performance

Porous materials such as Al_2O_3 and SiO_2 have been widely used in sensor applications [22, 23]. The porosity of the dielectrics in the annulus of the nanocoax is crucial to the sensor performance [21]. Physical or chemical adsorption/absorption of target molecules onto the surface of the porous medium is believed to be the basis of the molecular capture mechanism. The sorption behavior depends not only on the fluid-wall attraction but also on interactions between the fluid molecules. Additionally, the pore structure makes an interconnected network that facilitates the diffusion of molecules as well as decreases the sensor response time, as reported in our work with VOC detection [21]. We have also experimentally verified the key role of the porosity of the dielectric annulus in our sensor architecture by fabricating sets of coax structures having 1) porous dielectric, 2) porous dielectric and cavity and 3) nonporous dielectric and cavity annuli.

The measured capacitance of the arrays at 10 Hz is ~2.4 nF. This value is higher than the calculated value of ~1 nF determined using the effective dielectric constant 4.5 [24] of SiO_2 deposited in the spaces between adjacent conductors and the following relation

$$C_0 = N\left(\frac{2\pi l \varepsilon_0 \varepsilon_r}{ln(\frac{r_2}{r_1})}\right) + \frac{S \varepsilon_0 \varepsilon_r}{d}$$

Where N = 1.21 X 10^6 is the number of coaxes.

$$C_0 = 1.21 X 10^6\left(\frac{2\pi X 1.8 X 10^{-6} X 8.85 X 10^{-12} X 4.5}{ln(\frac{650}{250})}\right) + \frac{1.23 X 10^{-6} X 8.85 X 10^{-12} X 4.5}{2 X 10^{-7}}$$

$$C_0 = 940 \text{ pF} \sim 1 \text{ nF}$$

This difference could be accounted for by the differences in stoichiometry of the deposited oxide as well as adsorbed water on its surfaces. A porous dielectric and cavity coax annulus was formed by preferentially etching the SiO_2 in the coax annulus. Then the pores of a sample with porous dielectric were sealed to convert it into nonporous dielectric. This was done by depositing ~25 nm nonporous Al_2O_3 on the porous dielectric and cavity structure. It is important to note that, for arrays of coaxes with porous dielectric and both porous dielectric and cavity annuli, there was a significant drift (~10 fF/s for capacitors of capacitance ~1 nF) in capacitance with respect to time. However, this effect is negligible for the coax with nonporous dielectric and cavity annulus as shown in Figure 3.4.1.

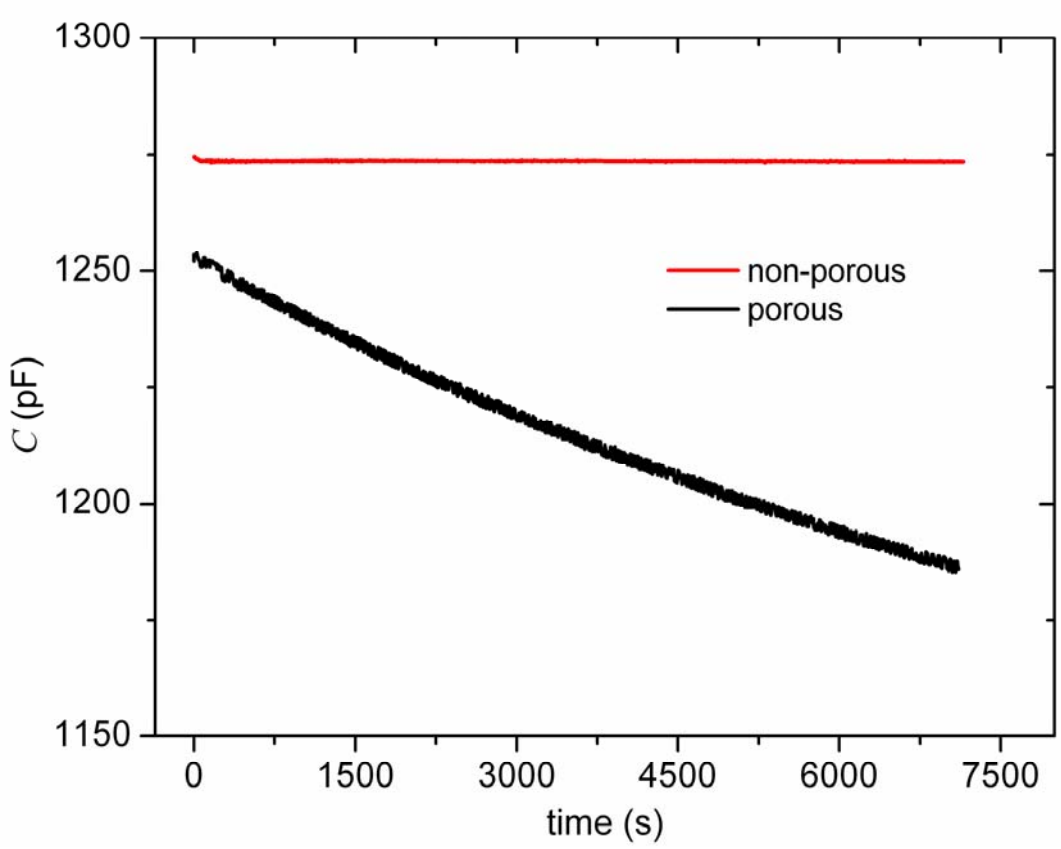

Figure 3.4.1 Drift of the capacitance of nanocoaxes arrays with porous and non-porous dielectrics annuli due to pumping of the 2G chamber containing them. Before pumping both types of coaxes were in N_2 environment.

In general, the slope of the drift is positive in the evacuated chamber and negative during the pumping of chamber or flow of N_2. Different attempts were performed to improve the stability of the coaxes such as using a chamber with less degassing materials, annealing of the dielectrics, applying high electric field on dielectric, electric guard of each nanocoax by employing nanotriax structure and pumping of the coax arrays for a long period of time. However, none of the above methods help to minimize the drift. The porosity of the dielectric may be the cause of the drift but the mechanism underlying the drift is yet to be clarified.

The performance of devices for the detection of volatile organic compounds (VOCs) diluted in N_2 gas was tested using the static measurement technique. Here high-purity nitrogen (with concentration of O_2, H_2O and VOC < 1 ppb) was used as a control. Figure 3.4.2 shows the response of all three devices detailed above at ~1 bar for N_2 and a mixture of N_2 and isopropyl alcohol (IPA) with molar fraction $N_{IPA}/(N_{IPA}+N_{N2}) = 0.43$ unit, where N_{IPA} and N_{N2} are the number of IPA and N_2 molecules in the chamber, respectively. The higher response of the coax array with porous and cavity annulus than with only porous medium annulus is probably due to the higher adsorption area for target molecules. Moreover, the porosity of the dielectric medium could be increased by etching of the dielectric. As mentioned above, some of the supporting SU-8 between the coaxes is removed during the etching of the dielectric. This facilitates diffusion of the gas molecules through the outer metallic wall (discussed in detail later in the Chapter) of the coaxes into the dielectric thereby enhancing the response. The response $\delta(\Delta C)$ only due to the chemical was obtained by subtracting the response of N_2 from the mixture.

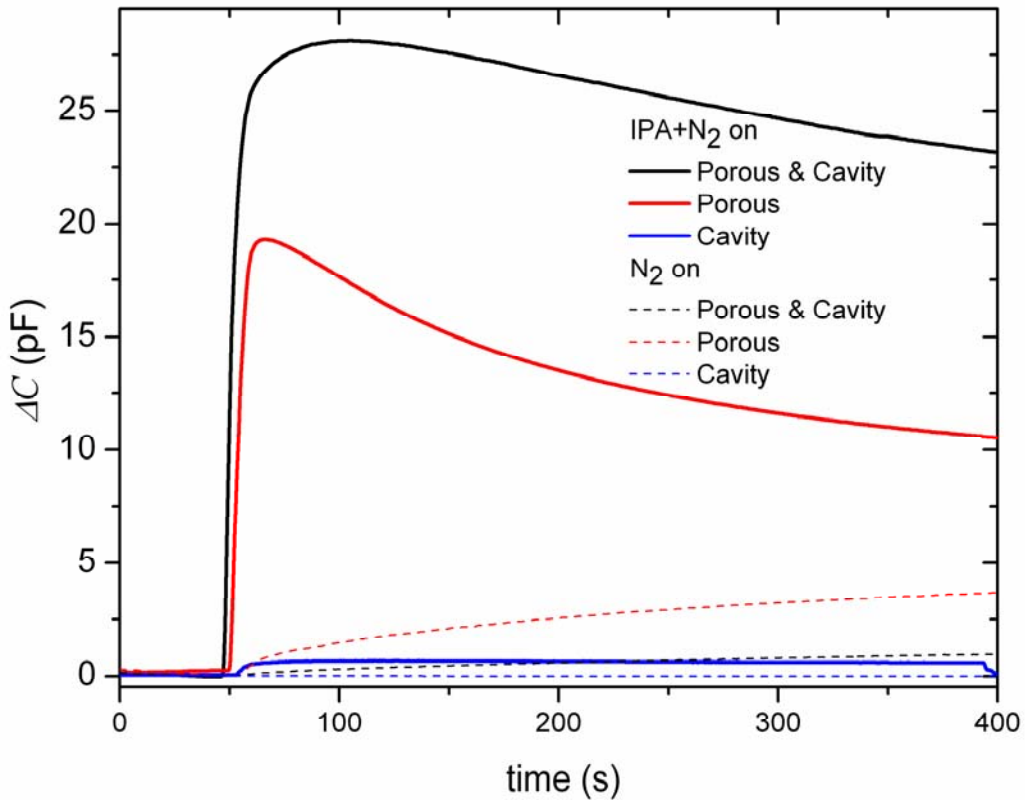

Figure 3.4.2 Response of the arrays of coax with porous dielectric, porous dielectric and cavity and nonporous dielectric and cavity annuli to N_2 and mixture of N_2 and IPA of molar fraction 0.43 unit.

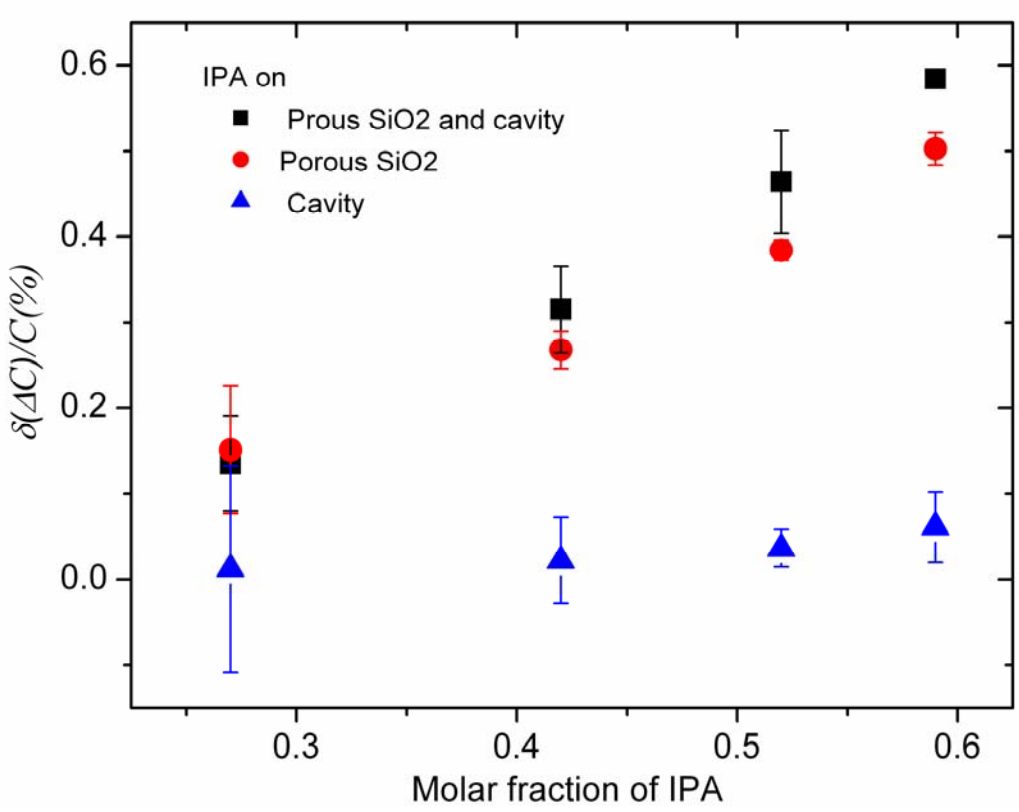

Figure 3.4.3 Fractional change of capacitance of nanocoaxial capacitive sensor arrays with different dielectric annuli for different concentrations of IPA.

In order to ensure consistency for all concentrations, we chose the response at t = 300 s. Figure 3.4.3 shows the percentage of the fractional change in capacitance $\delta(\Delta C)/C$ of coax arrays for various concentrations of IPA, where C is the value of capacitance of the coax recorded just before exposing it to the known concentration of IPA. The data with error bars are averages of three measurements with error bars indicating the standard deviations. For all concentrations of IPA, the response of the device with nonporous dielectric and cavity is smaller than that of the other two devices. This result strongly supports the key role of the porous dielectric in the nanocoaxial capacitive sensor. The response of arrays of coax with nonporous dielectric and cavity annulus is significantly less (> 90 %) than that of coax with porous dielectric and cavity annulus. This finite response can be ascribed to the smaller surface area of the cavity and the nonporous dielectric annulus to that of the porous dielectric and cavity annulus for the adsorption of molecules. However, the recovery time of the device after exposing it with a mixture of N_2 and isopropyl alcohol (IPA) with molar fraction $N_{IPA}/(N_{IPA}+N_{N2}) = 0.43$ unit, where N_{IPA} and N_{N2} are the number of IPA and N_2 molecules in the chamber with the porous dielectric annulus even after purging and pumping of N_2 twice is (>50X) higher than device with cavity annulus as shown in Figure 3.4.4. This could be due to slow desorption of gas molecules from the porous dielectric. Because of the higher recovery time of porous annulus, it takes longer time to functionalize the device for selective detection of molecules. Although the porous dielectric annulus device has higher sensitivity than cavity annulus, the cavity annulus has more stable signal than the former. Furthermore, there are chances of the blockage of porous annulus during the

functionalization and it is unable to detect molecules which size is larger than size of the pore.

In contrast to this, the cavity annulus has following privileges over the porous annulus. Since the cavity annulus has quicker recovery time than porous annulus, it can be functionalized faster than porous. Some selective detections can be possible by simply functionalizing the metal surface of the cavity annulus. The cavity annulus is also suitable in case of detecting molecules having larger size, which could be impossible in the case of porous annulus.

In addition to IPA, the coax arrays with porous dielectric and cavity were employed to detect VOCs with different dielectric constant including methanol, ethanol, acetone and hexane. Figure 3.4.5 depicts the response of three different VOCs namely methanol ($\varepsilon_r = 32.6$), ethanol ($\varepsilon_r = 24.3$) and isopropanol ($\varepsilon_r = 18.3$). As expected, for all concentrations $\delta(\Delta C)$ of coax array for VOC with high dielectric constant is higher than the VOC with low dielectric constant.

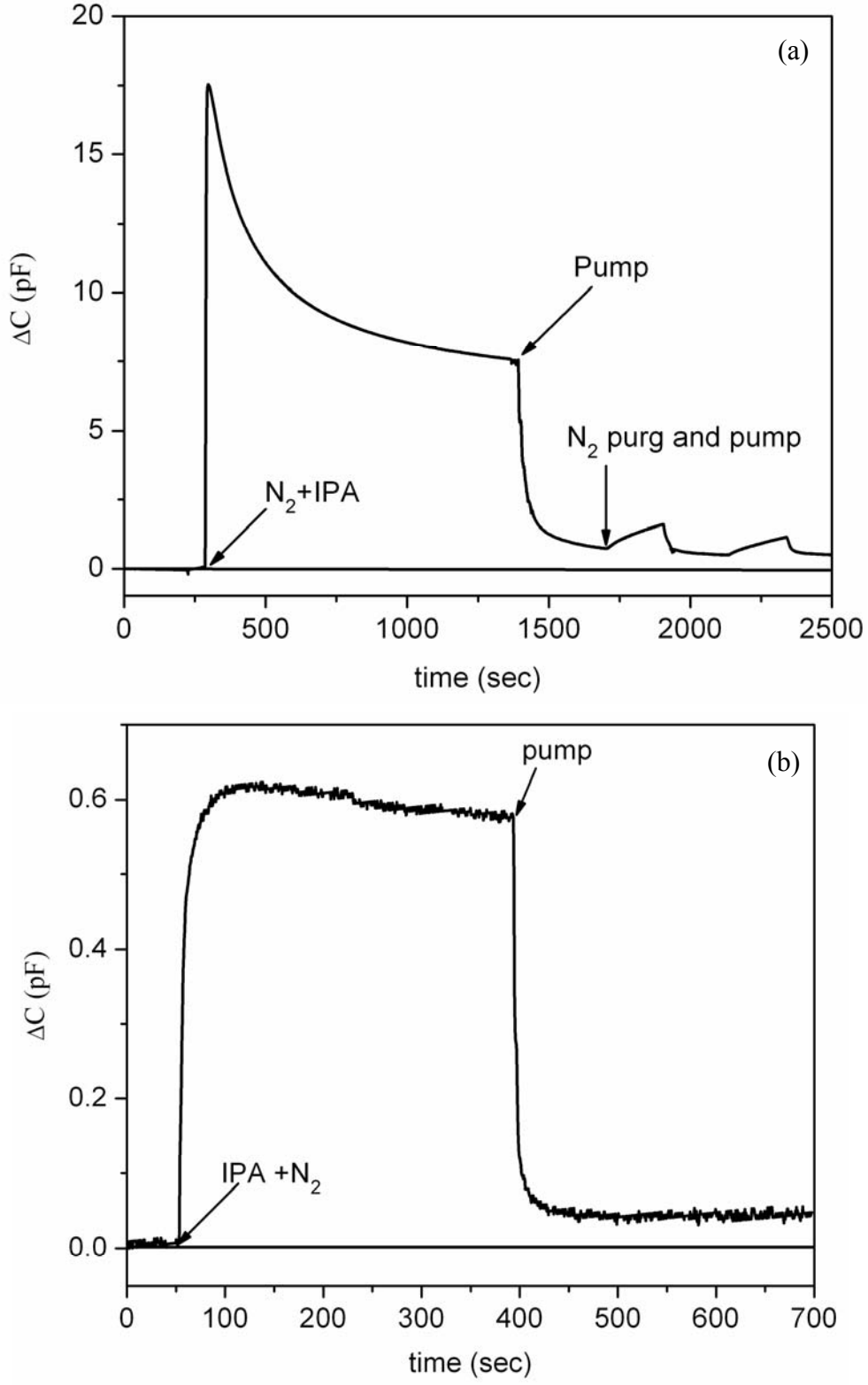

Figure 3.4.4 Recovery time of response of the arrays of coax with (a) porous dielectric and (b) nonporous dielectric and cavity annuli mixture of N_2 and IPA of molar fraction 0.43 unit.

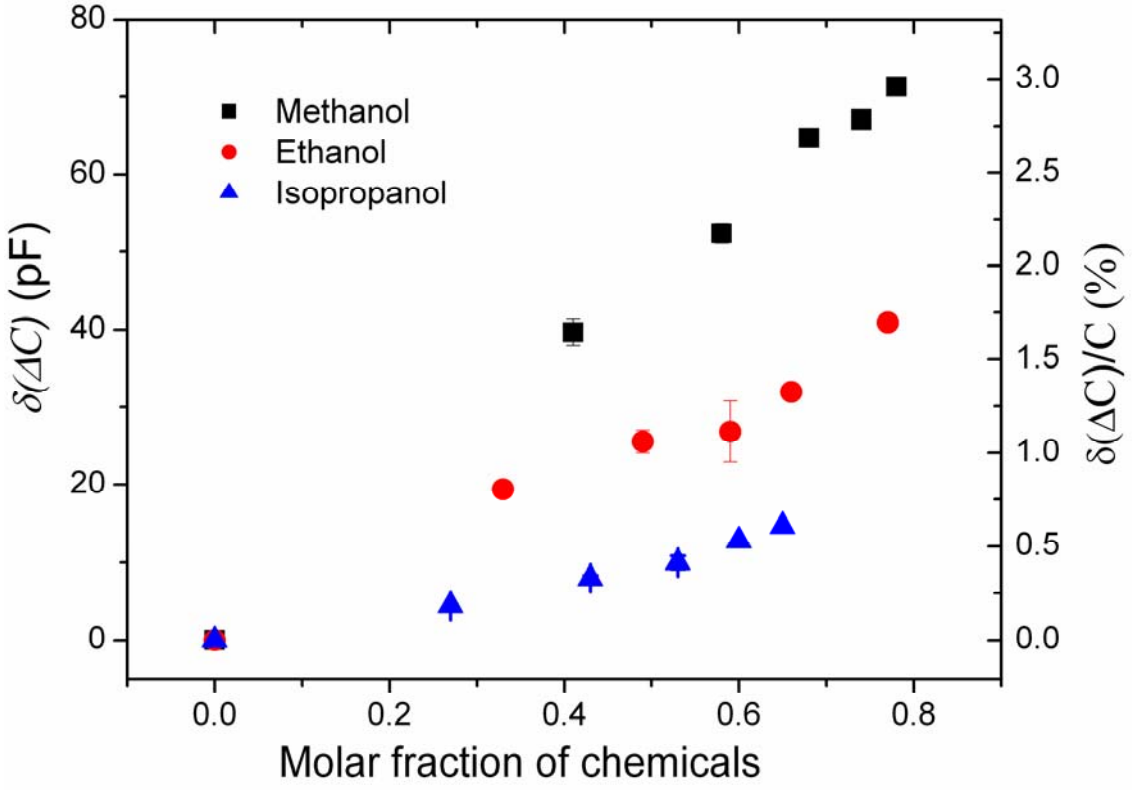

Figure 3.4.5 Concentration-dependent responses for various VOC species from an array of coax with porous dielectric and cavity annulus.

In addition to coaxes with porous SiO_2 annuli, responses of coaxes with different dielectrics were studied, including porous and non-porous Al_2O_3 and a combination of multiple layers of porous Al_2O_3 and SiO_2. As shown in Figure 3.5.4 within the studied range of concentrations of IPA, a coax array with porous Al_2O_3 annulus was found more sensitive than the coax with porous SiO_2 annulus. This could be due to different porosity and surface chemistry of two materials.

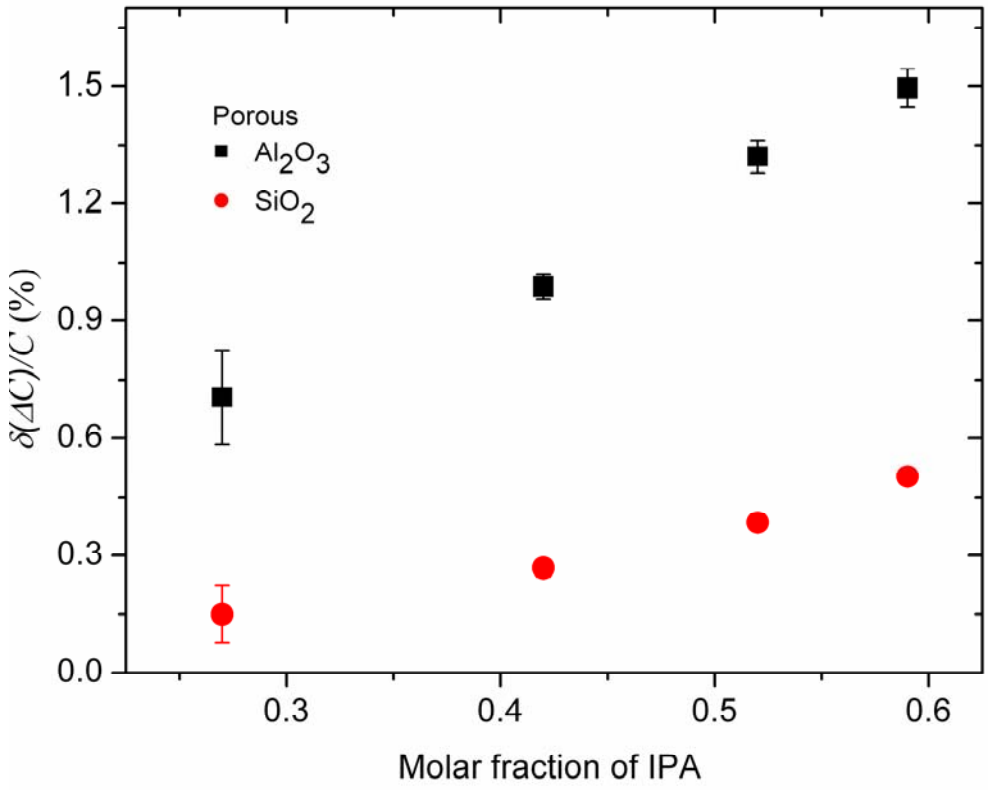

Figure 3.4.6 Responses from coax arrays with different dielectric annuli for different concentrations of IPA.

In addition to coaxes with different dielectrics, we have extended our comparative study for 2D and 3D capacitive sensors. For this, a planar capacitor was made on a Si substrate using the same deposition steps used for fabrication of coax arrays. A thin film of sputter-deposited metal of typical thickness up to 300 nm was found to be permeable for various gas molecules which could be due to the formation of metallic "sponges" during the deposition process [26]. Due to the porous nature of a thin film of deposited metal, we found that it is not necessary to remove the top part of a coax arrays to make a capacitive gas sensor. Henceforth, the capacitive gas sensors discussed are coax arrays without any decapitation. This makes the fabrication process faster and cleaner than before. Figure 3.4.6 shows the response of the 2D and 3D devices for 1 bar of air of humidity ~ 67%. From Figure3.4.6, it can be seen that the sensitivity of both devices is on the same order of magnitude and that the coax has a quicker response than the planar device. The response time τ of the coax structure as calculated using the expression for the charging of a capacitor $\delta(\Delta C)(t) = \delta(\Delta C)_{\infty}(1-e^{-t/\tau})$, where $\delta(\Delta C)_{\infty}$ is the steady state amplitude. The τ for the coax was found to be 200 times faster than for planar structure. This factor could be explained by following two facts: (i) porosity of the outer metal of the coax, due to the nonconformal coating of metal on the coax structure compared to the horizontal planar surface, and (ii) higher surface area of the exposed dielectric of the coax structure. The higher surface area in the 3D structure is thought to improve accessibility and adsorption kinetics of the gas molecules. After these preliminary results, we tried to find the LOD of the nanocoaxial capacitive sensor. To do so, the device was exposed to the chemical gases of ppm and ppb concentrations.

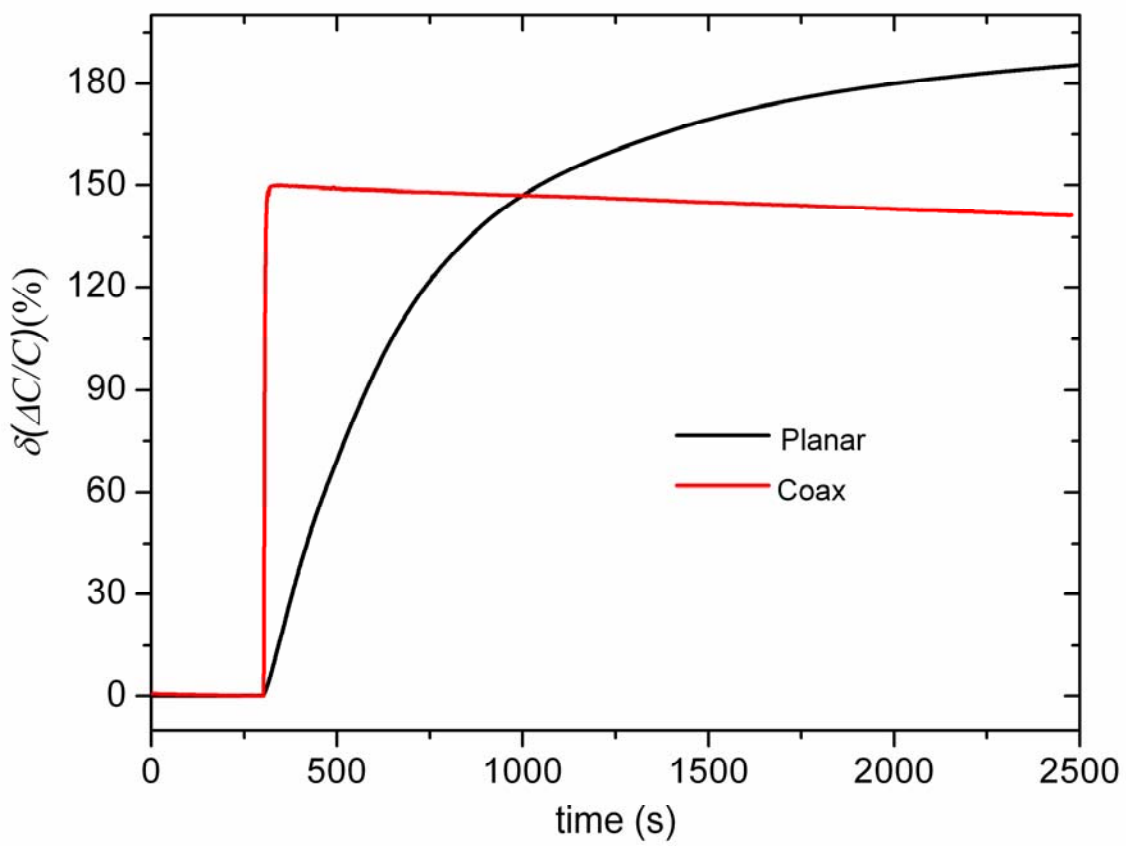

Figure 3.4.7 Response of the planar and nano-coaxial capacitive gas sensor for air with humidity ~ 67%

After these preliminary results, we tried to find the LOD of the nasnocoaxial capacitive sensor. To do so, the device was exposed to the chemical gases of ppm and ppb concentrations. At low concentrations of chemicals, the response of the coax arrays with polymer or Si pillar cores were not reproducible. Figure 3.4.8 shows the response of coax arrays with porous Al_2O_3 annuli for three sets of measurements taken at similar conditions. Moreover, we observed that the capacitance changed randomly with the flow rate of input gas. Different methods were applied to solve these issues such as cleaning of the device by purging and pumping of N_2, heating the device up to 110 ^{0}C after each exposure to chemicals and using a fresh device for each exposure. However, none of these techniques were helpful to resolve the issue.

In addition to capacitive gas sensing, arrays of coaxes or traixes with Au inner electrode and partially hollow annulus with nonporous dielectric were used for the detection of biomolecules such as biotin or streptavidin present in phosphate buffer saline (PBS) solution. Unfortunately, the formation of an electric double layer at the electrode/solution interface [25] makes this device insensitive to any biomolecules present in the aqueous solution. In conclusion, we achieved partial success in this capacitive sensor project. However, using the different transducing methods including optical and electrochemical, coax arrays could be used to make sensitive biosensors. In the next Chapter, we will describe the performance of nanocoax as an electrochemical sensor.

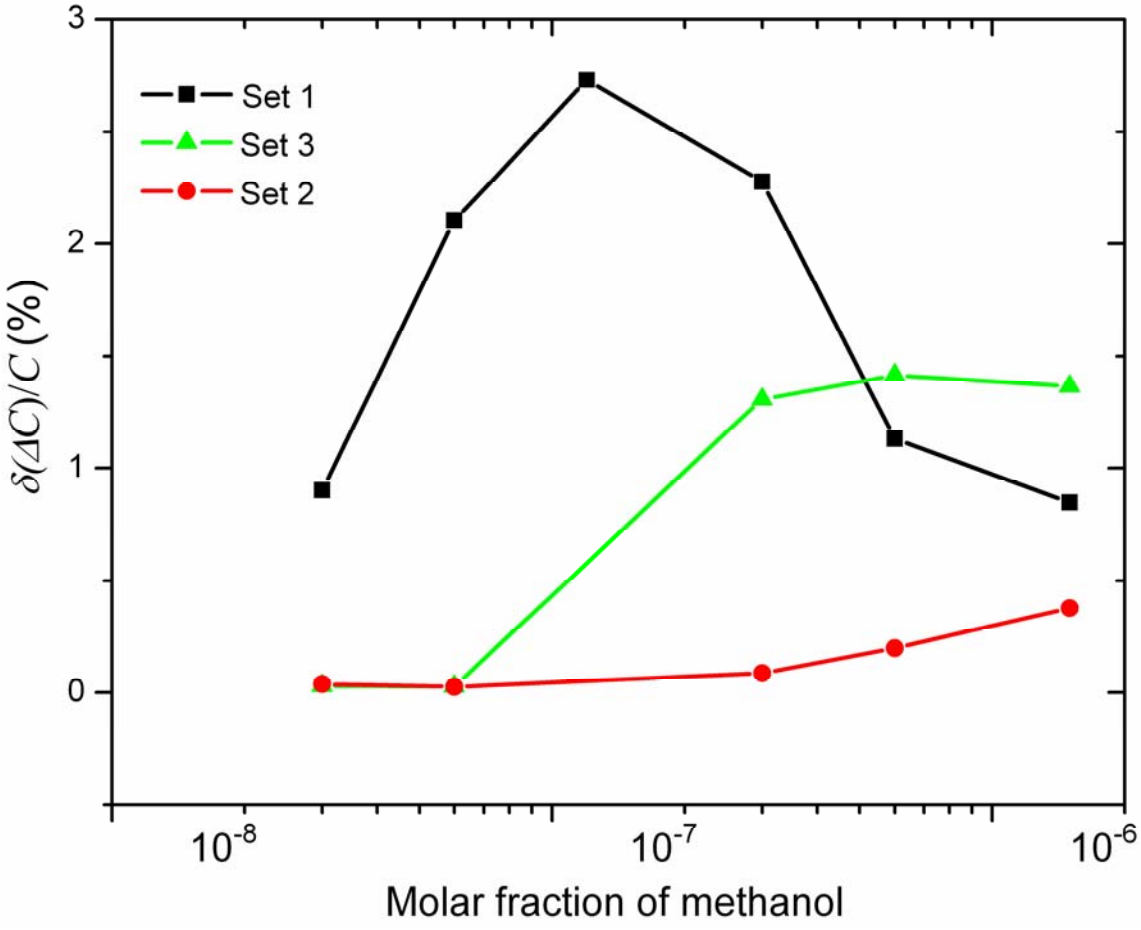

Figure 3.4.8 Response of the coax arrays with porous Al_2O_3 for different sets of measurements. Solid lines are eye-guided lines.

Summary

In this Chapter, we have introduced working principle and experimental setup for nanocoax-based capacitive sensors and measured responses of the sensors for different chemicals that were presented. The sensing performance coax arrays having porous, porous and cavity and nonporous and cavity annulus. Among these devices coax arrays with cavity and porous dielectric annulus were found to be the most sensitive to chemical gases and coax arrays with cavity and nonporous dielectric annulus were least sensitive to the chemicals gases. These results strongly support the key role of the porous dielectric in the coax gas sensor. However, some issues have to be explored, such as instability in the value of capacitance and irreproducibility of the response which were thought to be related with the porosity of the dielectric. Furthermore, our results indicate that, for the detection of gas molecules, the decapitation of the coax to remove the top of the outer metal is not necessary as ~100 nm thick film of sputter deposited metal is permeable to gas molecules.

The device's unique 3D structure affords rapid access of target molecules to the active sensing element (the porous coax annulus) in comparison to conventional 2D planar structures and hence significantly reduces the response time of the devices to gaseous molecules.

Because of the EDL at the electrode/solution interface the coax-based device is insensitive for capacitive detection of the biomolecules present in aqueous solution.

References:

[1] Y. Wang and J. T. W. Yeow, J. Sens. **2009**, (2009).

[2] F.-R. F. Fan and A. J. Bard, Science **267**, 871 (1995).

[3] P. Chen, J. Gu, E. Brandin, Y.-R. Kim, Q. Wang, and D. Branton, Nano Lett. **4**, 2293 (2004).

[4] G. Shekhawat, S.-H. Tark, and V. P. Dravid, Science **311**, 1592 (2006).

[5] A. M. Armani, R. P. Kulkarni, S. E. Fraser, R. C. Flagan, and K. J. Vahala, Science **317**, 783 (2007).

[6] E. S. Snow, F. K. Perkins, E. J. Houser, S. C. Badescu, and T. L. Reinecke, Science **307**, 1942 (2005).

[7] Z. M. Rittersma, Sens. Actuators Phys. **96**, 196 (2002).

[8] R. Fenner and E. Zdankiewicz, IEEE Sens. J. **1**, 309 (2001).

[9] E. Traversa, Sens. Actuators B Chem. **23**, 135 (1995).

[10] A. Tricoli, M. Righettoni, and A. Teleki, Angew. Chem. Int. Ed. **49**, 7632 (2010).

[11] J. Huang, S. Virji, B. H. Weiller, and R. B. Kaner, J. Am. Chem. Soc. **125**, 314 (2003).

[12] T. Zhang, S. Mubeen, N. V. Myung, and M. A. Deshusses, Nanotechnology **19**, 332001 (2008).

[13] X.-J. Huang and Y.-K. Choi, Sens. Actuators B Chem. **122**, 659 (2007).

[14] A. D. McFarland and R. P. Van Duyne, Nano Lett. **3**, 1057 (2003).

[15] M.-I. Baraton and L. Merhari, Mater. Sci. Eng. B **112**, 206 (2004).

[16] J. Kong, N. R. Franklin, C. Zhou, M. G. Chapline, S. Peng, K. Cho, and H. Dai, Science **287**, 622 (2000).

[17] F. Schedin, A. K. Geim, S. V. Morozov, E. W. Hill, P. Blake, M. I. Katsnelson, and K. S. Novoselov, Nat. Mater. **6**, 652 (2007).

[18] A. Ponzoni, E. Comini, I. Concina, M. Ferroni, M. Falasconi, E. Gobbi, V. Sberveglieri, and G. Sberveglieri, Sensors **12**, 17023 (2012).

[19] Z. Dai, L. Xu, G. Duan, T. Li, H. Zhang, Y. Li, Y. Wang, Y. Wang, and W. Cai, Sci. Rep. **3**, (2013).

[20] I. Bargatin, E. B. Myers, J. S. Aldridge, C. Marcoux, P. Brianceau, L. Duraffourg, E. Colinet, S. Hentz, P. Andreucci, and M. L. Roukes, Nano Lett. **12**, 1269 (2012).

[21] H. Zhao, B. Rizal, G. McMahon, H. Wang, P. Dhakal, T. Kirkpatrick, Z. Ren, T. C. Chiles, M. J. Naughton, and D. Cai, ACS Nano **6**, 3171 (2012).

[22] D. P. Broom and K. M. Thomas, MRS Bull. **38**, 412 (2013).

[23] J. Batey and E. Tierney, J. Appl. Phys. **60**, 3136 (1986).

[24] G. C. Schwartz, Y.-S. Huang, and W. J. Patrick, J. Electrochem. Soc. **139**, L118 (1992).

[25] M. Yi, K.-H. Jeong, and L. P. Lee, Biosens. Bioelectron. **20**, 1320 (2005).

Chapter 4

Nanocoax for Electrochemical Sensor

4.1 Introduction

Lithography based micro/nanofabrication, commonly referred to as "silicon technology", had long been mostly limited to the field of electronics. [1] In recent decades, it has found widespread use in other areas of science and technology. This trend is driven by a combination of two complementary factors: (1) Micro/nanofabrication is becoming more accessible to a widening pool of potential users. Specifically, investment costs have decreased dramatically, and clean room facilities have become standard fixtures in many research labs and institutions, and (2) Advances in micro/nanofabrication techniques allow fabrication of increasingly complex structures, continually creating opportunities for new fundamental experiments and technologies. Here, we will focus on electrochemical sensing using micro/nanofabricated devices, whose paired electrodes have a separation gap on the order of nanometers. Considerable effort has been directed toward increasing target-sensitivity in electrochemical sensors (ES) by developing nanogap electrodes that can provide real-time sensitive detection of chemical and biological agents. An ES with arrays of nanogap electrodes can be formed by connecting a large number of nanogap ESs operating in parallel. This can lead to further improvement in the performance of a nanogap electrode ES because the total output signal is the sum of signals from all connected individual ESs. Lithographic techniques such as electron beam [2–5], dip pen [6], transmission electron beam ablation [7] and focused ion beam (FIB) milling [8,9] can be used to make nanoscale gap electrodes.

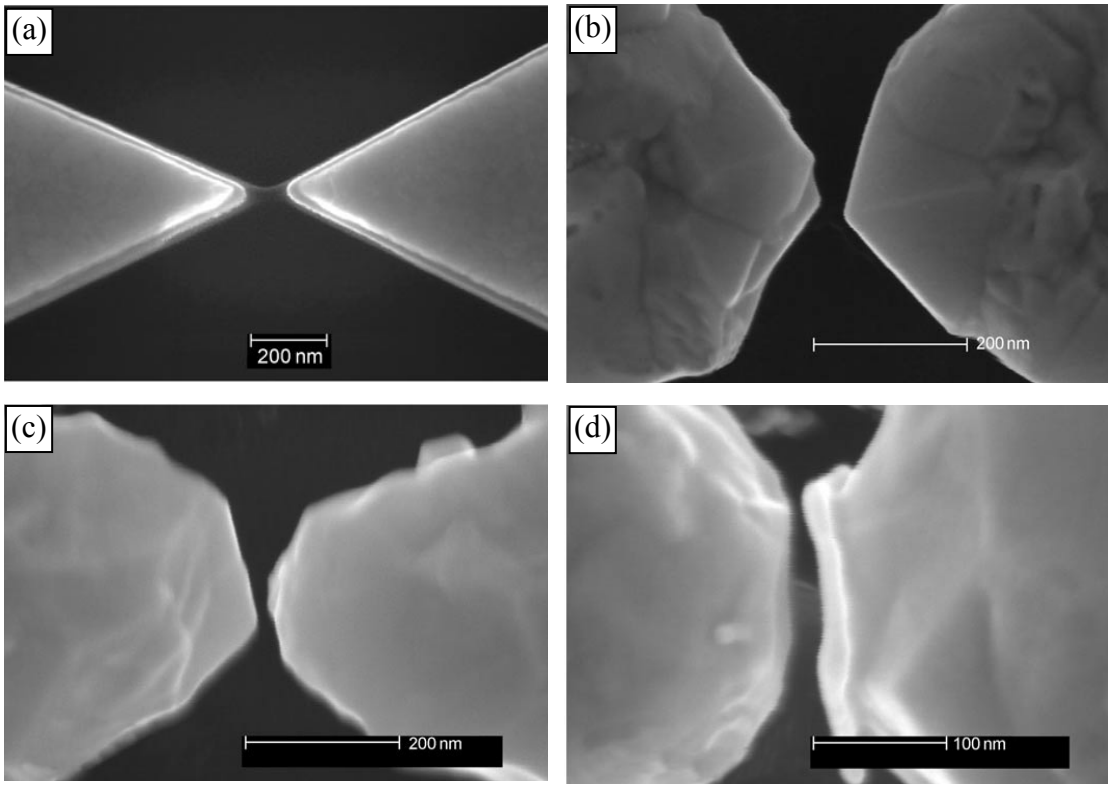

Figure 4.1.1 Example of SEM images of (a) 2D Au electrode pair of 200 nm gap made using EBL, (b-d) electrode pairs prepared by electrodepositing Au on the electrodes similar to (a) with gap distance 26, 16 and 7 nm respectively. From [10].

However, these methods are commonly used for planar, two dimensional structures, and are inevitably serial, costly, and time consuming processes. Other techniques such as electromigration [11,12], electrochemical deposition [13,14], and electro-breakdown [15] are simpler and faster than the aforementioned techniques for planar nanogap electrode fabrication, but have limited flexibility in controlling the size and shape of the gap between the electrodes. The details of different methods used to fabricate nanogap electrodes have been discussed extensively in the literature [16]. Figure 4.1.1 shows the SEM images of nanogap electrodes made using different fabrication techniques. Although different methods have been developed to make discrete pairs of nanogap electrodes, it remains a challenge to fabricate highly ordered arrays of nanogap electrodes with confined geometries over a large area, and to do so in a reproducible and cost-effective manner.

We have developed a soft lithography based simple and reliable method for fabricating highly ordered arrays of electrodes with well-defined nanogaps over a large area for use in ES devices, maintaining the advantage of nanogap sensing while overcoming many of the limitation of previous devices. [17]. No conventional lithographies (photo- or electron beam) are employed in the fabrication. The device is composed of an array of vertically-oriented nanocoaxes with hollow annulus, into which an analyte solution can ultimately fill and be detected as depicted in Figure 4.2.1 (a). We fabricated ESs using the two electrodes of the nanocoax as the integrated working electrode (WE) and counter electrode (CE) as shown in Figure 4.1.2 (b). ES arrays with various electrode gaps were prepared by changing the thickness of the dielectric layer and then removing it from annulus of the coaxes.

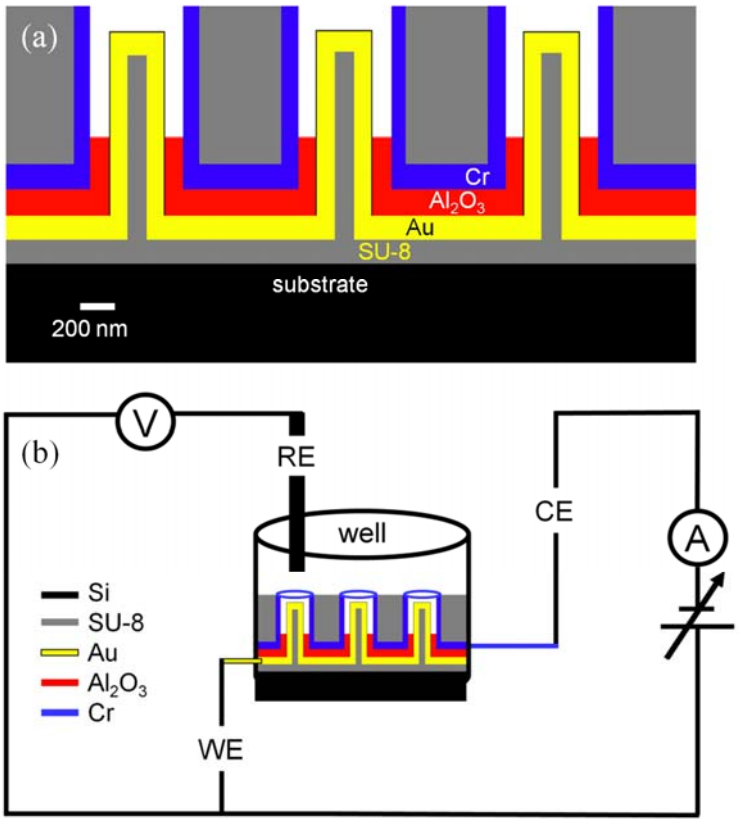

Figure 4.1.2 Schematic representations of (a) a partially hollowed nanocoax array, and (b) a coax-based ES made using inner and outer electrodes of the coax array as WE and CE, respectively, of an ES.

The resulting effect on the Faradic current, i.e. a current due to the transfer of electrons between electrode and electrolyte, was examined via differential pulse voltammetry (DPV). In this Chapter, we describe the experimental set up, measurement technique and results of nanocoax-based ES. Furthermore, a comparative study of 3D coaxial and 2D ESs with electrodes separated on the nm and mm-scale, respectively, will be presented.

4.2 Experimental Set-up and Measurements Techniques

To make nanocoax-based ES's, we create a reservoir for liquid on the coax arrays using a custom-made polypropylene gasket as shown in Figure 4.2.1. A three-electrode ES was then configured using the inner and outer coax electrodes as the WE and CE, respectively, and a Ag/AgCl electrode immersed in the reservoir as a reference electrode (RE) as shown in Figure 4.1.2 (b). For comparative study, we also constructed ESs with planar Au WEs, Pt CEs, and Ag/AgCl REs, which had the same projected WE area as the coax arrays (1.8 mm^2). The reservoir was filled with a redox reagent, 1 mM ferrocene carboxylic acid (FCA) in phosphate buffered saline (PBS) solution. Electrochemical characterization was performed using a potentiostat (Reference 600, Gamry Instruments). For analytical purposes, DPV was employed as the electrochemical measurement technique. The main virtue of DPV technique is its excellent precision, high sensitivity, and wide dynamic range of detection. The common characteristic of DPV involves varying the potential with a series of the potential pulses of fixed amplitude superimposed to a slowly changing base potential (V) to an electrode and then monitoring the resulting current (I) flowing through the electrochemical cell. Figure 4.2.2 shows applied potential waveforms and their respective current response for the two pulses in a DPV measurement.

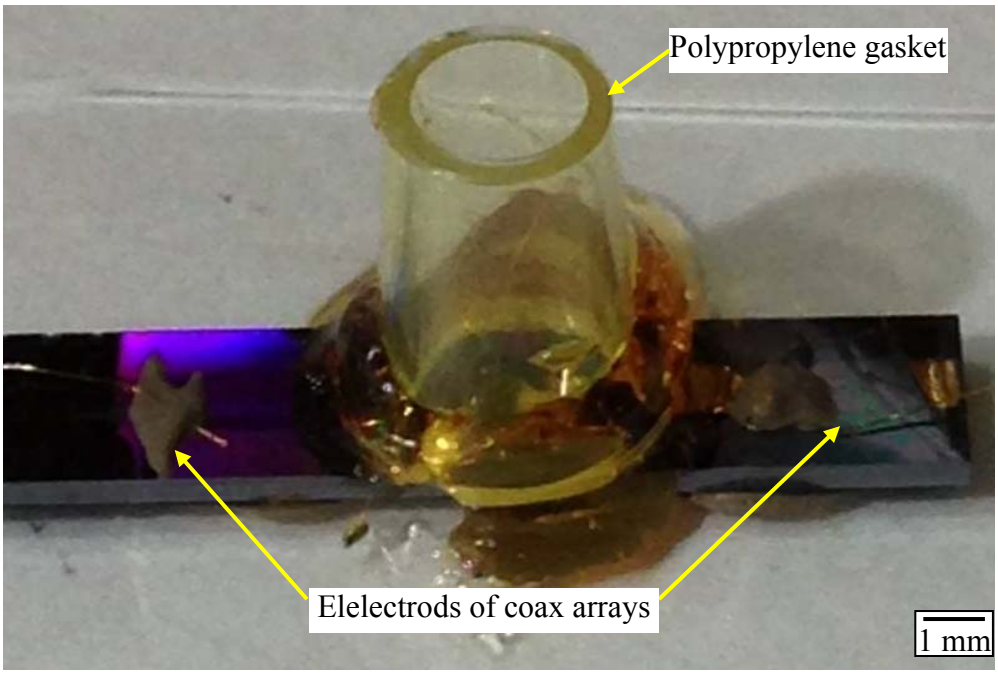

Figure 4.2.1 Photograph of a polypropylene gasket used to create a reservoir for liquid on top of nanocoax arrays.

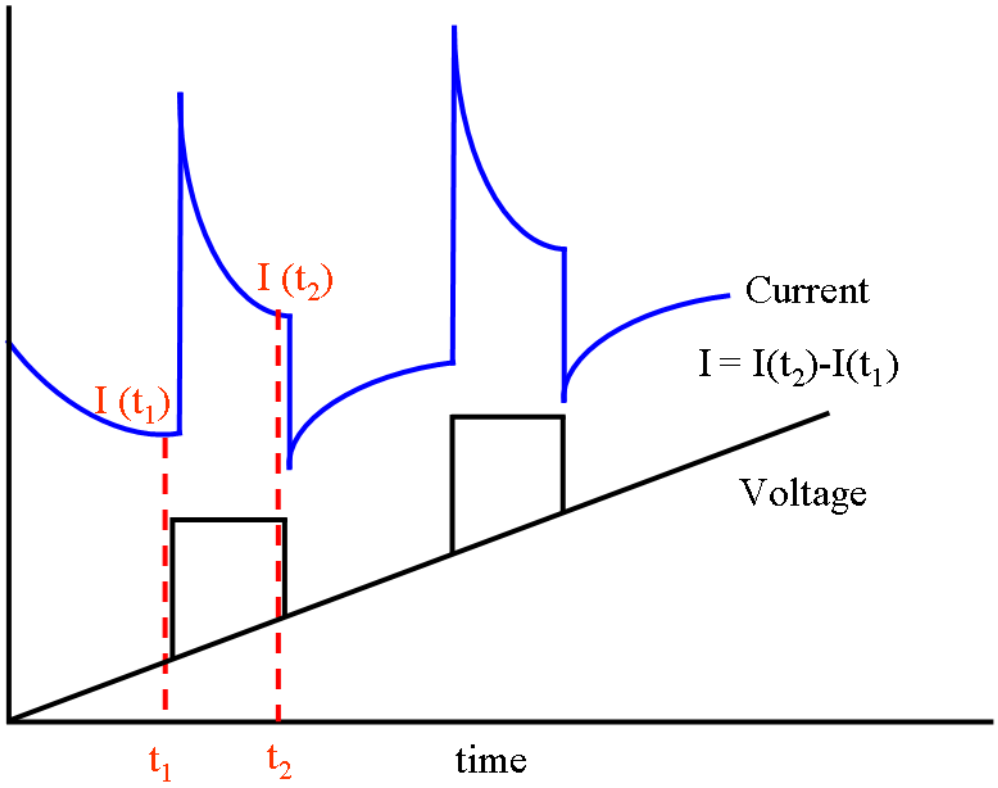

Figure 4.2.2 Schematic of waveforms and measurement scheme for DPV. In each cycle, pulse current samples were taken at the times indicate by the dotted lines. The differential faradic current (I) is the difference between these two values of currents, i.e. $I=I(t_2)-I(t_1)$.

Usually, a pulse with amplitude 10 to 100 mV, duration 1 to 100 ms and the interval between pulses typically 0.1 to 5 seconds was used. The current measurement is made at two points for each pulse; the first point of time (t_1) just before the application of the pulse and the second (t_2) at the end of the pulse. These sampling points are selected to allow for the decay of the nonfaradaic (charging) current. The difference between current measurements (I) at these points of each pulse is determined and plotted against the base potential (V). There are two advantages to measuring the difference in current. First, it increases the discrimination of the faradic current against the charging current, since any residual charging current is subtracted out. Second, the shape of the current response is a symmetric peak as shown in Figure 4.2.3. If we consider chemical reduction at an electrode, then for potentials more positive than the redox potential, both the forward and reverse currents are zero. Therefore, the difference in current is also zero. At potentials more negative than the redox potential, the current is diffusion-controlled, and the potential pulse has no effect. Hence, the forward and reverse currents are equal and the difference in current is again zero. The largest difference between the forward and reverse currents (and hence the largest current response) occurs at the redox potential. Details of DPV technique can be found in many standard textbooks [18,19].

The current due to a reduction (cathodic current) of the electrode is, by convention, assigned a positive sign. The current due to an oxidation of an electrode is assigned a negative sign. An important parameter in DPV which can be used to identify species of the chemicals is the width of the peak at half height, $W_{1/2}$ depicted in Figure 4.2.3.

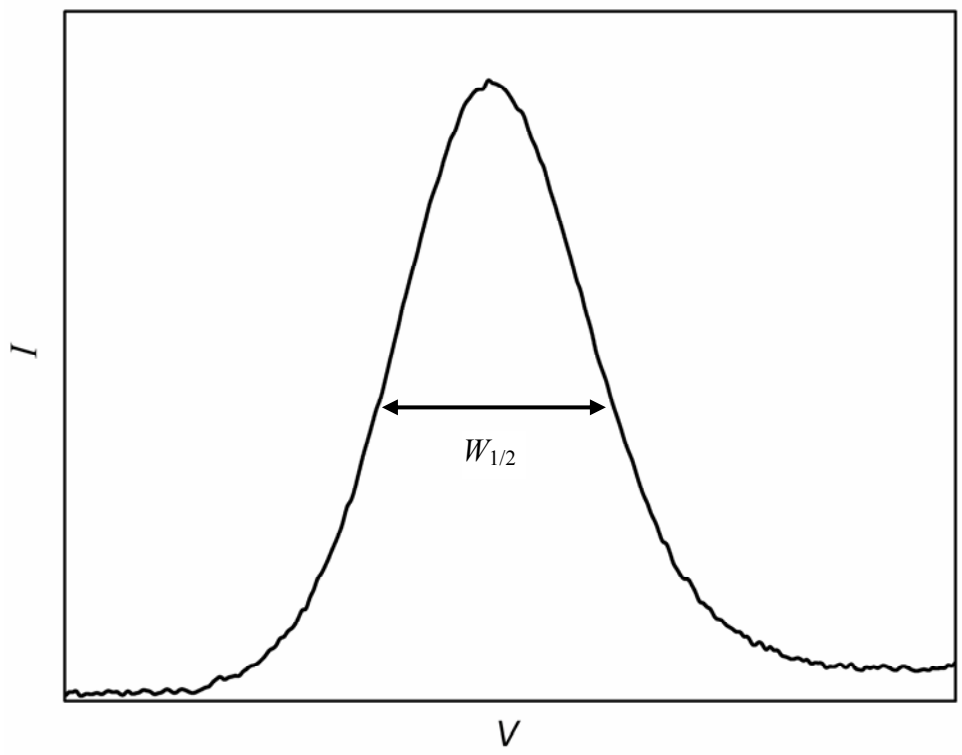

Figure 4.2.3 Typical waveform in DPV technique.

This is related to the number, n, of electrons transferred from an electrolyte to an electrode via

$$W_{1/2} = 3.52RT/nF$$

where R is the molar gas constant (8.3144 $J\ mol^{-1}K^{-1}$), T is the absolute temperature (K), and F = Faraday constant (96,485 C/equiv). At 25 ^{0}C, the values of $W_{1/2}$ for n =1, 2 and 3 are 90.4, 45.2 and 30.1 mV, respectively. In comparison to other voltammetry techniques such as normal pulse voltammetry, the sensitivity gain in DPV does not come from an enhanced faradic response. Instead, the improvement comes from a reduced contribution from the background current [18]. A factor which plays an important role in reducing the background charging current in pulse techniques, especially at higher measuring speeds, is the *RC*-time constant of an electrochemical cell. The effect on the time constant and, hence, the sensitivity of the ES due to the use of an array of hollow nanocoaxes will be presented in the following discussion.

4.3 Performance of Nanocoax-Based vs. Planar ESs

Reduction of the distance between the electrodes of an ES has received considerable attention as this is thought to increase the sensitivity by improving the Faradic-to-capacitive signal ratio and decrease the response time by reducing the solution resistance [18,20–23]. Here, we employed the soft lithography technique to make a nanocoax-based ES with well-defined nanogap electrodes. We have fabricated ESs with the gap between electrodes ranging from 50 to 400 nm. Using the DPV technique, the effect of electrode separation on subsequent ES performance was investigated. As mentioned earlier, one of the advantages of a nanogap configuration is it reduces the

response time of an ES. The response time depends on the RC-time constant, which is defined by the factor R_uC_d, where R_u is the uncompensated resistance, and C_d is the double layer capacitance. The maximum value of uncompensated resistance of an electrolyte solution of conductivity σ, confined between two electrodes separated by a distance d, is $R_u = d/\sigma A$, where A is the area of the inner electrode. There is an electric double layer capacitance density C_d due to the charged species and oriented dipoles at the metal-solution interface as shown in Figure 4.3.1, whose typical value is in the range 10-40 $\mu F/cm^2$ [18]. For a physiological solution such as PBS of bulk conductivity 0.14-0.18 S/m [24], the value of uncompensated resistance R_{ui} for a nanocoax with 250 nm diameter inner electrode, 200 nm annulus width, and 500 nm annulus depth, is $R_{ui} \sim 3$ MΩ. The number of coaxes within a 1.5 mm diameter array area is $n = 1.21 \times 10^6$. For resistive analysis, coax arrays can be treated as a parallel combination of n resistors, with an equivalent resistance $R_u = R_{ui}/n \sim 1$ Ω. For such arrays, we calculate the value of the double layer capacitance to be $C_d \sim 0.1$ μF. With these values, the cell RC-time constant of a nanocoax ES within the 1.5 mm diameter area employed is $\sim 10^{-7}$ s. For comparison, the RC-time constant of a planar cell with the WE and CE separated by mm-scale distance is $\sim 10^{-3}$ s.

Following the standard practice of using a DPV pulse time ~10 times greater than the RC-time constant, the coax-based ES reduces the limit of the experimental time scale to 10^{-6} s (1 μs) for the commonly used biological medium PBS. Such a rapid time scale could only be achieved for other microstructures by using a medium with much higher electrical conductivity [25].

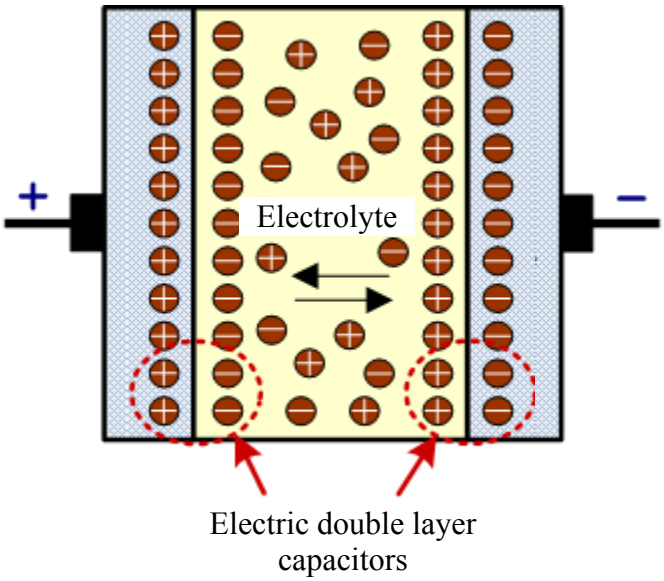

Figure 4.3.1 Schematic of electric double layer capacitors at the interfaces between electrodes and electrolyte.

Thus, the low value of the time constant of the coax-based ES provides the unique ability to study voltammetric signals in media with low conductivity.

In principle, an ES with a time scale ~1 μs can also be used to measure redox potentials of highly reactive intermediates, measure the rate constant of rapid heterogeneous charge transfer, and analyze complex mechanisms including chemical steps [26–30].

To observe the effect of electrode (WE-CE) separation on Faradic current, DPV measurements were carried out using initial and final potentials 0.0 and 0.5 V, respectively, pulse size 50 mV, pulse time 0.05 s, step size 2 mV, and sample period 0.1 s, for the redox chemical 1 mM FCA in PBS. Measured values of current of coax-based ES with different electrode gaps (coax annulus widths) and ES with planar WE are as shown in Figure 4.3.2. In all cases, the coax-based devices displayed higher current than the planar control. Figure 4.3.2 shows that all coax and planar ESs had a well-defined peak at 280 mV *vs*. (Ag/AgCl), which corresponds to the redox reaction of FCA. The width of the peak at half height is $W_{1/2}$ ~92 mV, close to a previously reported value of 90.4 mV [18,26] for a one electron process at 25 ^{o}C. This indicates that our devices can be used to collect the information on the number of electrons transferred from an electrolyte to electrode. In Figure 4.3.3, we show the dependence of the peak value of the current on the coax-based WE-CE separation $d = r_2 - r_1$, where r_1 is the outer radius of the inner coax conductor and r_2 the inner radius of the outer coax conductor. For consistency of measurement for all values of electrode separation, we subtracted the background current at 0.1 V from the peak current value, indicated as ΔI in Figure 4.3.3; this has less than a 1% effect on the overall result.

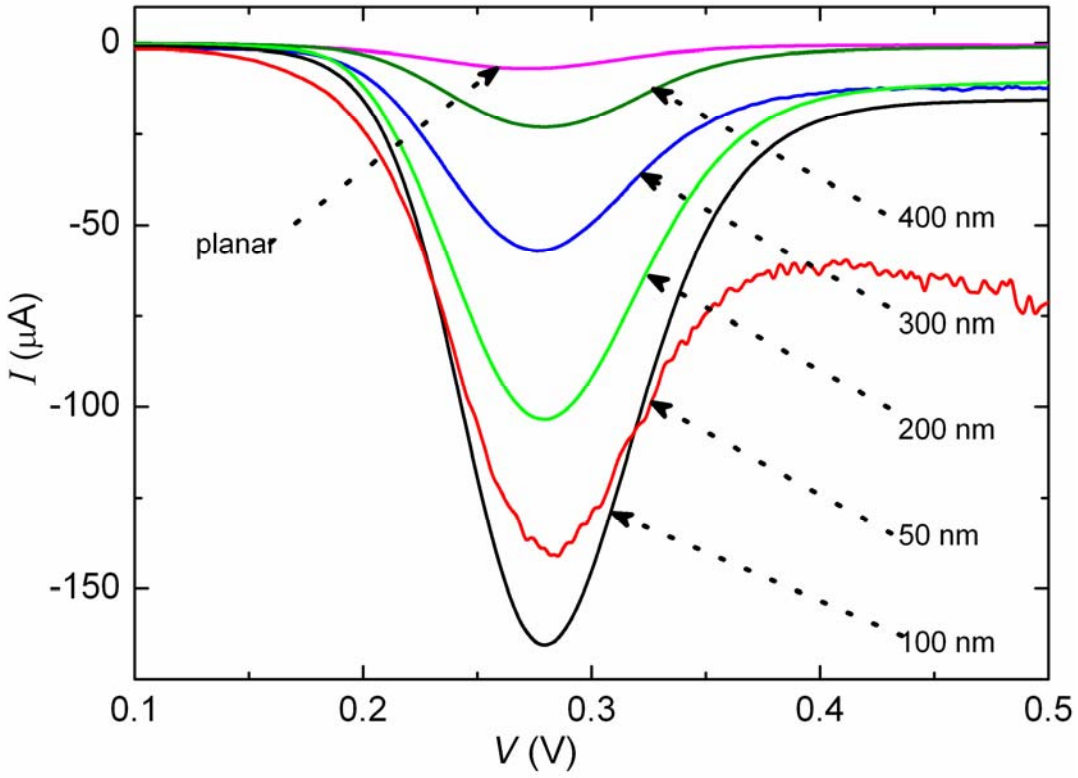

Figure 4.3.2 DPV signal from different annulus thickness, coax-based electrochemical sensors. Current in nanocoax-based ESs with 50 to 400 nm gaps between WE and CE, plotted *vs*. WE potential. Data for a planar ES control having millimeter-scale WE-CE gap is also shown.

The value of the peak current increases with decreasing distance between electrodes up to a certain value then it begins to decrease with decreasing distance. This can be explained by assuming a linearly-varying concentration gradient of the redox molecules within the diffusion layer between the two electrodes. Under such conditions current in the device can be expressed as

$$I = \frac{FAD(Cr_1 - Cr_2)}{(r_2 - r_1)}$$

Where F = Faraday constant

A = Area of inner electrode of radius r_1

D = Diffusion constant of the redox chemical

Cr_1 and Cr_2 are concentrations of redox chemical at the surfaces of electrodes of radii r_1 and r_2, respectively.

At the peak current the maximum number of molecules (or all molecules) on the surface of electrodes should be oxidized or reduced. At these maxima, the concentration of the redox molecules at the surface of the inner electrode is zero and the current in circuit can be written as

$$I = \frac{FAD(Cr_2)}{(r_2 - r_1)}$$

Under these conditions, current can be expressed as $I \sim (r_2\text{-}r_1)^{-1}$ [18]. But if the gap between the electrodes is smaller than size of redox molecules, no molecules can be diffused into the annulus. In this situation the value of faradic current should be zero as there are no molecules to produce the Faradaic current. Therefore, there should be a turning point in the peak value of current with respect to the gap of electrodes at which

current starts to decrease with the gap between electrodes. This could account for the smaller value of peak current at 50 nm than 100 nm gap of electrodes.

The ratio of current density for the coax-based ES to that for the planar device is also shown in Figure 4.3.3. The coax–based ES with 100 nm electrode gap is seen to have a signal nearly two orders of maghnitude greater than that of the conventional, planar ES (*i.e.* $J_{coax}/J_{planar} = 90$), while the noise level in each ES is approximately the same. We suggest that the observed improvement in signal-to-noise ratio in the coax-based ES compared to the planar ES, and with decreasing electrode gap in the coax-based ES, is due to two effects: rapid diffusion of redox species between the closely spaced electrode surfaces, and the large number of nanocoaxes in our device.

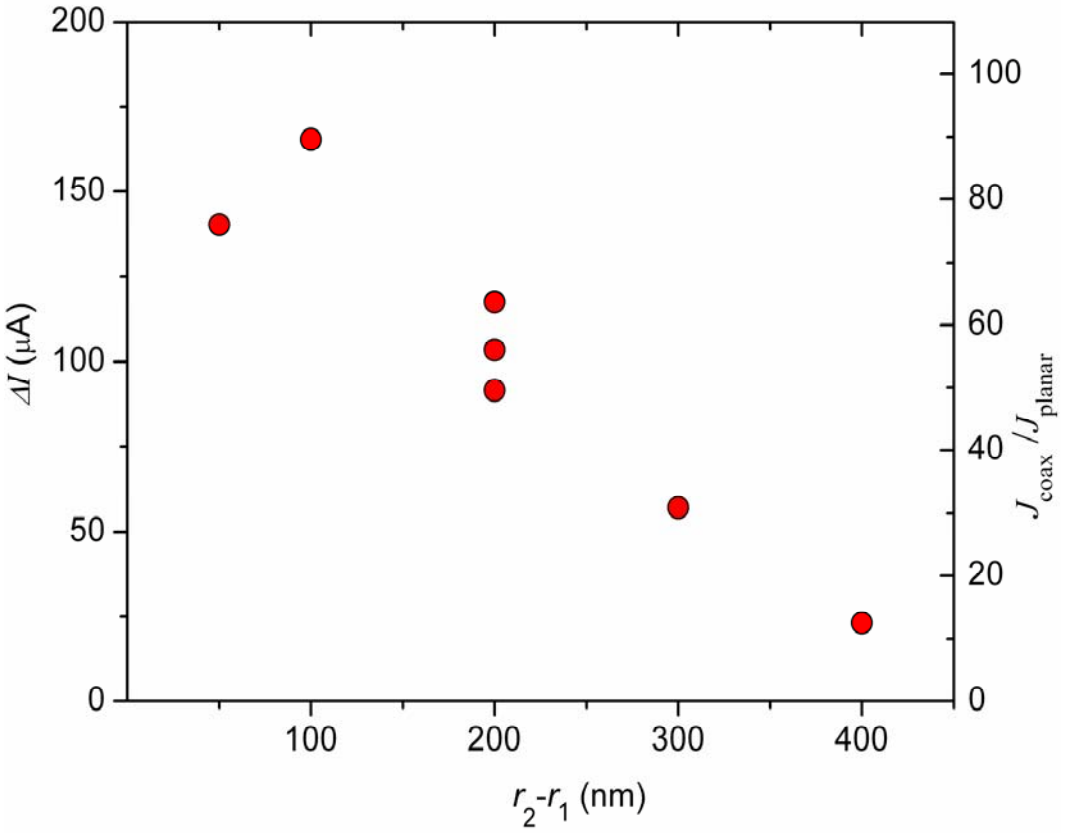

Figure 4.3.3 Difference between peak current and current at 0.1 V WE potential vs. gap (r_2-r_1) between WE and CE for nanocoax-based ES. Right axis: Ratio of current density in coax-based ES cell to that in planar ES vs. gap between WE and CE of nanocoax-based ES.

The small gap between the WE and CE facilitates efficient diffusion of redox molecules between electrodes, with the result that species reduced at the counter electrode rapidly return back to the working electrode and vice versa, providing positive feedback to the signal [31–33]. This process presents a large flux of redox species between electrodes, which yields a higher value of current compared to a sensor with a large electrode gap. The small dimensions of each nanocoax and their close spacing is such that each 1.5 mm^2 area ES device contains more than 10^6 nanocoaxial ESs operating in parallel (whose signals are thus additive). Also, in this coaxial structure, the inner electrode is circumferentially surrounded by the outer electrode, such that molecules primarily diffuse radially between the electrodes as shown in Figure 4.3.4. In combination, this means that we are within the linear diffusion regime such that the electrochemical processes are not mass diffusion limited, a problem found in other nanogaps ES devices [4]. This is evidenced by a conventionally-shaped cyclic voltammogram (Figure 4.3.5), in contrast to peak-shaped curves in the planar-diffusion dominated nanodevices [4].

For both the nanocoax-based ES and the planar ES, we studied the effect on the DPV signal due to multiple uses of the devices. Unlike the case of the planar ES, the signal from nanocoax-based ES degraded with the number of runs of DPV as shown in Figure 4.3.6(a). As can be seen in Figure 4.3.6(b), the peak value of the current decreases exponentially as a function of the number of runs of DPV according to the function $I = \alpha_0 + \alpha \exp(-x/\xi)$ with $\alpha_0 = 1.36 \times 10^{-5}$ A, $\alpha = 1.23 \times 10^{-4}$ A, $\xi = 2.99$ and x = number of runs.

Cleaning of the devices between two successive runs of DPV with DI water and organic solvents (isopropanol, methanol) followed by baking at high temperature 110 ^{0}C did not improve the degradation effect associated with the multiple times use of the nanocoaxial devices. The degradation in signal in successive runs of DPV could be due to of the lack of exchange of the liquid within annuli of the nanocoaxes.

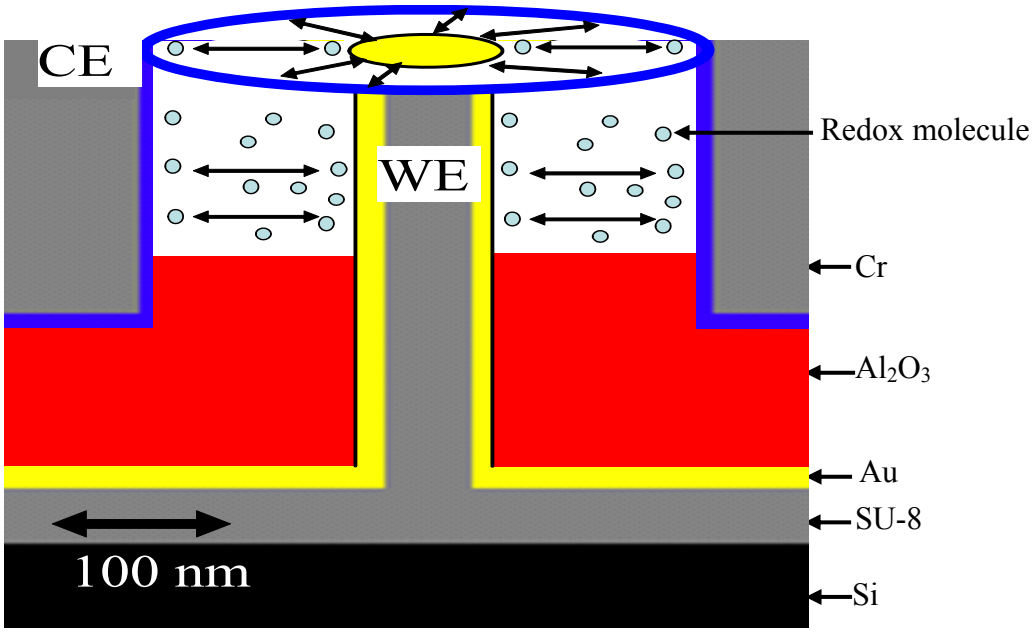

Figure 4.3.4 Schematic showing the radial diffusion of molecules in a nanocoax.

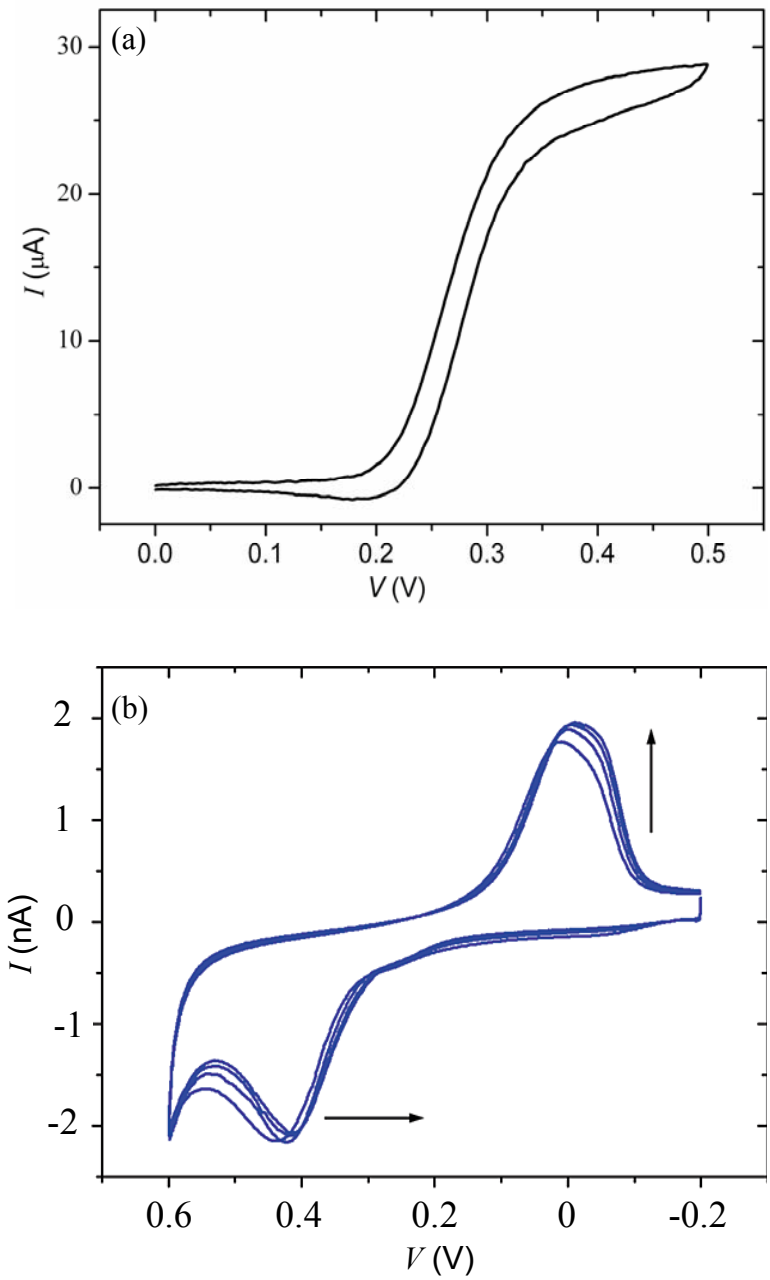

Figure 4.3.5 (a) CV of 1 mM of FCA using the nanocoax arrays ES with 200 nm electrode gap. CV was done after multiple runs (15 times) of DPV on the same device. (b) CV of 1 mM of FCA in a nanodevice having planar nanoelectrodes with separation gap of 200 nm [4]. Differences in the values of the redox potential in (a) and (b) could be due to different reference electrodes. Ag/AgCl and Pt were used as reference electrodes in (a) and (b), respectively.

After certain number of runs of DPV, the signal of the nanocoax-based ES becomes saturated. It is important to note here that the saturated value of the signal from the coax arrays is comparable to initial signal from planar ES having same projected area. This degradation effect suggests that for sensitive detection of chemicals, the nanocoax-based ES may be only beneficial as a single use device. However, a nanocoax-based ES was employed multiple times for the detection of different concentrations of p-aminophenol or 4-aminophenol (4AP). 4AP is the product of p-aminophenyl phosphates (pAPP) in presence of enzyme alkaline phosphates (ALP). pAPP is a commonly used substrate for electrochemically-based, enzyme-linked immunoassays [34].The relevant biochemistry for the above reactions can be represented by the following chemical equations [35] :

(a)

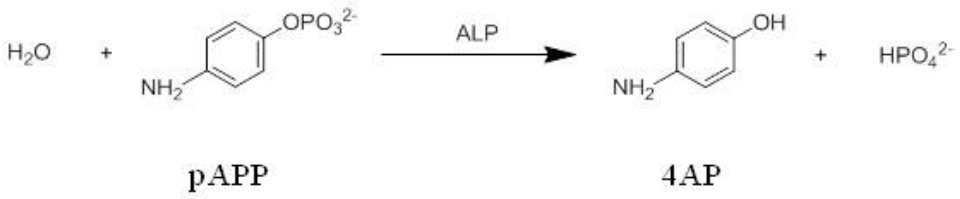

Hydrolysis reaction of pAPP to 4AP catalyzed with AP.

(b)

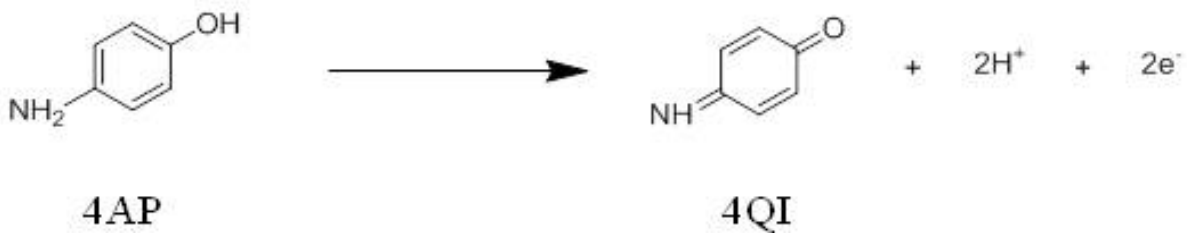

Oxidation reaction of (4AP) to (4QI)

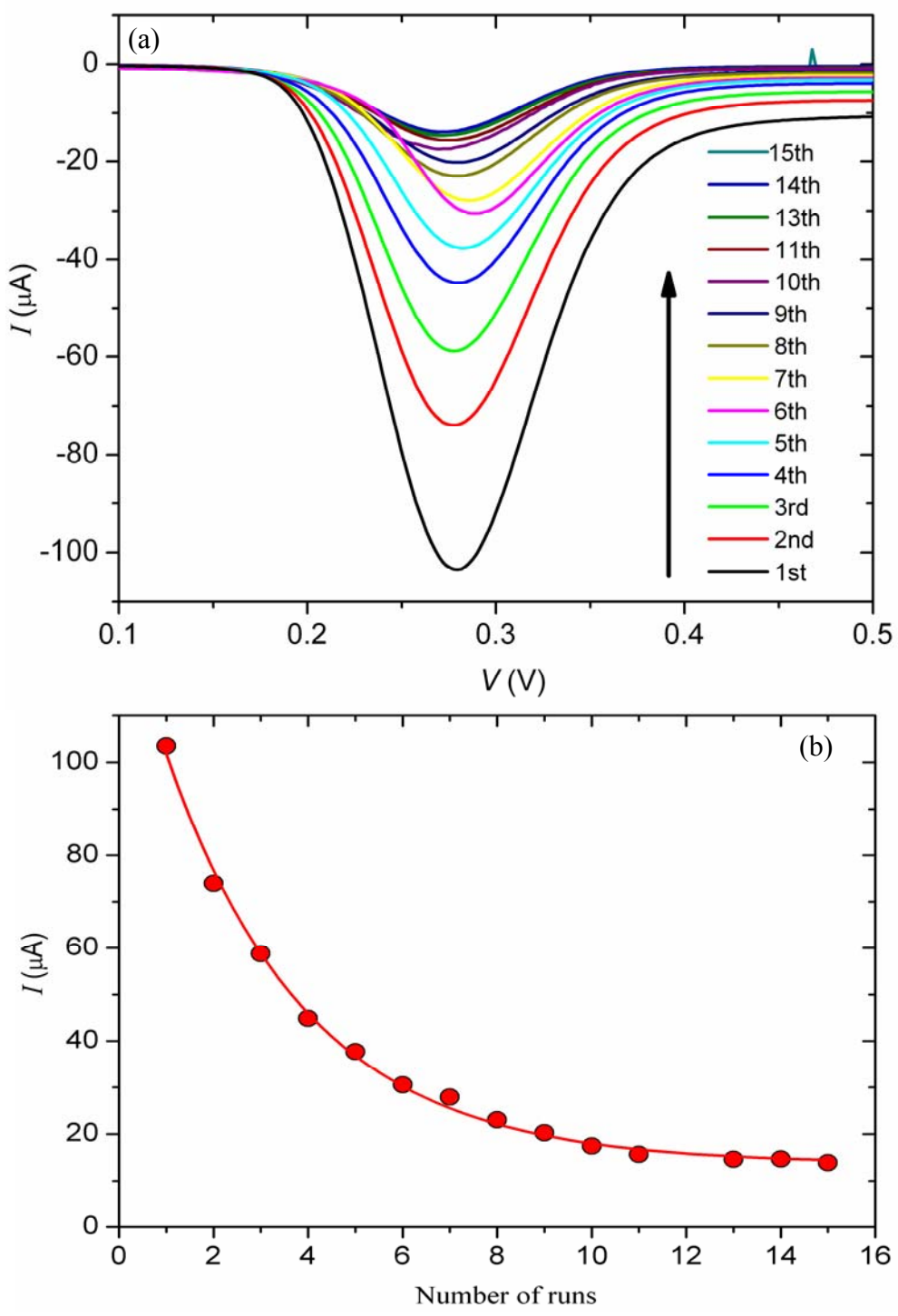

Figure 4.3.6 (a) DPV signal at multiple runs of DPV on nanocoax–based ES with electrode gap 200 nm. (b) Peak value of current in (a) vs. number of run with fitted line (solid).

We investigated the capability of nanocoax-based and planar ESs to detect 4AP in response to a series of dilutions of ALP. In electrochemical immunosensors, the ALP enzyme converts pAPP to an electrochemically active product which can be detected and quantified [35]. DPV responses for different concentrations of ALP enzyme in 1μg L^{-1} pAPP solution using a nanocoaxial device and planar control are as shown in Figures 4.3.7 (a) and (b). The nanocoax device was subjected to the 15 runs of DPV using FCA before ALP titration.

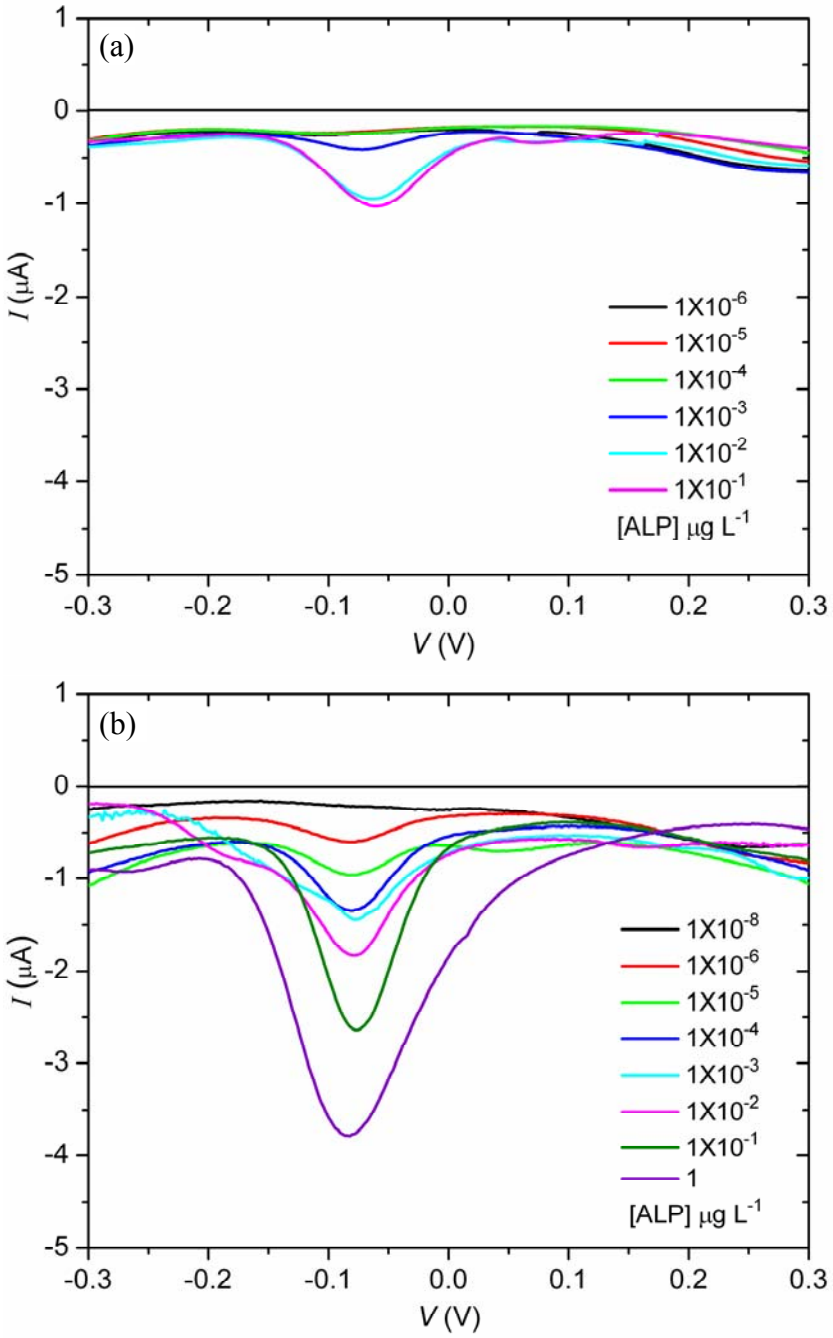

Figure 4.3.7 DPV responses for different concentrations of ALP enzyme in 1μg L^{-1} pAPP solution in (a) planar and, (b) nanocoax based electrochemical sensors.

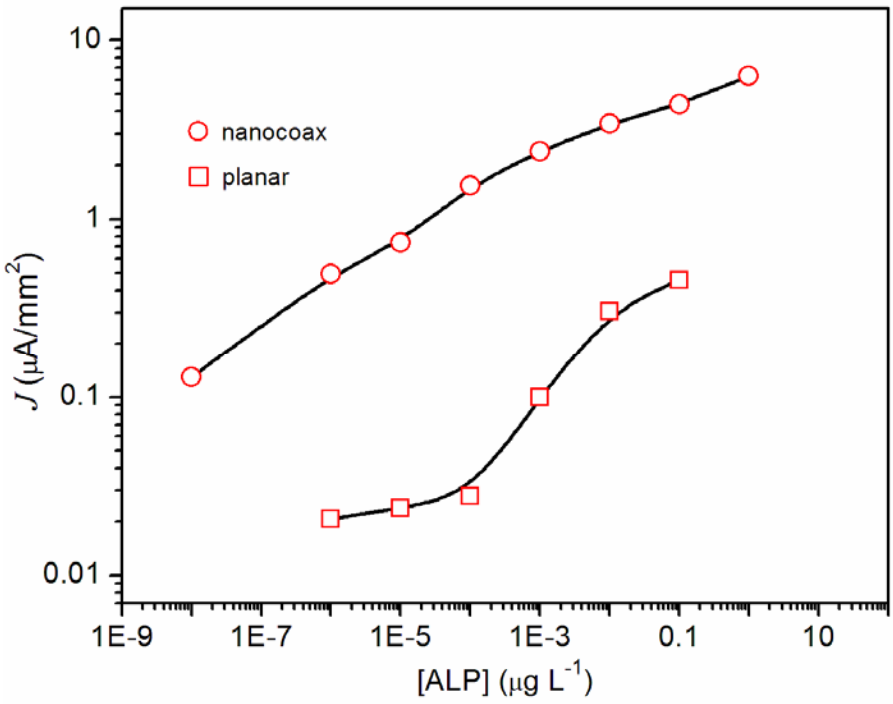

Figure 4.3.8 Comparison of DPV response to ALP titration in nanocoax and planar Au ESs. Solid lines are eye-guided lines.

DPV responses to ALP titration are shown in Figure 4.3.8 as the current generated per unit surface area for different concentrations of ALP enzyme in 1μg L^{-1} pAPP solution. ALP activity is present in nanocoax architectures due to their increased sensitivity and linear dynamic range over the planar gold architectures. This is consistent with results shown in Figure 4.3.3. The LOD of the nanocoax-based ES has to be determined. However, preliminary result for the LOD of the nanocoax–based ES is comparable with the previously reported LOD of the planar glassy carbon electrode [36]. This preliminary result and the knowledge that degradation in DPV response occurs in our coax device (Figure 4.3.6) indicate that we could further improve the performance of nanocoax-based ESs if we used virgin nanocoax arrays for each concentration of ALP. Figures 4.3.9 (a)-(c) show DPV responses of three independent sets of measurements. Each set of measurements includes the DPV response of planar control and nanocoax-based ESs with virgin nanocoax arrays for each concentration of ALP.

(a)

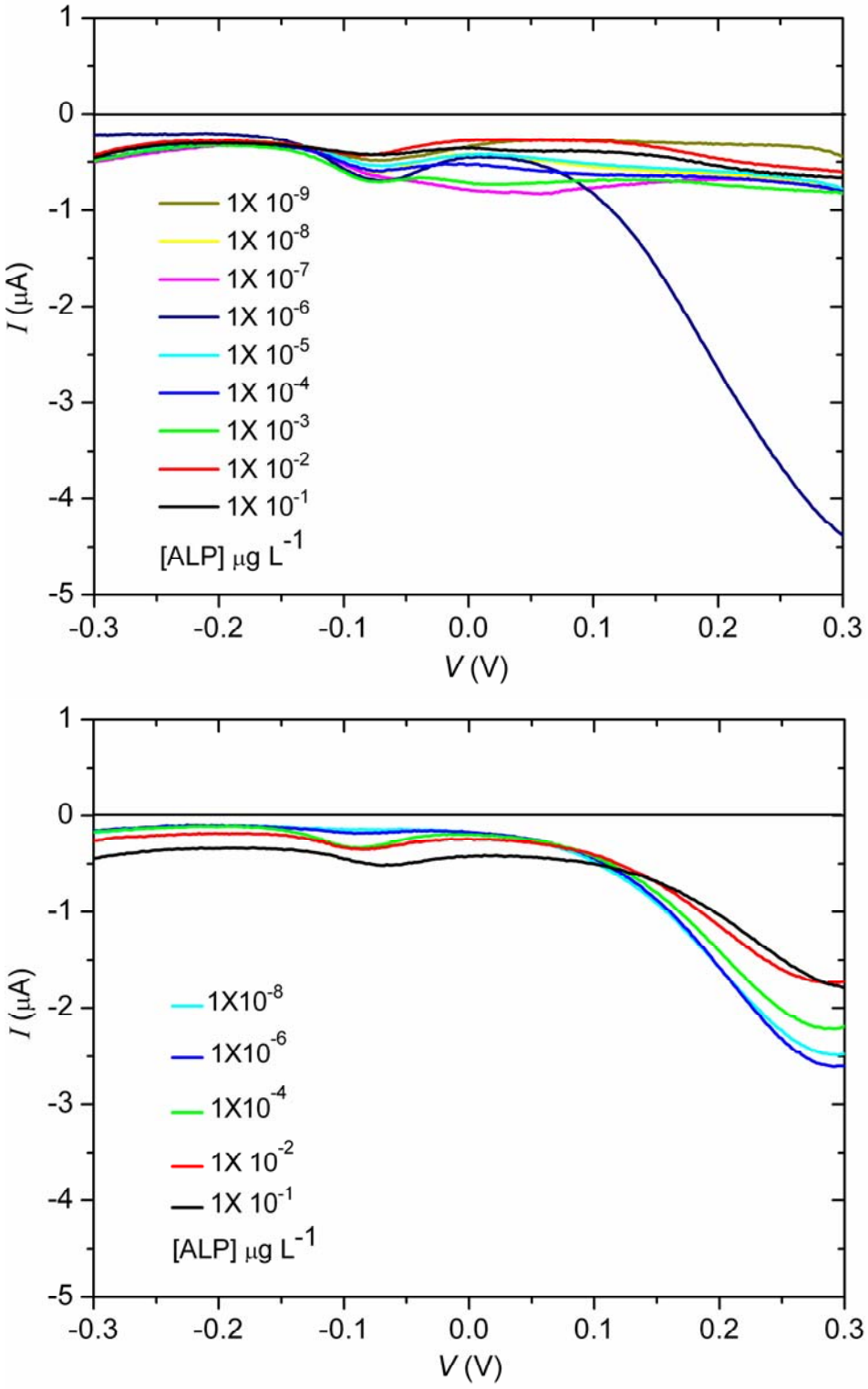

Figure 4.3.9 (a) DPV responses for different concentrations of ALP enzyme in 1µg L^{-1} pAPP solution in planar (top) and nanocoax based electrochemical sensors (bottom).

(b)

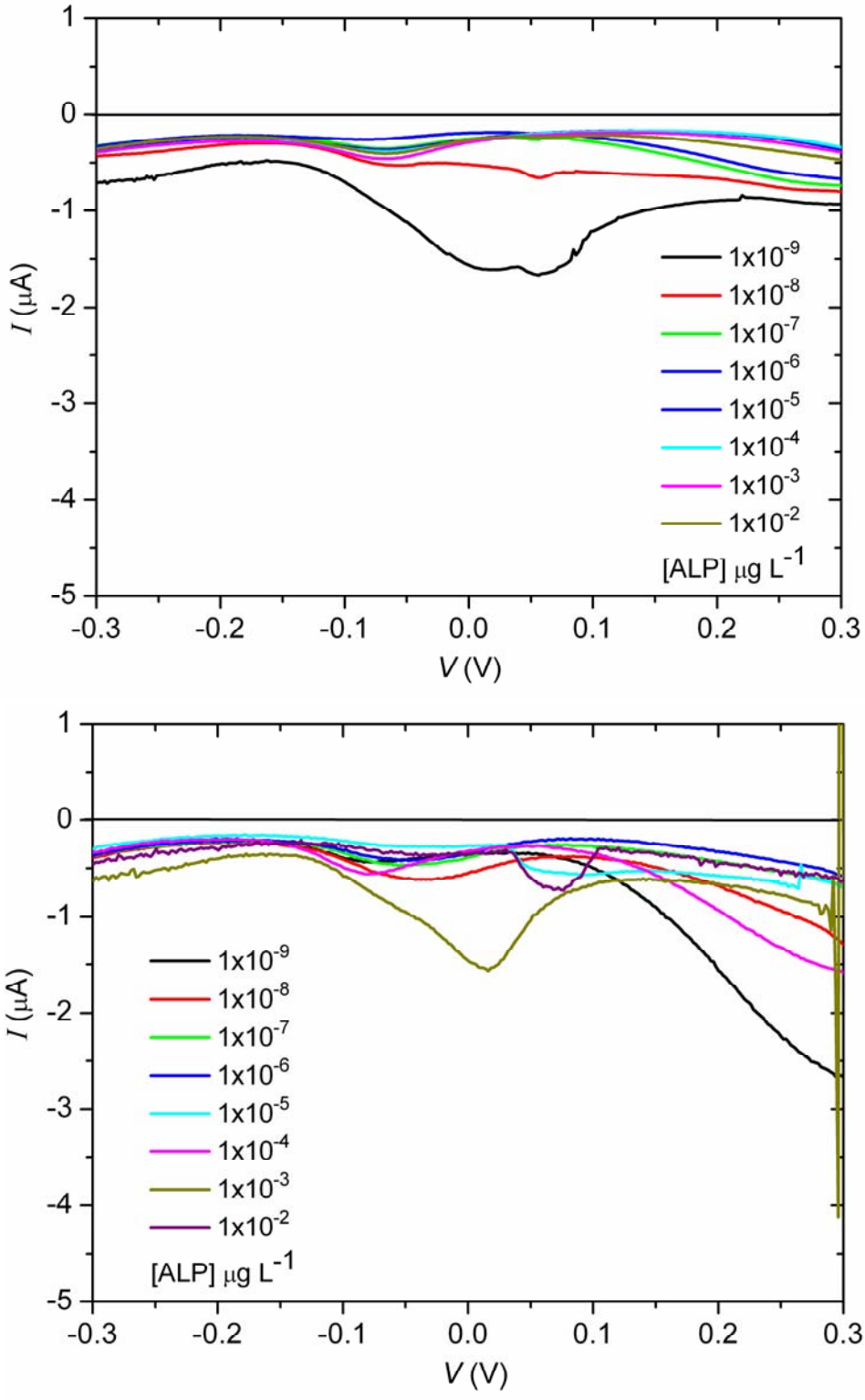

Figure 4.3.9 (b) DPV responses for different concentrations of ALP enzyme in 1μg L^{-1} pAPP solution in planar (top) and nanocoax based electrochemical sensors (bottom).

(c)

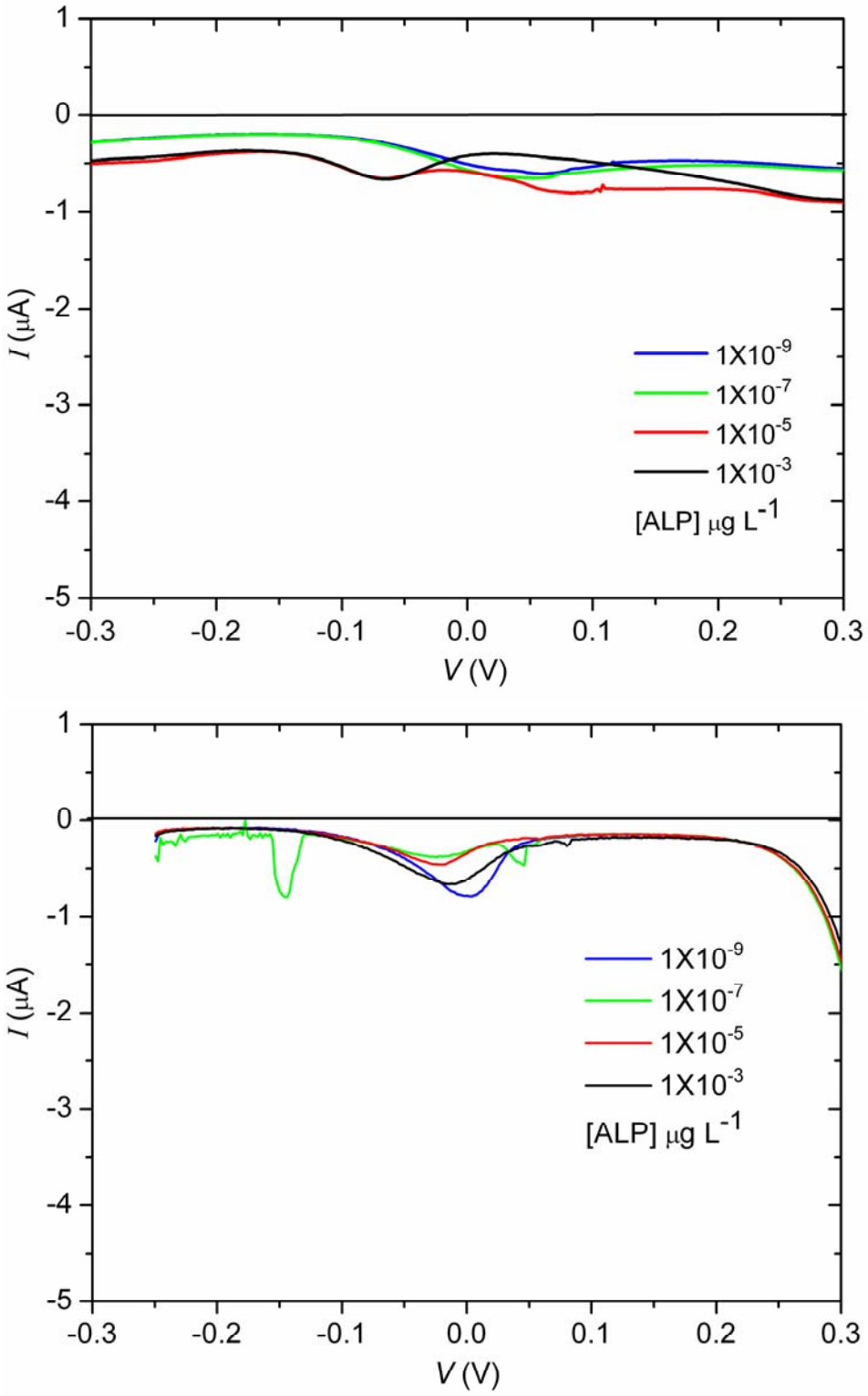

Figure 4.3.9 (c) DPV responses for different concentrations of ALP enzyme in 1μg L^{-1} pAPP solution in planar (top) and nanocoax based electrochemical sensors (bottom).

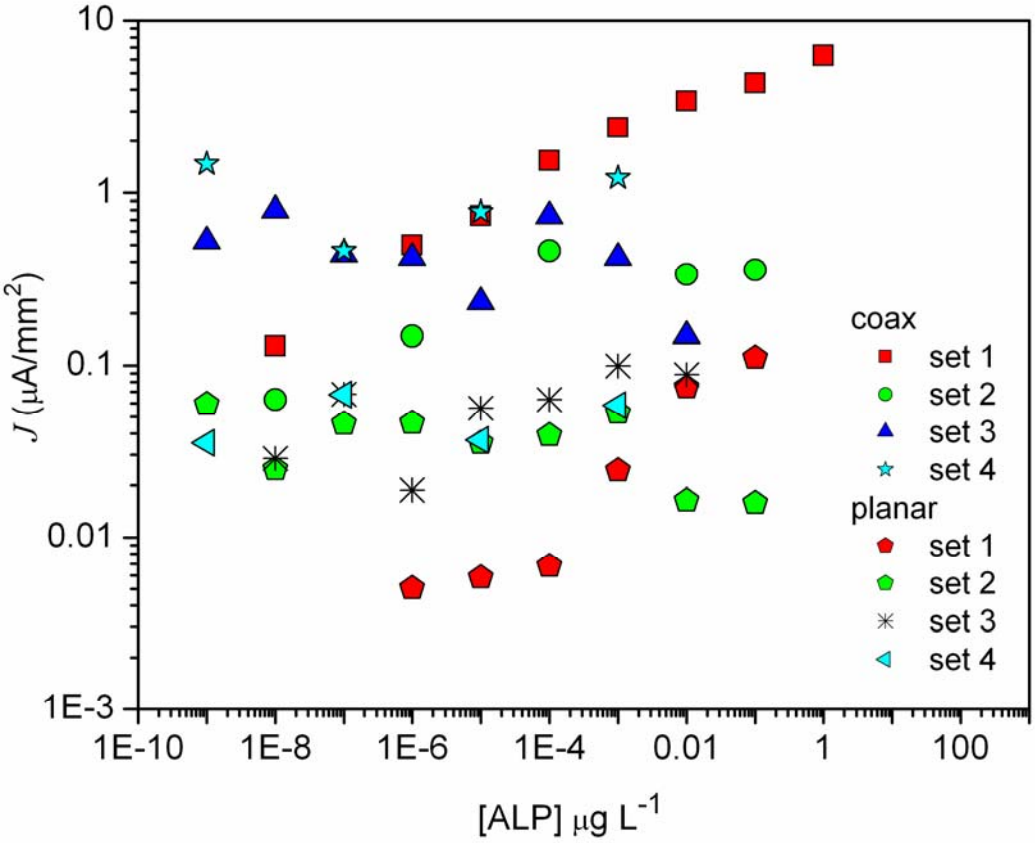

Figure 4.3.10 Comparison of DPV response to ALP titration in 4 independent set of measurements in nanocoax and planar Au ESs.

Figure 4.3.10 represents 4 sets of measurements of the peak value of current in coax-based ESs and planar controls. As mentioned earlier, in the first set of measurements peak value of current changed with the concentration of ALP. However, in subsequent sets of measurements systematic changes in the peak current were not noticed along with changes in the concentration of ALP. Even though we attempted to use identically analytes, unknown variables may have changed the chemical properties of analytes leading to two different results. The inconsistency in results could also be due to the change in conductivity of the surfaces of electrodes and electrolyte solutions. The latter fact could explain the reason for the change in the value of the potential where the peak value of the current occurs. This experimental inconsistency needs to be resolved before one can confirm the sensitivity and limit of detection found the nanocoax-based device in the measurement presented above in Figure 4.3.8.

While our devices are in array form, one can employ smaller sub arrays or even individual coaxes as a micro or nanoscale ES, after electrically addressing each coax or subarray. Such a device could then be employed, for example, to map variations in local concentration of the brain-signaling molecules *in vitro/silico*/*vivo*, which could be more facile and sensitive than the traditional manner of monitoring the concentration of the molecules using ultramicroelectrodes [37]. In addition, with further development to incorporate microfluidics for liquid exchange, the coax device could be developed into a cost-effective, portable device for rapid molecular analysis in broader applications such as environmental monitoring of chemicals and toxins, pathogen detection, and biomarker detection for the diagnosis of human disease, such as early-stage cancer.

Summary

Using the cores and shields of partially hollow nanocoaxes as working and counter electrodes, an ES with nanogap electrodes was designed. The width of the coax annulus controls the distance between electrodes in the sensor. An observed increase in electrochemical signal with decrease of electrode separation (annulus width) is due to the improvement in molecular diffusion, robust radial diffusion ensured by the cylindrical geometry, and the high site density of nanoscale electrochemical sensors in the device. These result in a ~100 × signal enhancement of the nanocoax over that of the planar ES control having millimeter separation between electrodes. This enhancement in the signal in the nanocoax-based ES was also employed to increase the sensitivity and dynamic range of detection of ALP enzyme. Such a coaxial architecture can be employed to increase sensitivity and the dynamic range of electrochemical sensors, for the detection of different molecules including biomarker associated with, e.g., early-stage of cancer.

References

[1] L. Rassaei, P. S. Singh, and S. G. Lemay, Anal. Chem. **83**, 3974 (2011).

[2] M. V. Mirkin, F.-R. F. Fan, and A. J. Bard, J. Electroanal. Chem. **328**, 47 (1992).

[3] A. N. Broers, E. G. Lean, and M. Hatzakis, Appl. Phys. Lett. **15**, 98 (1969).

[4] T. Li, L. Su, W. Hu, H. Dong, Y. Li, and L. Mao, Anal. Chem. **82**, 1521 (2010).

[5] L. Montelius, J. O. Tegenfeldt, and T. G. I. Ling, J. Vac. Sci. Technol. A **13**, 1755 (1995).

[6] H. Zhang, S.-W. Chung, and C. A. Mirkin, Nano Lett. **3**, 43 (2003).

[7] M. D. Fischbein and M. Drndić, Nano Lett. **7**, 1329 (2007).

[8] G. C. Gazzadi, E. Angeli, P. Facci, and S. Frabboni, Appl. Phys. Lett. **89**, 173112 (2006).

[9] T. Nagase, T. Kubota, and S. Mashiko, Thin Solid Films **438–439**, 374 (2003).

[10] Q. Qing, F. Chen, P. Li, W. Tang, Z. Wu, and Z. Liu, Angew. Chem. Int. Ed. **44**, 7771 (2005).

[11] D. E. Johnston, D. R. Strachan, and A. T. C. Johnson, Nano Lett. **7**, 2774 (2007).

[12] H. Park, A. K. L. Lim, A. P. Alivisatos, J. Park, and P. L. McEuen, Appl. Phys. Lett. **75**, 301 (1999).

[13] F. Chen, Q. Qing, L. Ren, Z. Wu, and Z. Liu, Appl. Phys. Lett. **86**, 123105 (2005).

[14] J.-H. Kim, H. Moon, S. Yoo, and Y.-K. Choi, Small **7**, 2210 (2011).

[15] M. Jung, W. Song, J. S. Lee, N. Kim, J. Kim, J. Park, H. Lee, and K. Hirakawa, Nanotechnology **19**, 495702 (2008).

[16] T. Li, W. Hu, and D. Zhu, Adv. Mater. **22**, 286 (2010).

[17] B. Rizal, M. M. Archibald, T. Connolly, S. Shepard, M. J. Burns, T. C. Chiles, and M. J. Naughton, Anal. Chem. **85**, 10040 (2013).

[18] A. J. Bard and L. R. Faulkner, *Electrochemical Methods: Fundamentals and Applications*, 2 edition (Wiley, New York, 2000).

[19] E. Gileadi, *Physical Electrochemistry*, 1 edition (Wiley-VCH, Weinheim, 2011).

[20] S. M. Oja, M. Wood, and B. Zhang, Anal. Chem. **85**, 473 (2013).

[21] T. Li and W. Hu, Nanoscale **3**, 166 (2011).

[22] R. J. White and H. S. White, Langmuir **24**, 2850 (2008).

[23] K. V. Singh, A. M. Whited, Y. Ragineni, T. W. Barrett, J. King, and R. Solanki, Anal. Bioanal. Chem. **397**, 1493 (2010).

[24] Phosphate buffered saline 1×; Catalog No. BP2438-20; Fisher Scientific: 300 Industry Drive, Pittsburg, PA.

[25] R. J. Foster, Chem. Soc. Rev. **23**, 289 (1994)

[26] R. C. Engstrom, M. Weber, D. J. Wunder, R. Burgess, and S. Winquist, Anal. Chem. **58**, 844 (1986).

[27] R. S. Robinson, C. W. McCurdy, and R. L. McCreery, Anal. Chem. **54**, 2356 (1982).

[28] P. Sun and M. V. Mirkin, Anal. Chem. **78**, 6526 (2006).

[29] M. A. G. Zevenbergen, B. L. Wolfrum, E. D. Goluch, P. S. Singh, and S. G. Lemay, J. Am. Chem. Soc. **131**, 11471 (2009).

[30] S. Bi, B. Liu, F.-R. F. Fan, and A. J. Bard, J. Am. Chem. Soc. **127**, 3690 (2005).

[31] D. O. Wipf and A. J. Bard, J. Electrochem. Soc. **138**, 469 (1991).

[32] F.-R. F. Fan and A. J. Bard, Science **267**, 871 (1995).

[33] F.-R. F. Fan and A. J. Bard, Science **277**, 1791 (1997).

[34] H. T. Tang, C. E. Lunte, H. B. Halsall, and W. R. Heineman, Anal. Chim. Acta **214**, 187 (1988).

[35] W. Khalid, G. Göbel, D. Hühn, J.-M. Montenegro, P. Rivera-Gil, F. Lisdat, and W. J. Parak, J. Nanobiotechnology **9**, 46 (2011).

[36] C. Ruan, Talanta **54**, 1095 (2001).

[37] R. D. Lama, K. Charlson, A. Anantharam, and P. Hashemi, Anal. Chem. **84**, 8096 (2012).

Chapter 5

Molecular Imprint Polymer on Nanocoax Structure for Biosensing

5.1 Introduction

Artificial formation of affinity recognition sites of target molecules in a synthetic matrix is a promising technique in sensor technology. In biosensing, affinity matrixes are typically prepared using specialized bio-structures such as antibodies, hormone receptors and enzymes, which conjugate perfectly and selectively with their natural targets. Though these are natural receptors, their applications in reusable affinity matrixes suffer from limited stability outside of their native environment, as well as labor intensive and expensive production methods [1–6]. Moreover, for certain target molecules, a natural recognition element may not exist or may be difficult to obtain in pure form. For these reasons, there has been a drive towards the development of a chemical alternative to biological receptors, creating tailor-made nonbiological receptors that are capable of recognizing and binding the desired biomolecules with high affinity and selectivity. Ideal synthetic hosts should be stable, easy to produce and process, and accessible to target molecules for which natural receptors do not exist.

One of the simplest ways of generating artificial receptors is through molecular imprinting of polymers (MIP) [7–9]. In this technique, a highly cross-linked polymer is synthesized around the target analyte, which acts as a template molecule. The removal of templates from the cross-linked matrix generates recognition cavities complementary to the shape, size, and functionality of the templates, as shown in Figure 5.1.1.

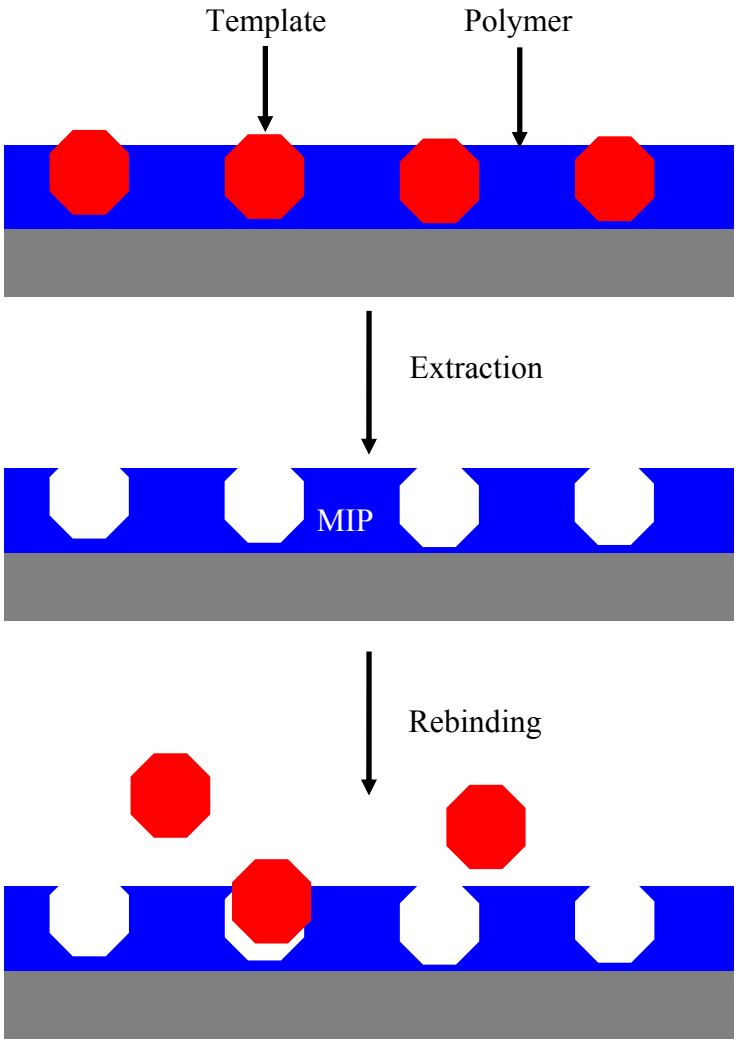

Figure 5.1.1 Schematic representation of typical steps for generation of MIP: polymer material that is formed in the presence of templates that can subsequently be removed and yet leave imprint sites in the polymer matrix that will recognize and allow for rebinding of a specific template analyte.

In essence, a molecular "memory" is imprinted on the polymer, which is now capable of selectively rebinding the template molecule [10]. MIPs are generally more stable than their biological counterparts [11,12] and indeed can provide binding sites for molecules for which no natural receptors exist. The density, distribution and effectiveness of the binding sites on the MIP depend on the monomer-template interaction, the form of the imprinted materials, and the rigidity of the polymeric matrix [10,13–16]. Over the past two decades, a number of application areas of MIPs including separation [17], sensing [18], drug delivery [19,20], and catalysis [21] for low molecular weight compounds have been established [20,22]. Several imprinted materials have been synthesized and tested. However, imprinted materials ideally suitable for proteins have yet to be fully explored due to their relatively large size, high surface complexity and conformational flexibility, and the incompatibility of proteins with organic solvents that are typically used for imprinting [23].

One of the main challenges of traditional imprinted materials is the extraction of the original templates and the subsequent inclusion of the target molecules into the cavities in the interior of bulk polymer. This is especially the case for large molecules like proteins, which reduce the capacity and kinetics of rebinding of the target molecule [24]. Creation of binding sites on or near the polymer's surface has received considerable attention, as this is thought to improve accessibility and binding kinetics of large target molecules [25–28]. Different techniques can be used to create binding sites on polymer surfaces, such as epitope-mediated imprinting [26,29–33], surface templated imprinting [25,34–36], surface-grafted imprinting [15,22,37,38], and imprinting on the surfaces of nanostructures [39–42]. Most of the previous reports on MIP-based

biosensors have employed thick polymer matrixes prepared via chemical polymerization or other less flexible covalent imprinting methods. These methods are inevitably serial, costly, and time-consuming processes. Moreover, transducing mechanisms used to detect targets are different from the mechanism used to imprint them [12,43,44]. It remains a challenge to develop a cost effective, non-covalent and aqueous media-based MIP film with thickness comparable to the size of proteins, and to do so in a simple geometry and with a sensitive transducer to characterize and quantify all steps that lead to the MIP.

Among the techniques used for protein imprinting, the electrochemical method has attracted much attention due to its use of self-limiting electrodeposition of nonconducting polymers [45] to a thickness comparable to the size of biomolecules. Furthermore, this method facilitates the deposition of a film directly at a precise area on the transducer surface in a biocompatible environment, as well as the characterization of all the steps of MIP-based sensors [23,46–50]. This method is sensitive, label-free and straight forward compared to other transducing methods [48]. These superior features of electrochemical polymerization have been successfully applied to the preparation MIP-based biosensors on 3D nanostructures [39,42,51].

MIP on 3D nanostructures has attracted considerable attention for the purpose of making sensitive electrochemical sensors because of its excellent electron transfer ability and large specific surface area relative to planar 2D devices [40,42,52–54]. This larger area for polymerization on electrode surfaces thereby increases the number of imprinting sites and thus enhances sensitivity. Therefore, 3D nanostructures, such as metal nanopillars and CNTs, have been used to increase the sensitivity of MIP-based sensors [40,42,52].

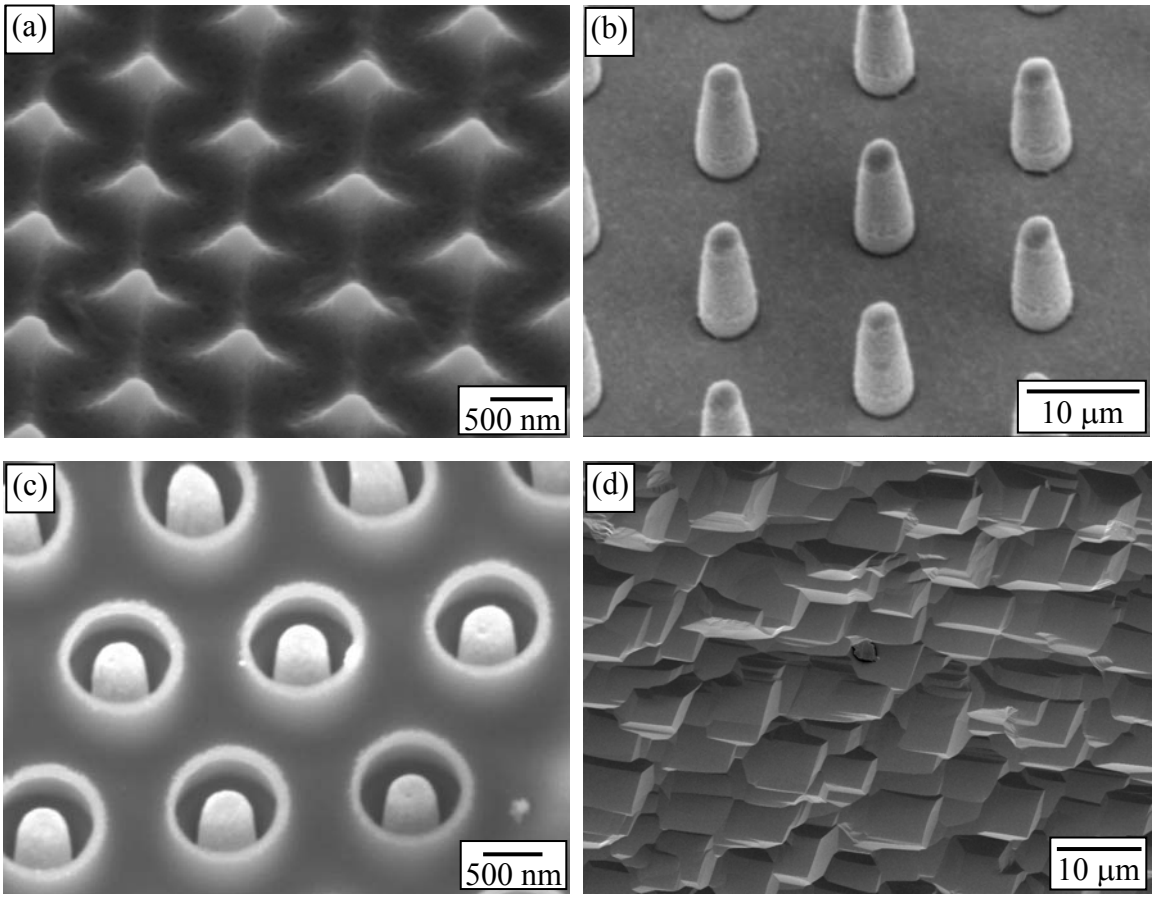

Figure 5.1.2 SEM images of the Au coated nanostructures: (a) Nandome arrays, (b) Nanopillar arrays, (c) Nanocoax arrays and (d) Unpolished side of Si wafer.

However, fabrication processes of these nanostructurs are serial, time consuming and limited in their ability to control the density of electrodes. Moreover, a long and narrow diffusion path created on a dense 3D nanostructure can impede site accessibility in the detection step. To attempt to address these issues we developed a non-conducting polymer based MIP electrochemical sensor using different shaped 3D nanostructures with known density made from SL processes such as arrays of nanodomes, nanopillars, and nanocoaxes. We also attempted other irregular structures such as rough Si surfaces and "nanodendrites". Figure 5.1.2 show SEM images of some 3D structures used to in this work.

The main objective of this work was to develop a MIP-based electrochemical sensor on a nanocoax structure, because following the results of the nanocoax ES presented in Chapter 4 this structure was anticipated to improve the sensitivity by decreasing the electrodes gap while maintaining the high surface area. However, for the systematic studies, first we started to develop MIP-based biosensors in a simple planar structure. Here, we present a reliable method to produce and quantify a non-conducting MIP film by electrochemically polymerizing an aqueous solution of phenol on a simple planar gold surface. We demonstrate that a thin film of non-covalent MIP in a planar geometry can maintain sensitivity and selectivity while overcoming previous complications in extraction and rebinding of the template analyte within the bulk polymer [23]. After the qualitative and quantitative studied of MIP films on planar geometry, we made several attempts to develop a MIP on the 3D nanostructures including nanocoax. We will discuss the issues associated with the MIP on such 3D scaffolds. In this work, to develop a MIP-based ES, streptavidin (SA) was chosen as the template protein because of its stability

and known binding sites for biotinylated proteins [55,56]. Due to its size being comparable to that of SA, bovine serum albumin (BSA) was used as a control to test the selectivity of the MIP sensor.

5.2 MIP in 2D Structure

5.2.1 Preparation of Gold Substrates

A gold planar surface was prepared by depositing a thin layer (~100 nm) of Au on a piranha-cleaned Si wafer. Electron-beam evaporation was used to deposit Au preceded by a 10 nm adhesion layer of Ti. To measure the thickness of the polyphenol (PPn), a photoresist (PR)-patterned Au surface was fabricated using photolithography as shown in Figure 5.2.1(a). For this, a thin film of the PR Shipley1813 was spin-coated on a Ti:Au-coated Si wafer at 4000 rpm for 45 s followed by soft baking at 90 °C for 1 min on a hot plate to remove any residual solvent. To make patterns of PR, the wafer was exposed to UV light of power density 24 mW/cm^2 for 3.7 s on a mask aligner (MA6, Karl Suss) holding a Cr-mask with pattern of size ~5 μm, then developed in MF319 developer for 1 min and rinsed with DI water. It is important to note that for MIP, a Au surface without any patterns was used.

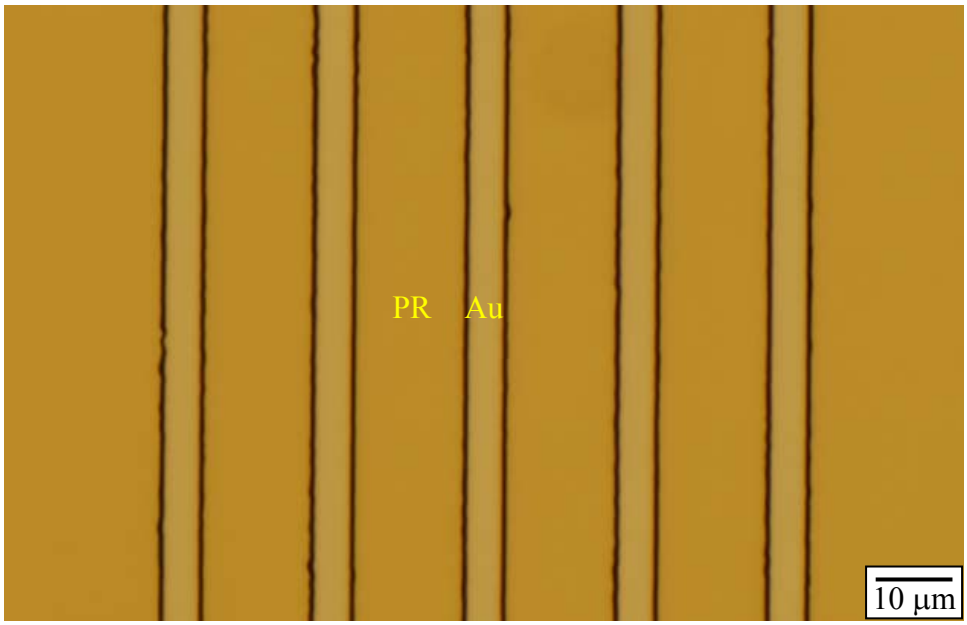

Figure 5.2.1 (a) Optical microscope image of PR- patterned Au surface.

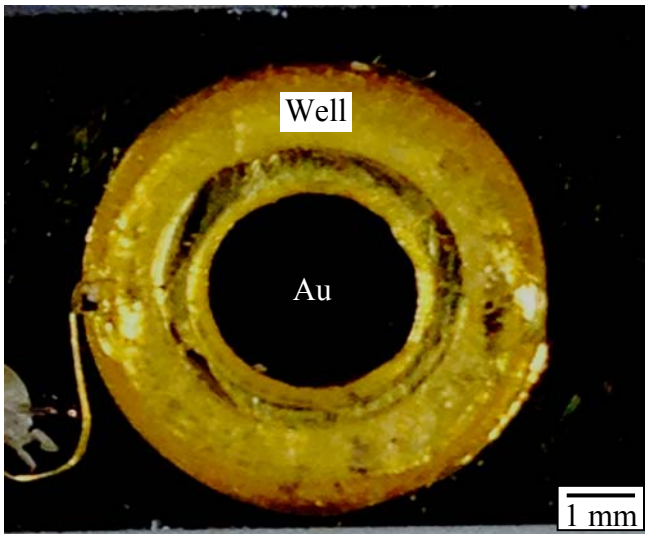

Figure 5.2.1 (b) Optical microscope image of top view of a reservoir made on the surface of gold electrode. Side view of the reservoir looks similar to Figure 4.2.1.

Both patterned and unpatterned wafers were diced into many sections of size 1 cm^2 using a dicing saw (DiscoUSA, DAD3220). After dicing, unpatterned wafers were cleaned using the RCA (Radio Corporation of America) SC-1 cleaning solution, which is a solution of DI water: hydrogen peroxide: ammonium hydroxide with ratio 3:1:1 (by volume) at 75 ^{0}C for 10 min. As shown in Figure 5.2.1(b), a reservoir with ~1 ml volume was created on each wafer using custom-made polypropylene gaskets of ~1 cm height and 3 mm inner diameter, with Epon epoxy applied to seal the gasket in order to prevent the electrolyte solution from leaking out.

5.2.2 Electrochemical Measurements

As in the previous Chapter, all electropolymerizations and measurements of the electrochemical behavior of thin films of polymers were done using a potentiostat (Gamry Instruments, Reference600) and data analysis was conducted with Echem Analyst (Gamry). A three-electrode electrochemical system was configured by using the planar Au surface as working electrode (WE), a Ag/AgCl wire as reference electrode (RE) and a Pt wire as counter electrode (CE). Cyclic voltammetry (CV) was used for the electropolymerization of phenol and differential pulse voltammetry (DPV) was used to examine Faradic current changes at the interface of the Au electrode and electrolyte consisting of 1 mM FCA in PBS. For CV, a ramping voltage was applied to the WE at a scanning rate of 50 mV s^{-1} between 0.0 and 0.9 V for five cycles and for DPV, the initial and final potentials versus the reference electrode were 0.0 and 0.5 V, respectively. The pulse size was 50 mV, the pulse time 0.05 s, the step size 2 mV, and the sampling period 0.1 s.

5.2.3 Electropolymerization of Phenol and Measurement of Thickness

We used electrochemically-polymerized phenol to develop a MIP-based electrochemical biosensor. Using CV, 2.5 mM of phenol in PBS solution was electropolymerized to coat a thin film of polyphenol (PPn) on a Au surface of a reservoir created using a polypropylene gasket as shown in Figure 5.2.2. Current vs. applied potential for two successive cycles of electropolymerization of 2.5 mM phenol on a Au electrode is as shown in Figure 5.2.2. No oxidation peak during the second CV cycle indicates that the PPn film deposited during the first cycle of CV is non-conducting, with thickness sufficient to prevent further oxidation of phenol at the Au surface. A dilute solution of phenol in PBS is conductive enough to electropolymerized at a low oxidation potential (0.4–0.8 V vs. Ag/AgCl) [38,43,57]. The main advantage of PPn is its non-conducting enough to prevent further polymerization phenol which then self-limits its thickness. We have measured the thickness of the deposited film of PPn and find that it self-limits at about 7nm. To measure the thickness, a thin film of PPn was coated on a PR-patterned Au surface. After the deposition of the PPn, the remaining PR was removed and the thickness of the resulting patterns of the PPn was measured using the AFM. Figure 5.2.3 (a) and (b) show 2D and 3D views of an AFM image of PPn layer on surface of gold of roughness ± 0.5 nm.

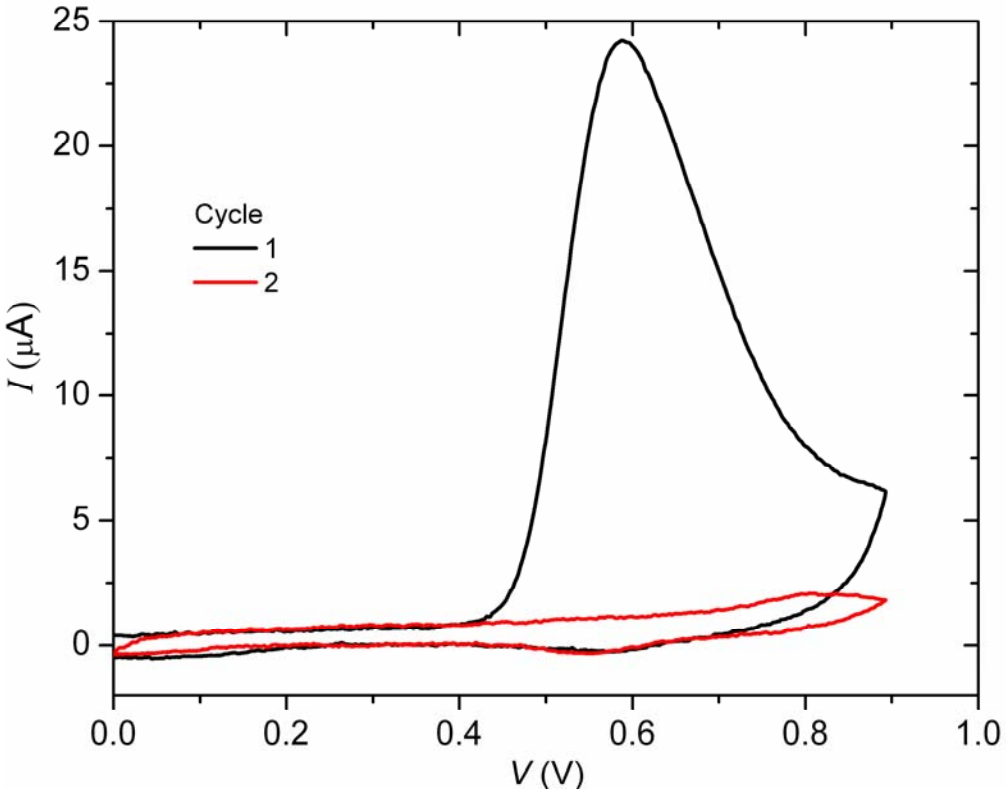

Figure 5.2.2 Current vs. applied potential for two successive cycles of electropolymerization of 2.5 mM phenol on a gold electrode of diameter 3 mm.

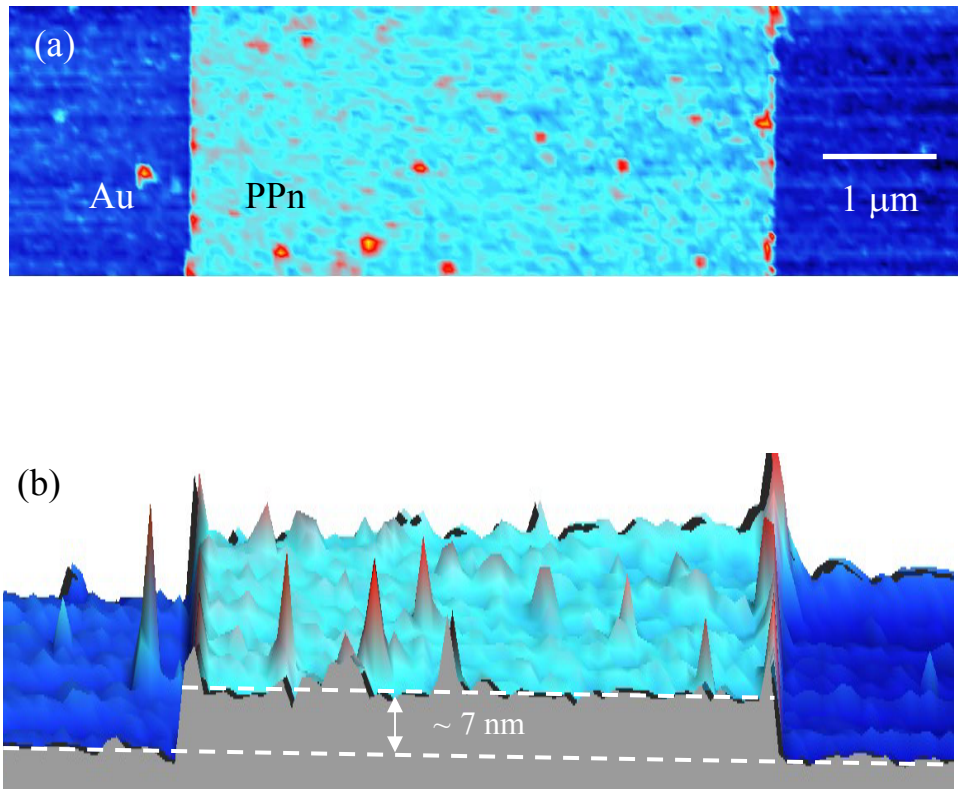

Figure 5.2.3 (a) 2D and (b) 3D views of an AFM image of PPn layer of thickness 7.25 nm on surface of gold.

The measured thickness of the PPn layer was 7.25 ± 0.65 nm, which is less than the calculated value of the thickness ~18 nm based on the amount of charge transfer during the first cycle of CV for polymerization of phenol. The total charge Q resulting from phenol oxidation (peak area) allows an estimate of the thickness of the polymer layer [44]. Assuming that each phenol molecule in the film is oxidized by one electron, one obtains

$$Q = eN \tag{1}$$

where e is the elementary charge and N is the number of oxidized phenol molecules on the electrode surface. In terms of area A and thickness t of the polymer layer and mean volume of one monomer unit in the polymer $V_{0,}$ N can be expressed as

$$N = A\ d/V_0 \tag{2}$$

The molecular weight of the monomer m can be written as

$$V_0 N_A \rho = m \tag{3}$$

where N_A is Avogadro's number, and ρ is the density of the polymer, m is the molecular weight of the monomer. Using the above equations, we get

$$t = Q\ m/F\ \rho\ A \tag{4}$$

where $F = N_A\ e$ is the Faraday constant.

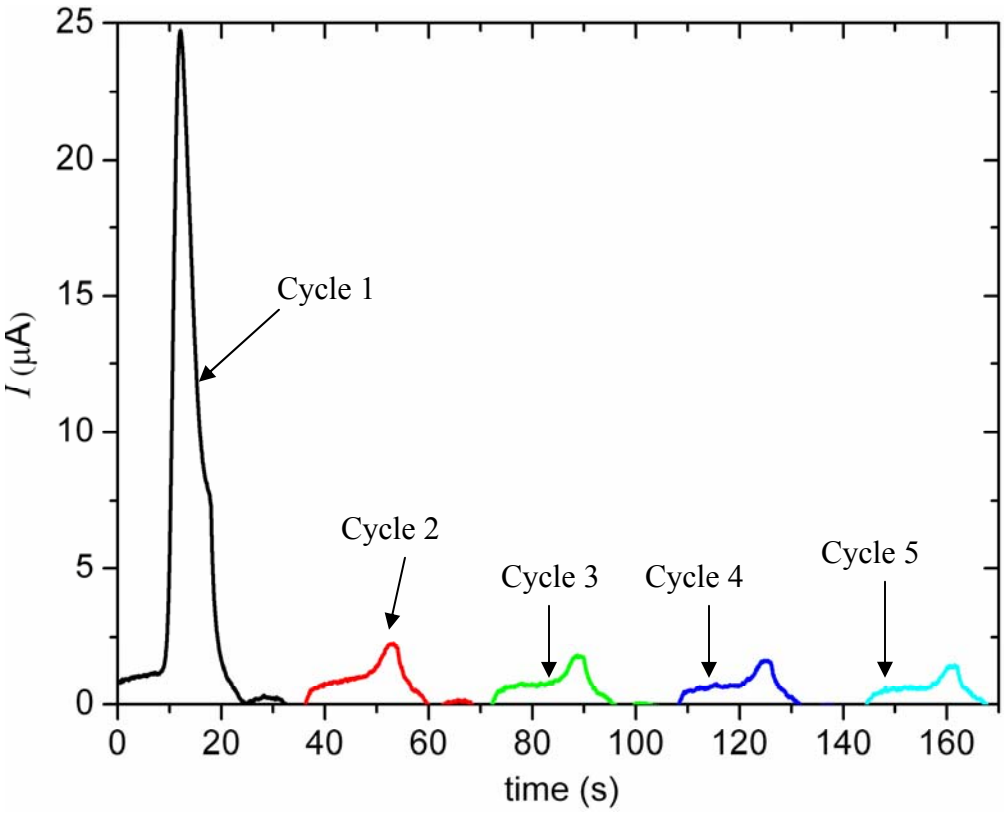

Figure 5.2.4 Current vs. time for CV for electropolymerization of phenol.

Current vs. time for the five successive cycles of cyclic voltammetry used for electropolymerization of phenol on the planar gold surface is plotted in Figure 5.2.4.

The total amounts of charge transferred at the first and fifth cycles of CV are ~ 142 and ~12 μC, respectively. Charge in the fifth cycle is taken as a background charge which needs to be subtracted in order to calculate the amount of the charge transfer due to oxidation of the phenol. The amount of charge transferred due to oxidation of phenol is thus ~130 μC. We consider the geometric area of the electrode inside the well of the reservoir to be equal to the area of the deposited PPn. Additionally, the density of the PPn is the same as that of the phenol monomer, $\rho \sim 10^3$ kgm^{-3}.

From equation (4), the thickness of the PPn deposited on the gold surface by this estimate should be

$$t = \frac{94.1 \times 130 \times 10^{-6}}{6.02 \times 10^{23} \times 1.6 \times 10^{-19} \times 10^{-3} \times 7} = 17.989 \times 10^{-9}\ m = 18.0\ nm$$

Again, the measured thickness of the PPn layer was 7.25 nm. This film thickness was confirmed by measuring 5 similar types of PPn-coated samples via AFM, as shown in Figure 5.2.5. The measured value of thickness is less than half of the above calculated value. This could be accounted for by the roughness factor of the electrode, i.e., the microscopic area of the electrodes which corresponds to the area of PPn is always higher than the geometrical area of the electrode by a factor of 2 to3 [56].

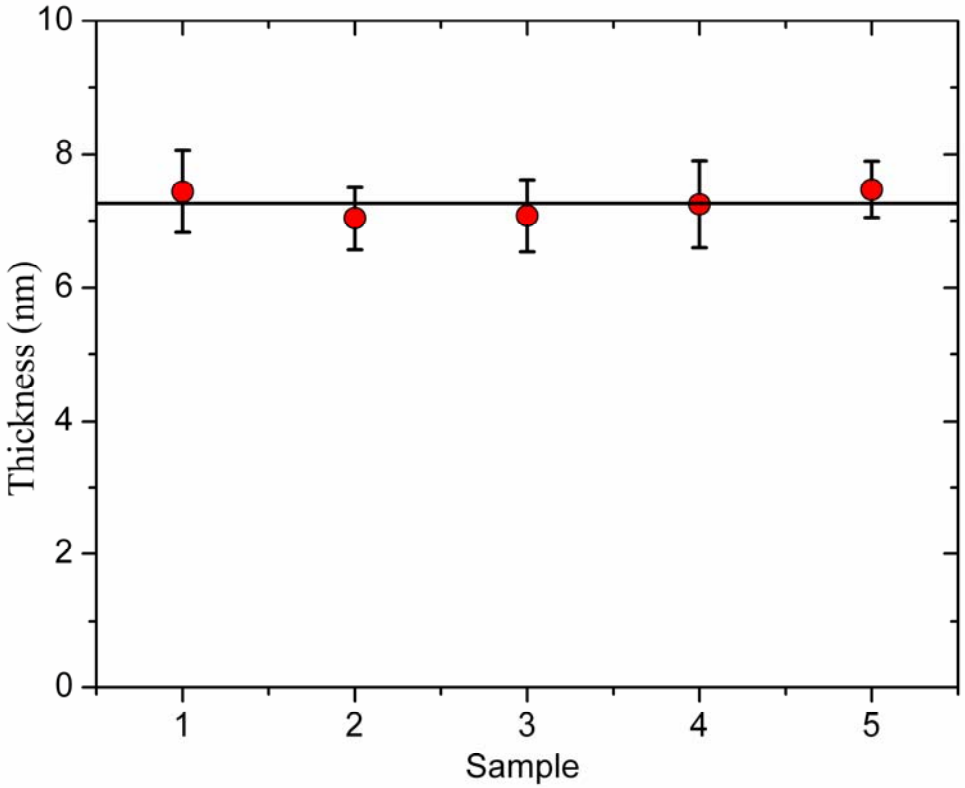

Figure 5.2.5 Thickness of PPn vs. the number of samples. Flat solid line corresponds to the mean value 7.25 nm of thickness.

More to the point, the measured value of the PPn thickness is also comparable to the size of many proteins [58], and which can play a key role in producing a non-covalent, surface-imprinted polymer without using any additional biomolecules, unlike the case of peptide-mediated surface imprinting [26].This in principle might enhance the extraction and rebinding kinetics of molecules, and hence the sensitivity of the MIP-based biosensor. To test this, we developed a PPn-based MIP with SA as a template protein, on a planar Au surface, and examined its sensitivity and selectivity.

5.2.4 Protein Imprint and Development of MIP

As shown in figure 5.1.1, the first step in making a MIP-based biosensor is the formation of the template-polymer matrix. This was done by electropolymerization of a 2.5 mM phenol solution containing SA on the Au surface of a reservoir created using a polypropylene gasket. First, a 0.3 V dc voltage, which is too low to induce polymerization of the phenol, was applied for 300 seconds to attract proteins within proximity of the surface of the WE; then, five cycles of CV resulted in the formation of polymer matrices.

To study the effect of the concentration of the template on the performance of the MIP sensor, phenol solutions with SA concentrations ranging from 0 to 500 mg L^{-1} were electropolymerized. As shown in Figure 5.2.6, the peak value of the current at the first CV cycle decreases with an increase in the concentration of the template proteins. This could be due to a decrease in the exposed area of the Au electrode as a result of assembly of larger numbers of proteins for higher concentration solutions.

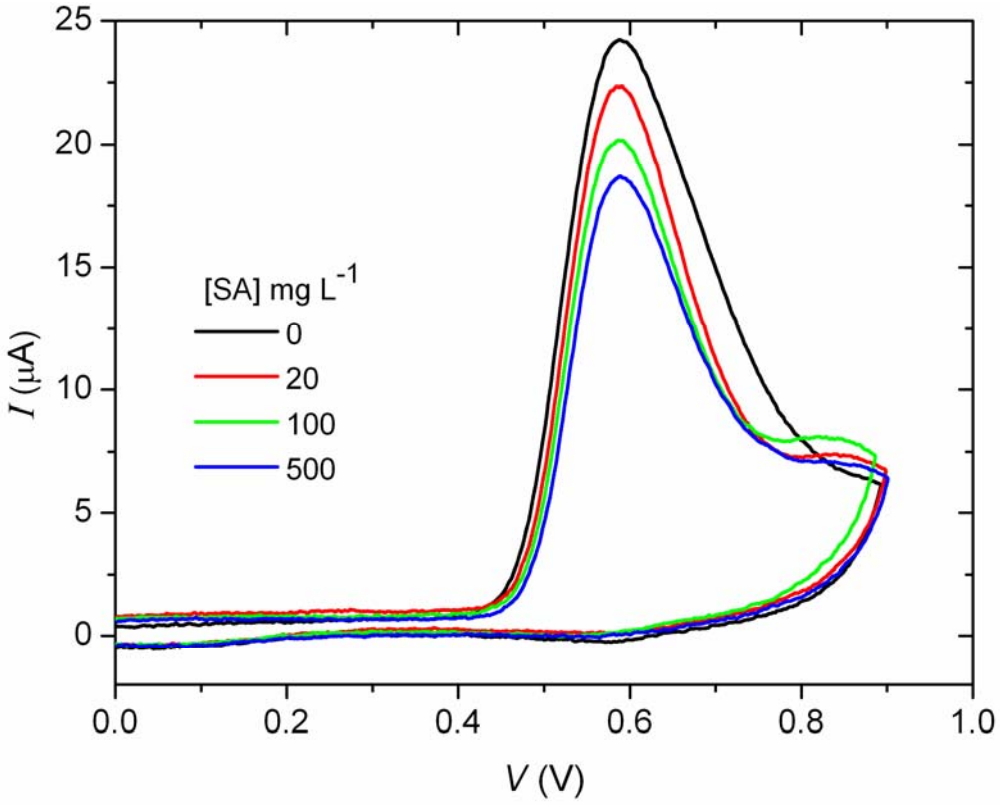

Figure 5.2.6 Current vs. applied potential at first cycle of CV for electropolymerization of 2.5 mM of phenol solution with various concentrations of template protein SA.

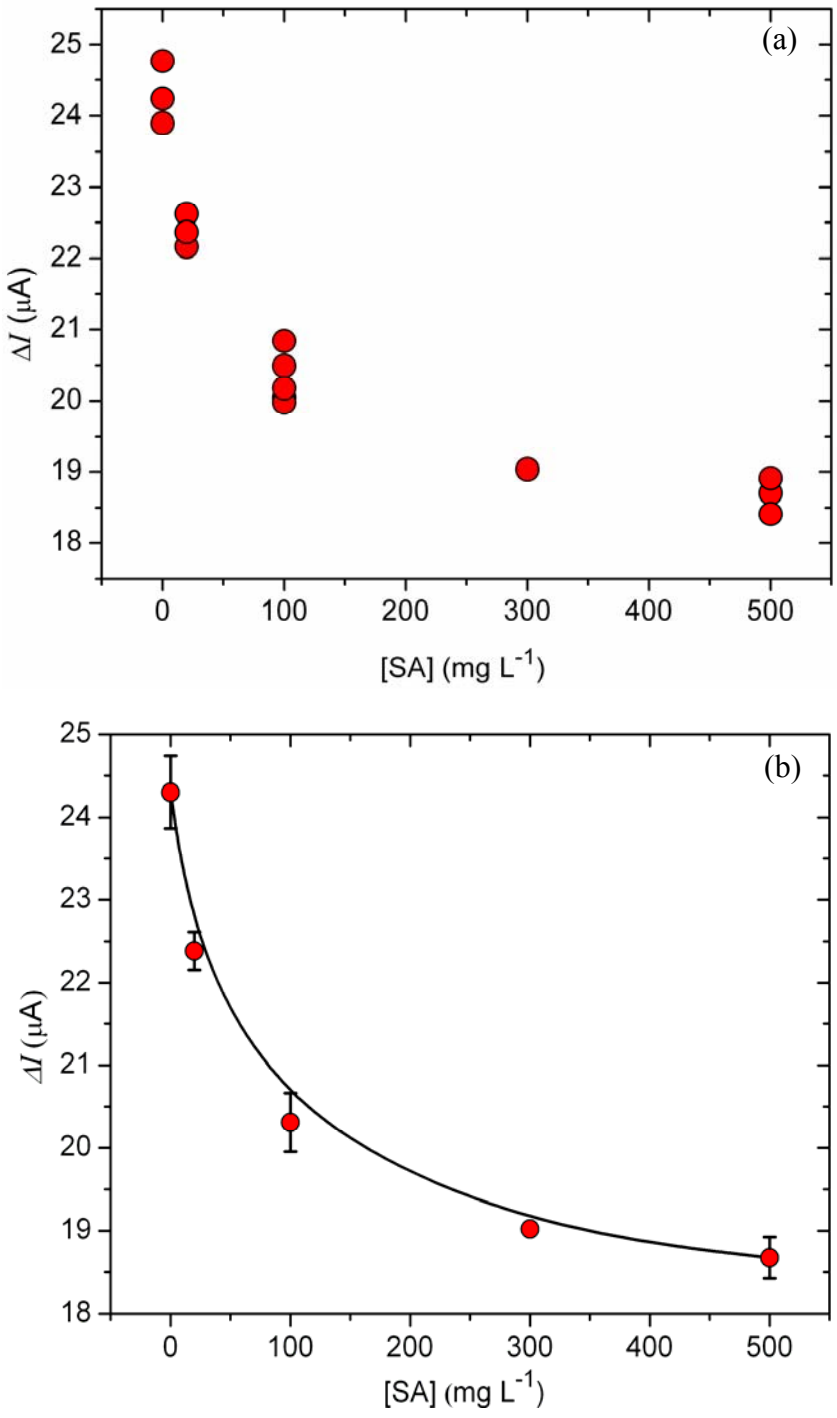

Figure 5.2.7 Difference between peak current value and current at 0.1 V at the first cycle of CV for various concentrations of template protein (a) raw data (b) the average of data in (a) with error bars indicating the standard deviations and with fitted solid line.

We show in Figure 5.2.7(a) the dependence of this peak current value with SA concentration where, for consistency of measurement for different protein concentrations, we subtracted the background current at 0.1 V from the peak current and indicated the results as ΔI. As seen in Figure 5.2.7(b), the peak value of the current decreases exponentially with concentration of SA as $\Delta I = \beta_0 + \beta \exp(-C/C_0)$ with $\beta_0 = 1.87 \times 10^{-5}$ A, $\beta = 5.04 \times 10^{-6}$ A, C_0 = 70.71 mg L^{-1} and C = concentration of SA in mg L^{-1}. Aside from 300 mg L^{-1}, all data in Figure 5.2.7(b) are averages of measurements presented in Figure 5.2.7(b) with error bars indicating the standard deviations. The amount of charge transferred during the first cycle of the CV of phenol solution with different concentrations of template proteins can be used to obtain a quantitative estimation of the density of proteins in the polymer matrixes. The volume of coated PPn depends on the amount of charge transferred in the first CV cycle [44]. Figure 5.2.8 gives an idea about the amount of charge transferred in this first cycle for polymerization of phenol with different concentration of SA. The difference in the amount of charge transferred, i.e. the peak value of the current, at the different concentrations of SA, we assume is due to the difference in coated volume of PPn. We converted the difference in the volume of PPn without SA (V_{PPn}) and with SA ($V_{PPn\text{-}SA}$) to the number of SA molecules in SA-PPn matrices as

$$N_{SA} = \frac{(V_{PPn} - V_{PPn-SA})}{V_{SA}},$$

where N_{SA} is the number of the SA molecules in a matrix and V_{SA} is volume of a single SA, which has a value of 105 nm^3 [58].

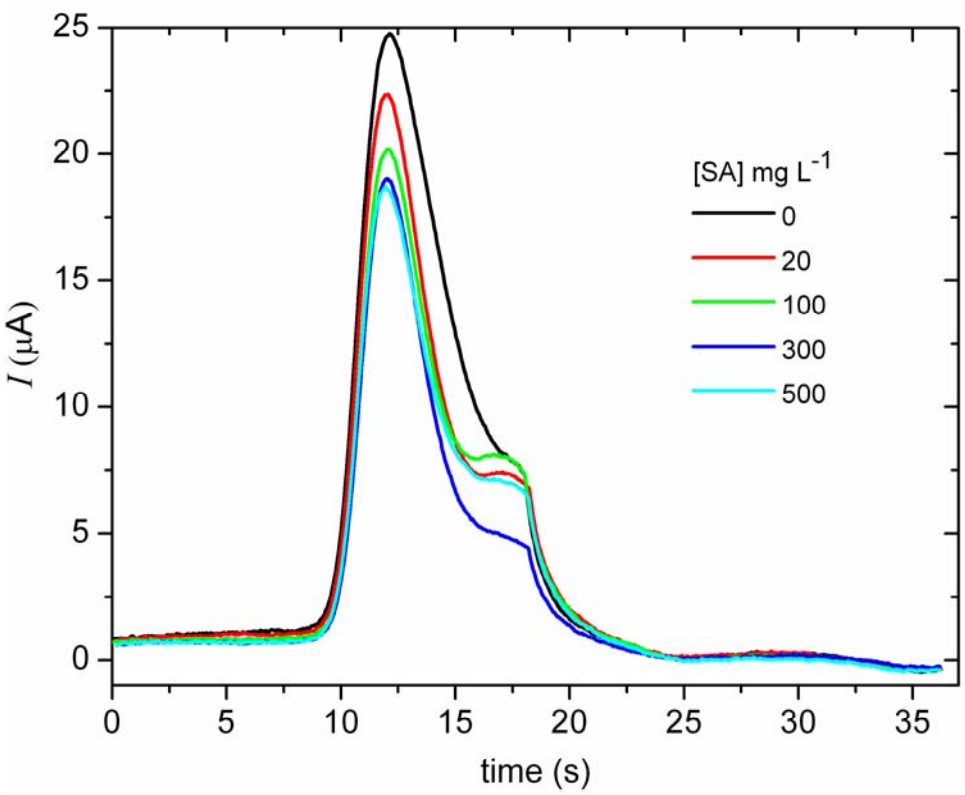

Figure 5.2.8 Current vs. time for first cycle of CV for different concentration of SA.

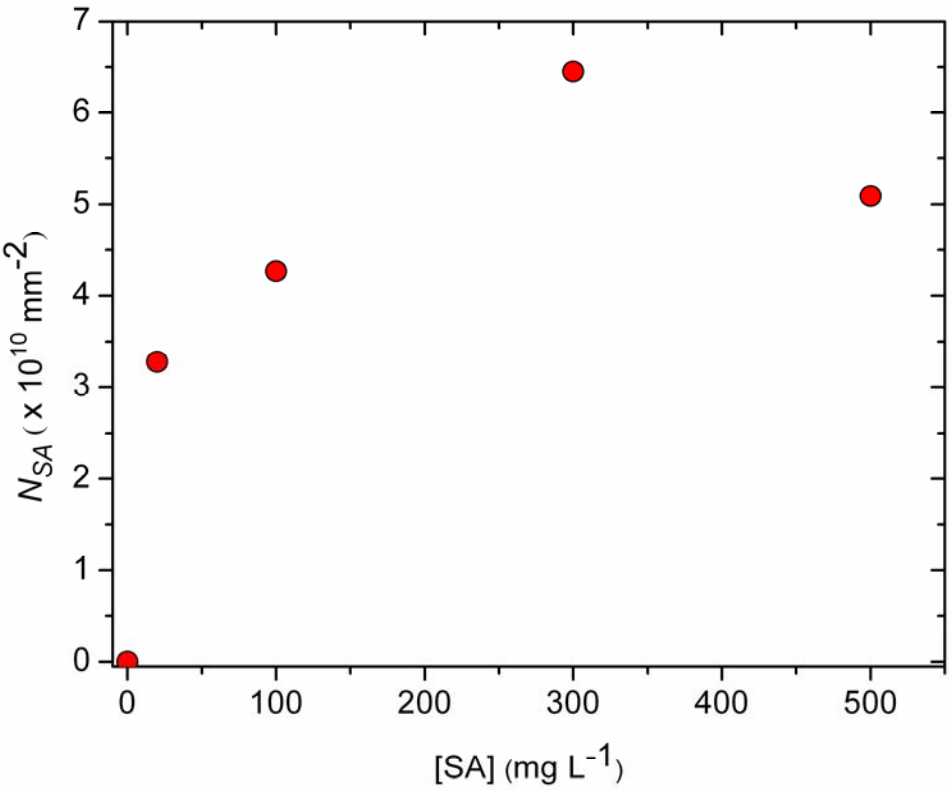

Figure 5.2.9 Number of SA per unit area of SA-PPn matrix for various concentrations of SA in 2.5 mM phenol solution.

It is important to note that, for all concentrations of SA, currents at the fifth CV cycle are about the same. Thus the background correction term is not included.

From equation (4), we can write

$$V_{PPn} = Q_{PPn}\, m/F\, \rho \text{ and } V_{SA\text{-}PPn} = Q_{Ppn\text{-}SA}\, m/F\, \rho$$

$$N_{SA} = \frac{m(Q_{PPn} - Q_{PPn-SA})}{V_{SA} F\, \rho}$$

$$N_{SA} = 94.1 \times 10^{14} \times (Q_{PPn} - Q_{PPn-SA}) C^{-1}$$

The calculated values of N_{SA} per unit area of SA-PPn matrices, made using different concentrations of SA in phenol solution, are presented in Figure 5.2.9. The higher value number of the number of SA molecules in SA-PPn matrix for 300 mgL^{-1} of SA could be due to defects on the Au surface. The quality of SA-PPn and PPn coatings were tested by using DPV with 1 mM FCA solution. Figure 5.2.10 shows the DPV signals from a bare, a PPn film and a SA-PPn matrix, corresponding to 100 mg L^{-1} of SA, coated Au surfaces each of diameter ~3 mm. Nearly equal magnitudes and a similar nature of the DPV signals were observed from the PPn and SA-PPn films. No oxidation peaks on the DPV signals from PPn and SA-PPn films indicate that no leakage of the electrolyte solution occurred in either PPn or SA-PPn films. However, as expected, the magnitude of the DPV signal reduced significantly due to the coatings.

As indicated in Figure 5.1.1, the next step in the development of a MIP is the extraction of the template proteins from the template-polymer matrix. For this, SA-PPn matrixes were incubated overnight in different kinds of buffer solutions, including a combination

of different concentrations of sodium dodecyl sulphate (SDS) (0.1 to 10 %), proteinase k (Pk) (10 to 500 mg L^{-1}), and acetic acid (AcOH) (0.1 to 1%) solutions, DI water at 27 and 70 ^{0}C, 10% of tween 20, 2 to 8 M of guanidine-HCl, and 1 to 3 M of urea solutions. The effects of all these chemicals on the PPn coating and the SA-PPn matrix are summarized in Table 5.2.11. Among these combinations, the solution containing 1% SDS, 0.1% acetic acid, and 100 mg L^{-1} of Pk in PBS most efficiently extracted the SA without causing major damage to the surface of the NIP control. After the extraction of proteins, both NIP and MIP films were evaluated using DPV. The DVP response of NIP and MIP films is as shown in Figure 5.2.12.

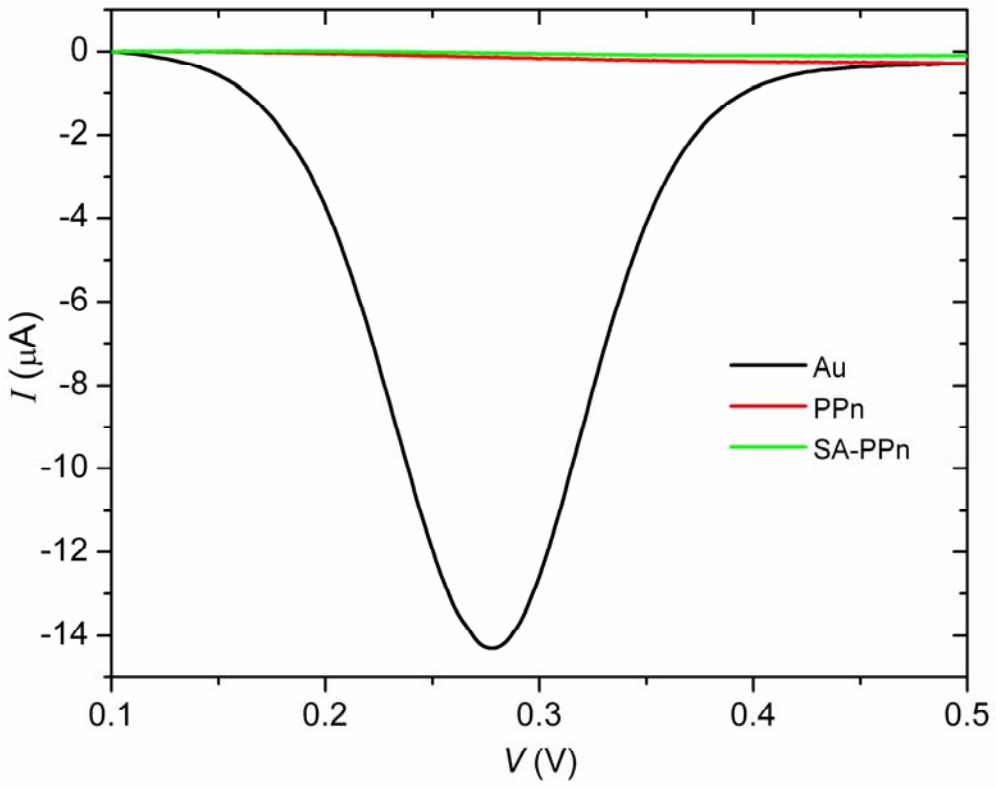

Figure 5.2.10 DPV signals from a bare, a PPn and a SA-PPn matrix, corresponding to 100 mg L^{-1} of SA, coated Au electrodes each of diameter ~3 mm.

Chemicals at 25 ^{0}C	Damage on PPn	Extraction of SA from SA-PPn matrix	Efficient extraction for MIP
DI water	No	No	No
10 % SDS &1% AcOH in PBS	Yes	Yes	No
5% SDS &0.5% AcOH in PBS	Yes	Yes	No
1%SDS & 0.1% AcOH in PBS	No	No	No
1%SDS, 0.1% AcOH &100 mg L^{-1} Pk in PBS	No	Yes	Yes
0.1% SDS, 0.01% AcOH &100 mg L^{-1} Pk in PBS	No	No	No
Tween 20	No	No	No
2M Guanidine - HCl	No	No	No
4M Guanidine - HCl	No	No	No
8M Guanidine - HCl	No	No	No
1 M Urea	No	No	No
3 M Urea	No	No	No
DI water up to 90 ^{0}C	No	No	No

Table 5.2.11 Chemical solutions tested for the extraction of proteins, toward the development of MIP.

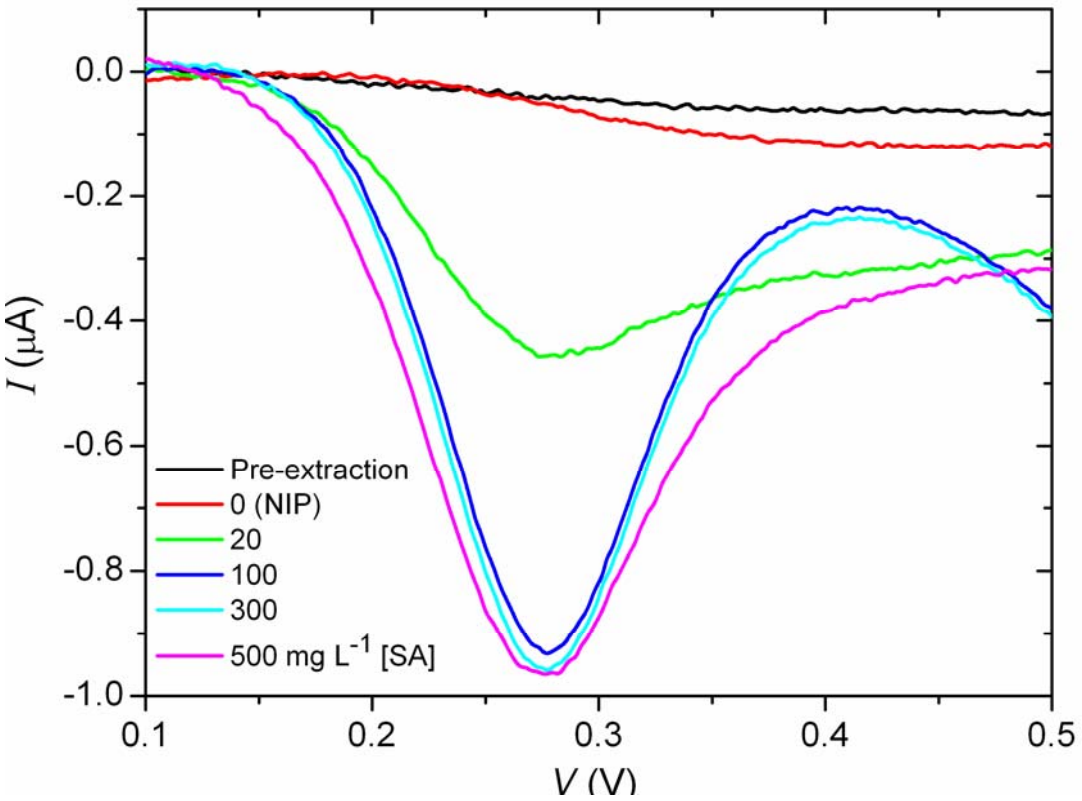

Figure 5.2.12 DPV signal at the different stages of development of MIP. The signals before extraction is from SA-PPn matrix composed of 100 mg L^{-1} SA signals after extraction of SA from the matrixes with various concentrations of template SA are shown. Data for the NIP control is also presented.

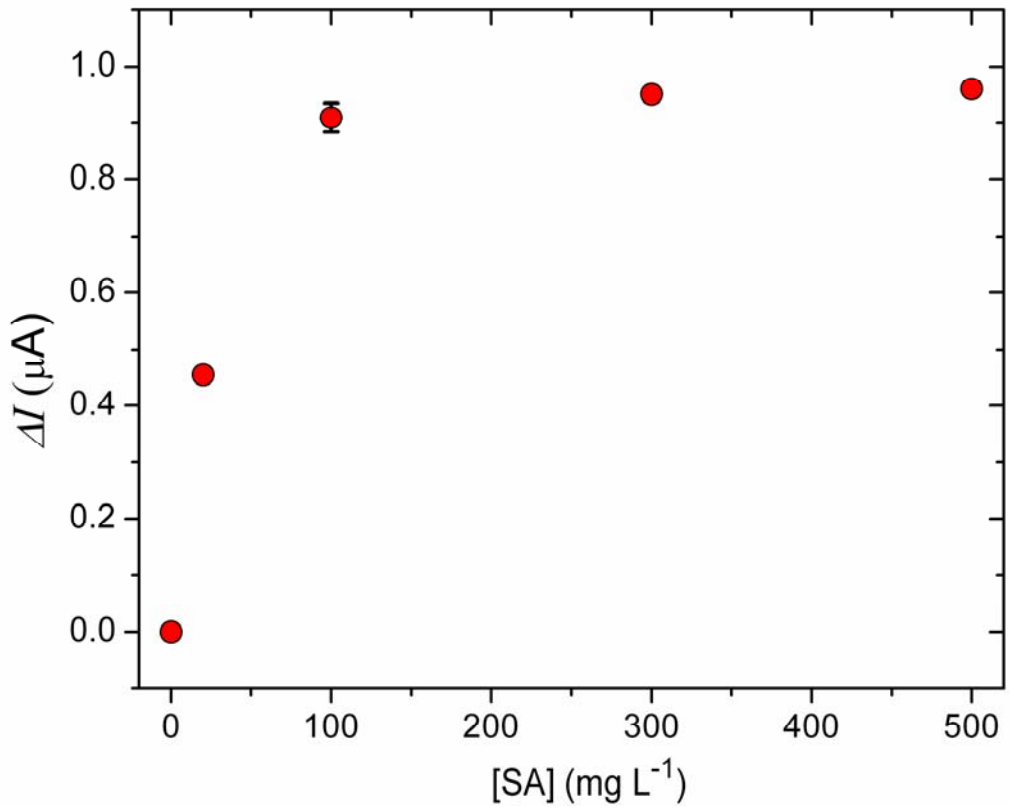

Figure 5.2.13 Difference between peak current value and current at 0.1 V for the various concentrations of template protein SA.

The dependence of this peak current value with SA concentration is as shown in Figure 5.2.13. As anticipated, the value of the peak current increases with the concentration of the protein and becomes saturated near 100 mg L^{-1} of SA, as shown Figure 5.2.13. This is in agreement with the nature of the peak value of the current measured in first cycle of CV for various concentration of SA as shown Figure 5.2.7. In order to demonstrate the breadth of sensitivity and selectivity of the MIP-based planar sensor, a MIP film corresponding to the 100 mg L^{-1} (~1.7 μM) concentration of the template SA was used.

5.2.5 Rebinding of Proteins

For the rebinding of the template protein SA, MIP samples incubated for 30 min at room temperature with solutions of SA of various concentrations ranging from 0.5 to 10,000 pg L^{-1}, this corresponds to ~10 aM to 100 fM, which was calculated using the following relation.

$$[SA]_m = \frac{[SA]}{[M]}$$

Where $[SA]_m$ and $[SA]$ are molar and mass concentrations of a protein and $[M]$ is molecular weight of protein in terms of kDa (1 kDa =1.66 x 10^{-24} kg) and for SA [M]= 60 kDa [58]. After incubation with each concentration of SA, unbound SA on MIP were washed out and the rebinding of SA on its imprinted sites on the MIP was observed using DPV with the FCA solution. Figure 5.2.14 (a)-(c) show the DPV signal after rebinding of SA on 3 independent MIP films using solutions containing various concentrations of SA. As expected, the magnitude of the peak current decreases with an increase in concentration of rebinding protein.

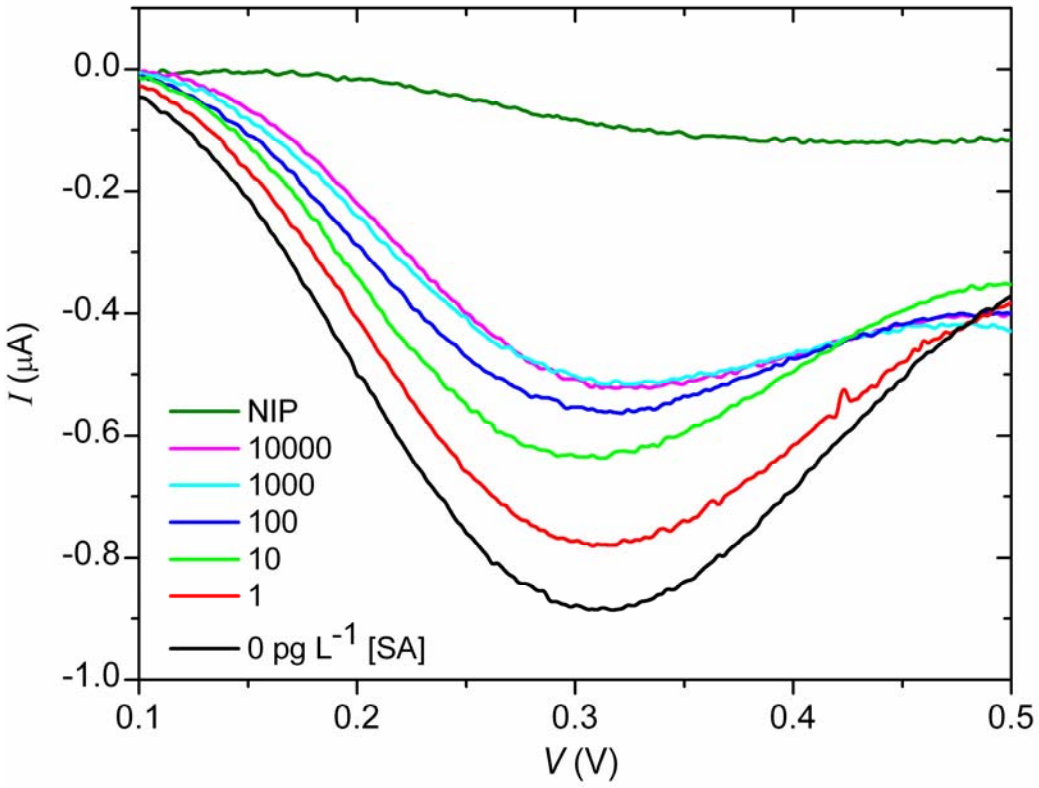

Figure 5.2.14 (a) DPV current response due to rebinding of various concentrations of template analyte SA on the MIP developed from 100 mg L^{-1} template protein SA.

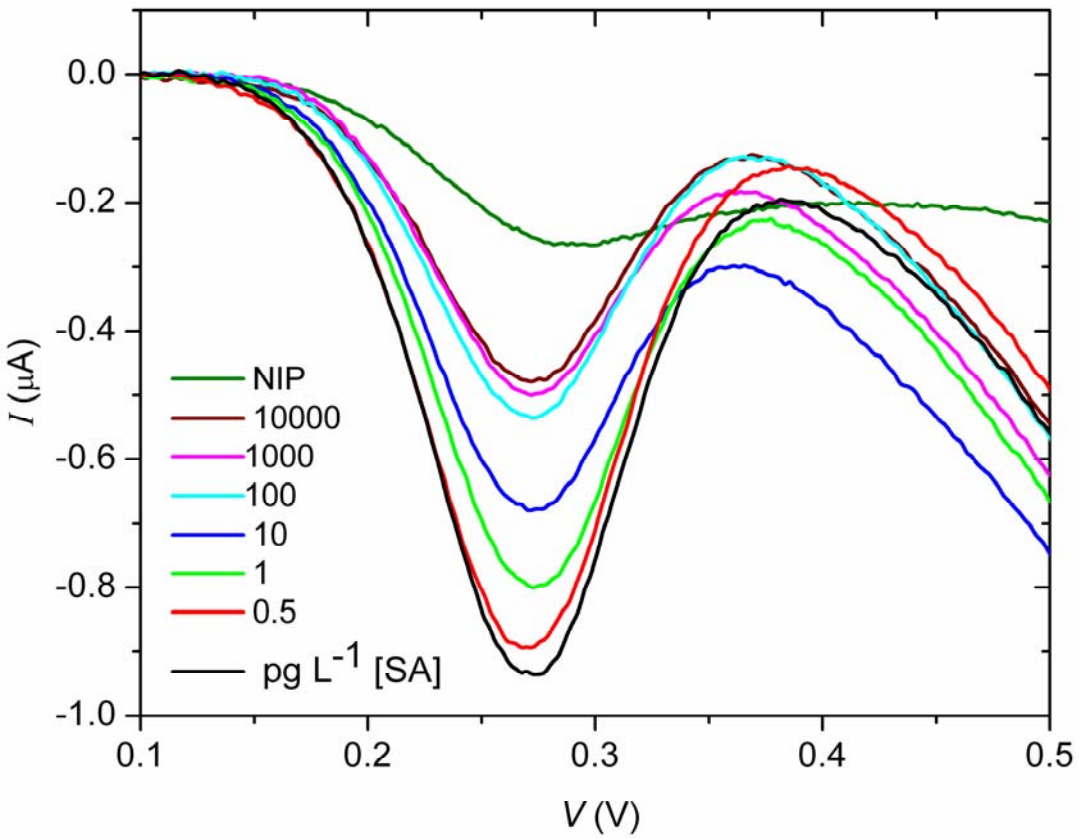

Figure 5.2.14 (b) DPV current response due to rebinding of various concentrations of template analyte SA on the MIP developed from 100 mg L^{-1} template protein SA.

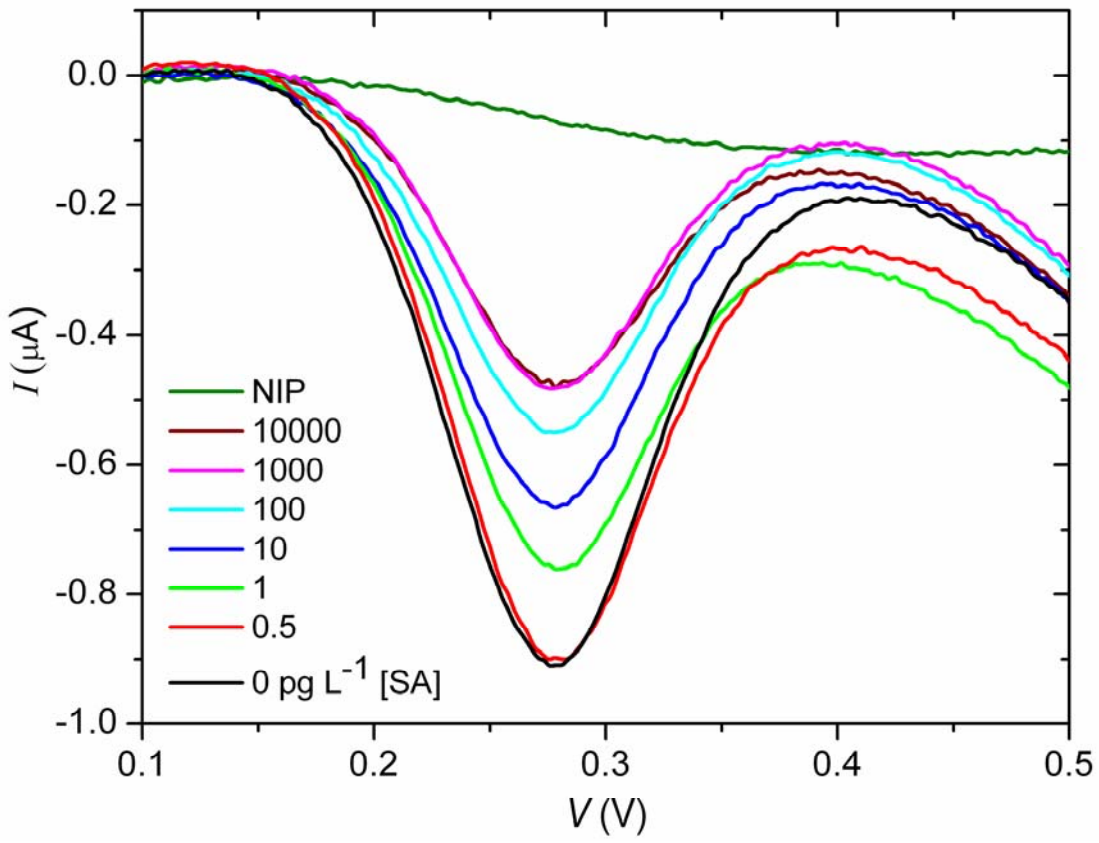

Figure 5.2.14 (c) DPV current response due to rebinding of various concentrations of template analyte SA on the MIP developed from 100 mg L^{-1} template protein SA.

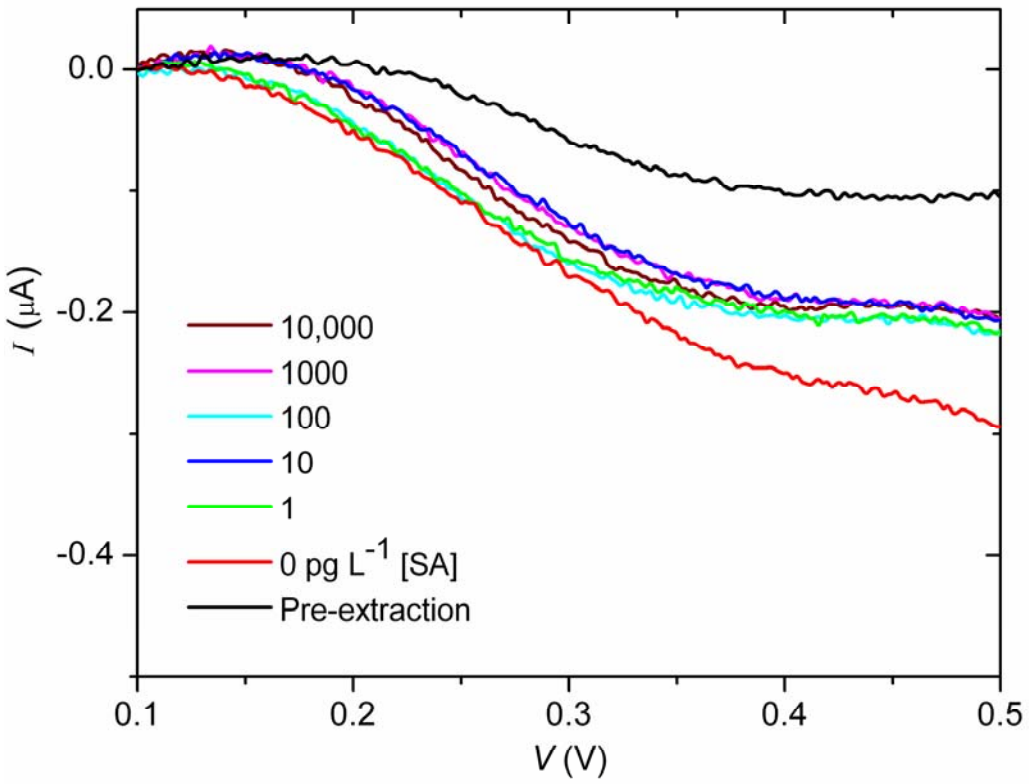

Figure 5.2.15 DPV current response from NIP before and after treatment with the same buffer solution used for the extraction of SA from SA-PPn matrix. The responses due to rebinding of various concentrations of template analyte SA on the NIP are also shown.

This is because of the increase in resistance of the MIP film caused by blocking of the MIP sites as a result of target protein rebinding. However, there is saturation in current for rebinding at concentrations above 1000 pg L^{-1} of SA. Moreover, the magnitude of the saturated peak is always higher than for the NIP control (*i.e.* it does not return to the low current NIP level). This could be due to a certain fraction of target molecules removed in the extraction process having been done so from imprints that leave behind voids too small to facilitate molecule rebinding.

In this work NIP was taken as a control. NIP was subjected through all the steps of the MIP sensors. As shown in Figure 5.3.15, there are no oxidation peaks in the DPV signal after the treatment with the same buffer solution used for the extraction of protein from SA-PPn matrix, which indicates that there was no damage in the NIP film from the process for extraction of proteins. Also there is no change in the signal due to rebinding of the SA on NIP films. This indicates that PPn itself has no electrochemical interaction with SA. The data for changes in the peak value of current after subtracting the peak value before rebinding any concentrations of proteins on MIP, defined here as $\delta(\Delta I)$, versus protein concentration for three independent measurements are plotted in Figure 5.2.17. The average value of $\delta(\Delta I)$ for 0.5 pg L^{-1} and the standard deviation for the 0 pg L^{-1} data are ~0.02 μA. Considering a 3σ criterion, we claim a limit of detection (LOD) of MIP on this 2D planar substrate for SA as 1 pg L^{-1} (~20 aM). This is essentially the same LOD (Figures 5.2.18 (a) and (b)) as reported for a significantly more complex nano-engineered 3D MIP sensor [39].

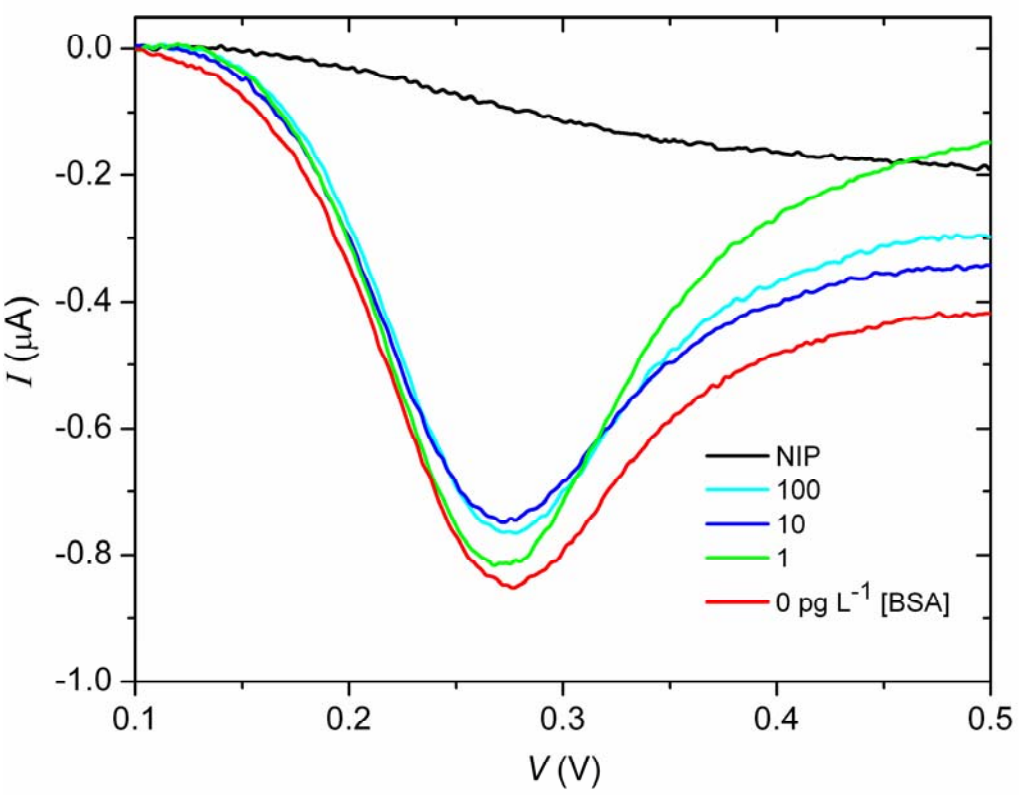

Figure 5.2.16 DPV current response due to rebinding of various concentrations of BSA on the MIP developed from 100 mg L^{-1} template protein SA.

To assess the selectivity of our MIP film, the interference of various concentrations of the non-template protein bovine serum albumin (BSA) on the DPV signal of the film was tested. As shown in Figure 5.3.16, the lack of a significant change in the DPV response of the MIP film before and after incubation with various concentrations of BSA confirms the strong selectivity ($\delta(\Delta I)_{SA}/\delta(\Delta I)_{BSA}$ ~300%) selectivity of MIP on planar device. Moreover, the selectivity of MIP film on 2D planar is comparable to previously reported selectivity of MIP film on 3D nanostructure [39](Figure5 .3.18(b)) with respect to the control protein BSA. Certain aspects of 2D MIP sensors, such as the use of the different kinds of template biomolecules for potential clinical use and electrode arrangement to reduce distance between WE and CE to increase the sensitivity have not yet been examined. However, the straightforward fabrication process of the self-limited 2D MIP film could be employed to make cost effective, integratable and portable devices for the rapid detection of biomolecules associated with human diseases, such as cancer biomarkers.

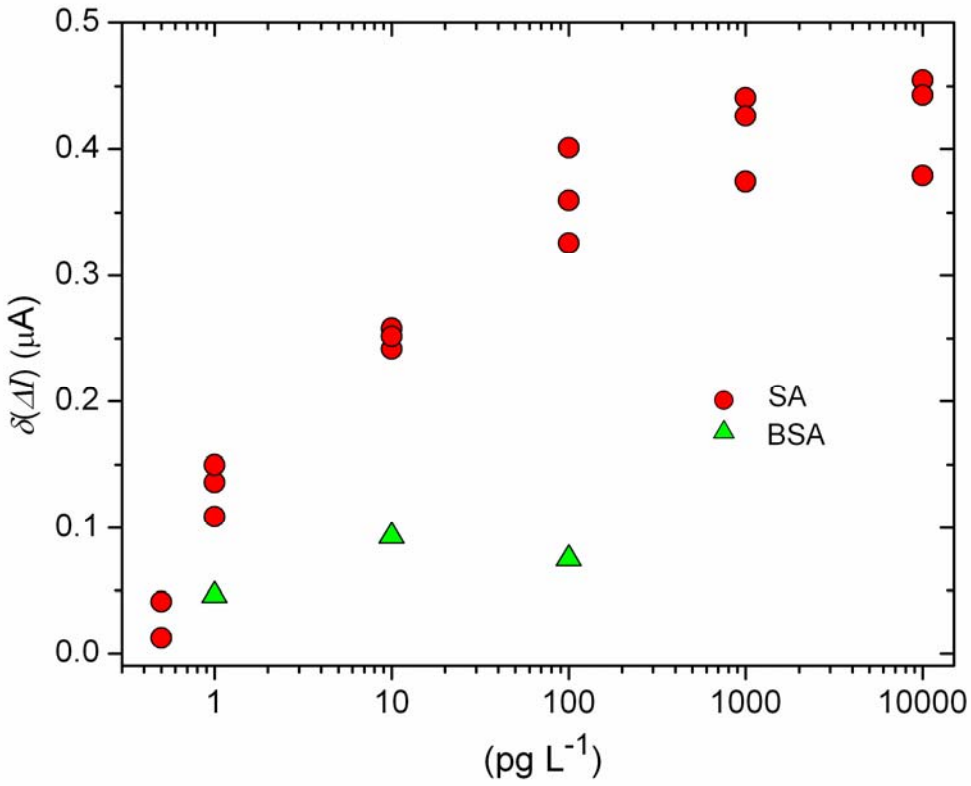

Figure 5.2.17 Difference between the peak current without and with rebinding of various concentrations of SA. The response of the MIP from SA template for control protein BSA is also presented.

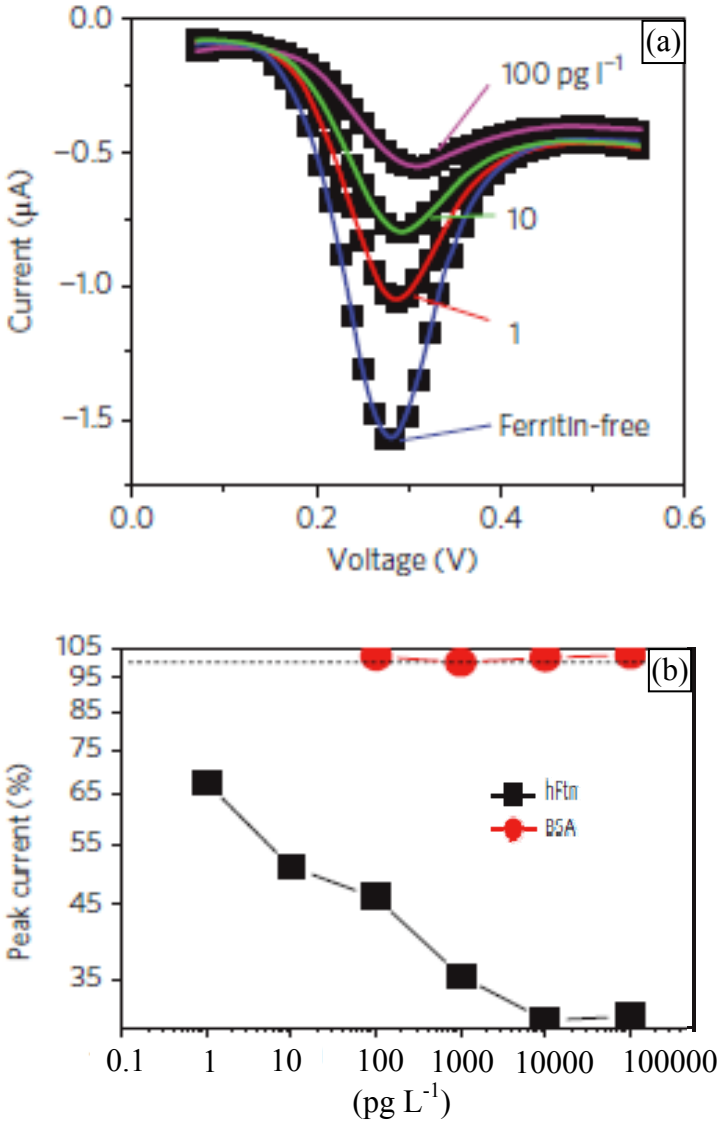

Figure 5.2.18 (a) DPV current response due to rebinding of various concentrations of template analyte human ferritin (hFtn) on the MIP developed on tips of arrays of CNT using from 100 mg L^{-1} template protein hFtn in 1.5 mM phenol solution. (b) Protein concentration-dependent peak current response vs. concentration of template and control proteins, hFtn and BSA, respectively. Each value of peak current (%) in y-axis, is percentage of ratio of peak DPV current from the MIP film after binding of the correspondence concentration of protein in x-axis to the peak DPV current from MIP after extraction of template protein (i.e. without binding of protein).

5.3 MIP on 3D Nanostructures

Using the same recipes made for development of MIP-based sensor in 2D planar structure as reference starting point, we attempted to develop MIP on the different 3D nanostructures mentioned in Section 5.1. Among these structures, nanocoax was of a particular interest. Recalling the results in Chapter 4 and the previous section 5.2, we saw an ~100 × signal enhancement of the nanocoax over that of the planar ES, and a LOD of MIP on this 2D planar substrate for SA as 1 pg L^{-1} (~20 aM), respectively, we might anticipate a selective and sensitive MIP- based biosensor for the detection of proteins with LOD in order of zepto-molar concentrations. Such a ultrasensitive MIP-based sensor might provide detection of early stage diseases such as alzheimer's, ovarian cancer, or coronary artery disease, whose treatments experience better success rates if the diseases can be detected in their early stage of development [59].

Here to make a smooth transition from a simple 2D planar to a compound 3D nanocoax structures, we tried to develop MIP in other intermediated 3D nanostructures such as arrays of nandomes and nanopillars. As in the case of the planar electrode, 2.5 mM of phenol in PBS solution and SA with concentration of 100 mg L^{-1} in 2.5 mM of phenol in PBS solution were used to deposit a PPn film and a SA-PPn matrix on the surface of the 3D electrodes. In the case of nanocoax arrays, only the inner electrode surfaces were coated. This was achieved by using the inner electrodes of the arrays as a WE for polymerization of phenol. We used all solutions mentioned in Table 5.2.11 for the extraction of proteins to develop a MIP on the surface of various 3D architectures. However, none of the buffer solutions were able to efficiently extract proteins without damaging the NIP.

Figure 5.3.2 shows the DPV responses from a PPn film and a SA-PPn matrix before and after incubation in a solution containing 1% SDS, 0.1% acetic acid, and 100 mg L^{-1} of Pk in PBS. Nearly equal magnitudes and a similar nature of the DPV signals, with oxidation peaks due to leakage of the electrolyte solution from the SA-PPn and PPn films, were observed. This observed peak on the NIP control indicates that the buffer solution used to extract protein damaged the PPn coating. This is the solution that efficiently extracts the SA without major damage to the surface of the NIP control in planar electrodes. This damage of the non-planar PPn coating could be due to a non-uniform thickness of PPn caused by the roughness of the surface of the 3D structure as shown in Figure 5.3.1 (a). Rough morphology of the electrode can change electric properties of a device including the field breakdown mechanism at the metal/insulator interface [60]. This damage in the PPn layer could be due to over-oxidation of phenol [45] because of enhanced electric field (Figure 5.3.1 (c)) near the sharp edges of the rough surface of the electrodes.

Different attempts were made to minimize the damage to the polymer or the effect of the damage on the sensor performance. Such attempts included coating a monolayer of thiol on the surface of the electrodes before polymerization of phenol or after the incubation of PPn in the buffer solution. We also investigated the use of a different monomer (amino-phenol, and scopoletin) solution to develop MIP. Polymerization of conducting polymer (anthranilic acid) followed by the polymerization of phenol. However, a successful technique to solve this problem has not yet been identified.

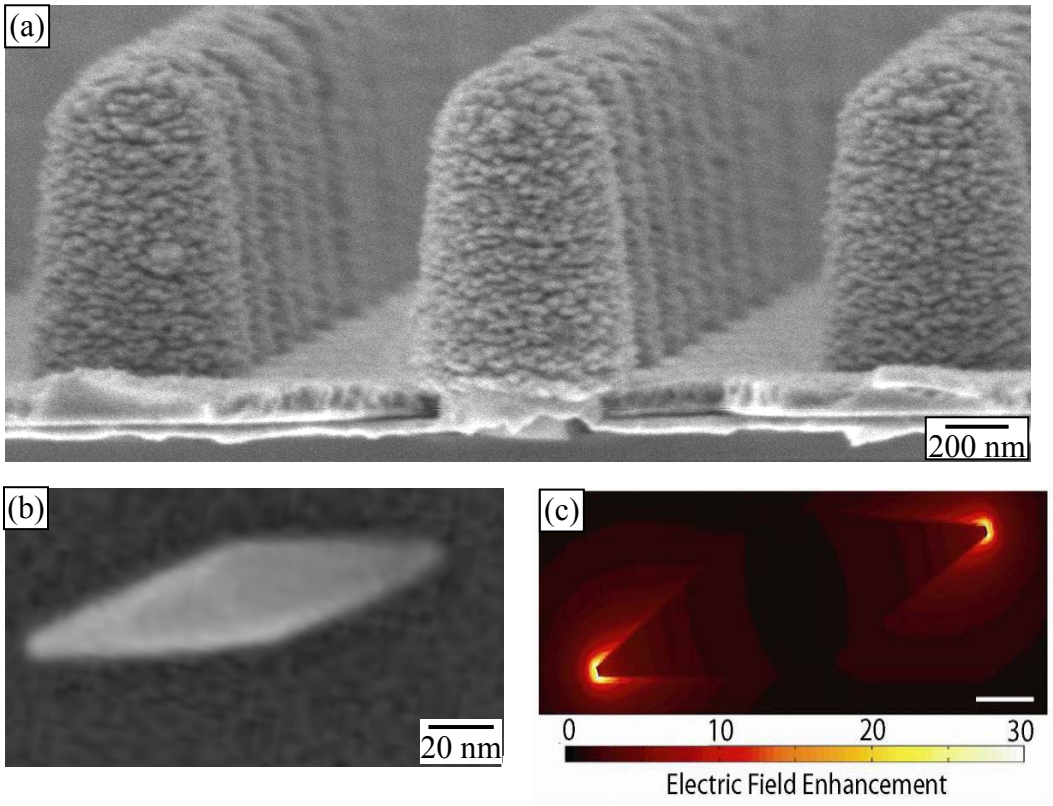

Figure 5.3.1 SEM images of (a) arrays of metallized SU-8 nanopillar showing roughness on their surfaces and (b) a Au bipyramid nanostructure with sharp tips. (c) Calculated profile of the electric field showing the enhancement of the electric field at tips of Au bipyramid. From [61].

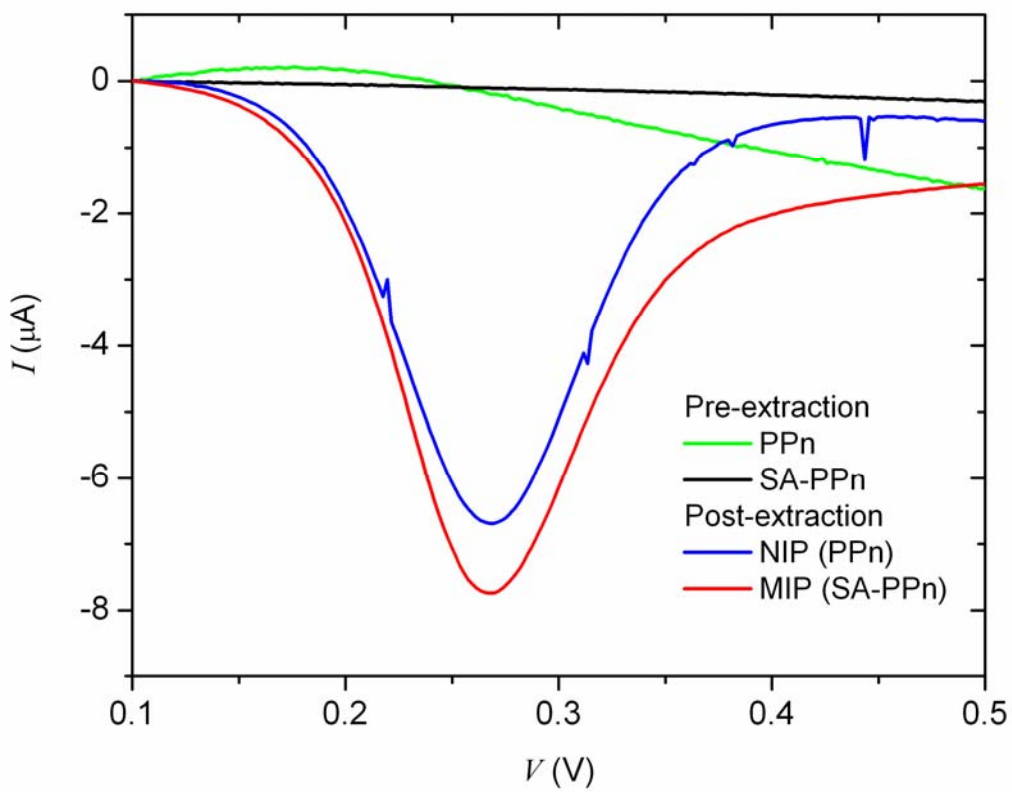

Figure 5.3.2 DVP signals before and after extraction of SA from SA-PPn matrix coated using 100 mg L^{-1} SA on the surface of inner electrode of arrays of nanocoax. Data for the PPn control is also presented.

In spite of the damage to the PPn coating on 3D surfaces, we tried to observe the effect of the rebinding of protein in both MIP and NIP film on the electrode surface of nanocoax. For the rebinding of the template protein SA, MIP and NIP were incubated for 30 min at room temperature with solutions of SA of various concentrations ranging from 1 to 100 pg L^{-1}. After incubation with each concentration of SA, unbound SA on MIP and NIP were washed out and the rebinding of SA on its imprinted sites on the MIP and voids in NIP were observed using DPV with the FCA solution. However, in both cases the magnitude of the peak current decreased with an increase in concentration of the rebinding protein. We interpret this being a result of rebinding of proteins blocking the MIP sites and NIP voids therefore increasing the resistance of the films. The data for $\delta(\Delta I)$ versus protein concentration for both NIP and MIP are plotted in Figure 5.3.4. In contrast to an imprinted film, the NIP film contains no imprinted sites. Hence, specific binding through the imprinting effect should not be observed. Furthermore, the observed DPV signal from undamaged NIP in planar electrode indicates PPn itself has no electrochemical interaction with SA. The observed DPV signals from rebinding of SA on NIP could be due to the creation of voids of size comparable to the size of the proteins, or cracks in the NIP. However, the underlying mechanism behind the observed DPV signals due to rebinding of SA on NIP has yet to be identified.

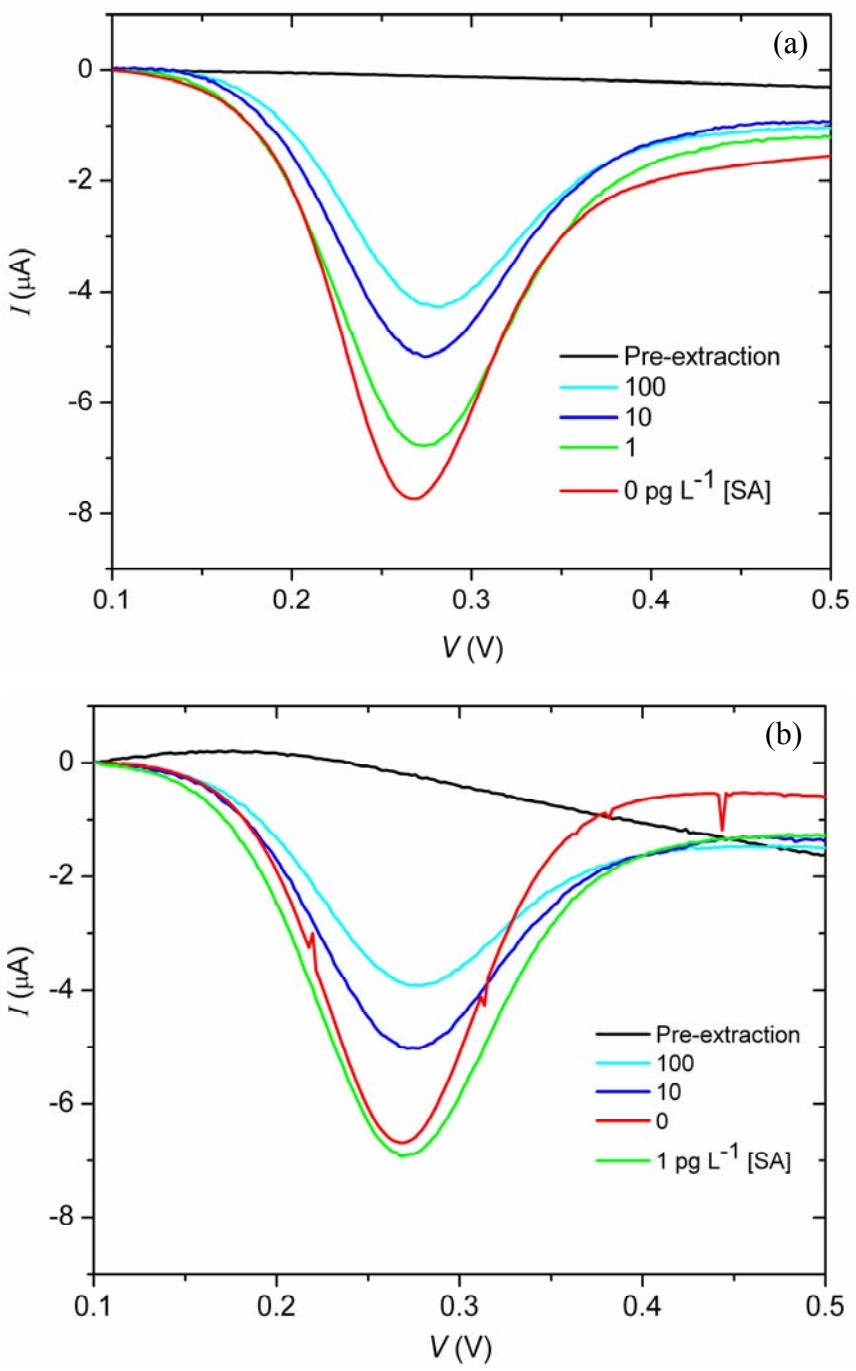

Figure 5.3.3 DPV current response due to rebinding of various concentrations of template analyte SA on the (a) MIP developed from 100 mg L^{-1} template protein SA and (b) NIP on the nanocoax structure.

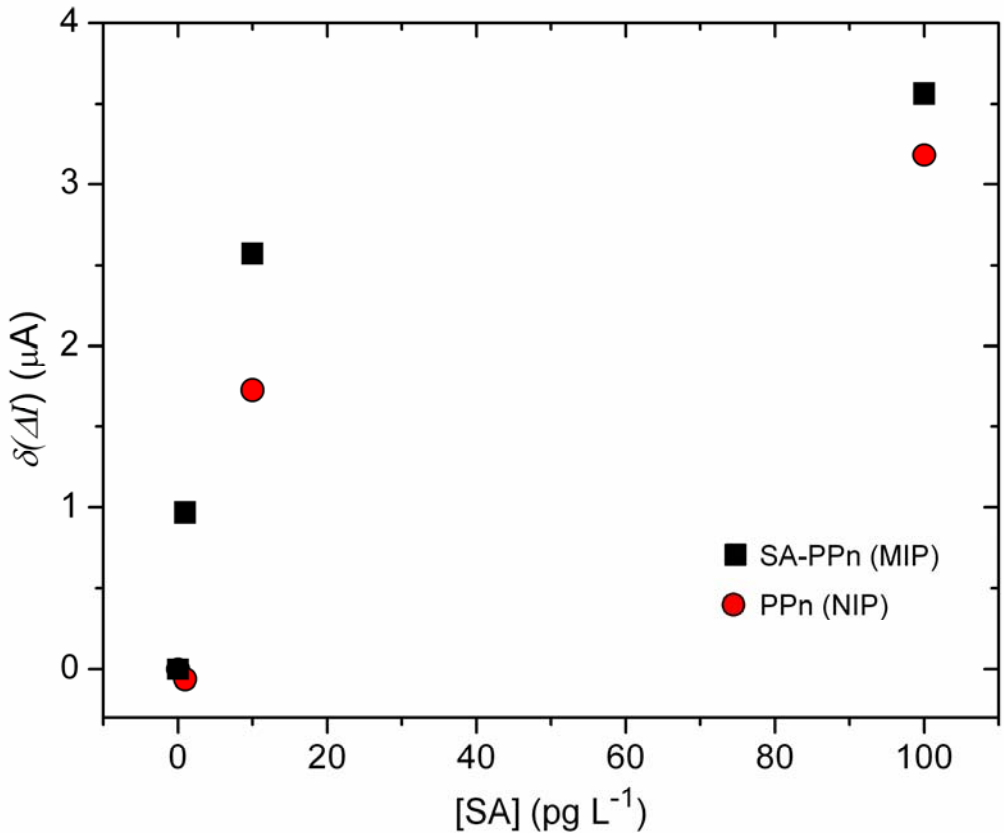

Figure 5.3.4 Difference between the peak current without and with rebinding of various concentrations of SA MIP and NIP on the nanocoax structure.

Summary

Using 2D Au electrodes, we have developed a thin, non-conducting, aqueous solution-compatible, MIP-based electrochemical biosensor for the selective recognition of proteins. While matching sensitivity and selectivity comparable to previously reported MIP sensors, [40,52,53,62] our strategy offers some attractive features, especially a simple and fast electrode fabrication process that is amenable to direct integration of MIP sensors on e.g., a cost-effective portable device. We have used different 3D nanostructures as the scaffolds including arrays of nanocoaxes to develop a MIP-based electrochemical sensor. Though different solutions were tried to extract SA from the different polymers matrixes without damage to the corresponding NIP controls, a successful combination of polymer and buffer solution for efficient extraction of proteins to develop a MIP based electrochemical sensor in 3D nanostructure has yet to be identified. Considering the potential of the sensor demonstrated thus far for detection of SA, we can anticipate 2D MIP-based portable and label-free sensors for additional uses, such as environmental monitoring and diagnosing human diseases via detection of biomarkers.

References

[1] S. Subrahmanyam, S. A. Piletsky, and A. P. F. Turner, Anal. Chem. **74**, 3942 (2002).

[2] Y. Yuan, R. Yuan, Y. Chai, Y. Zhuo, L. Bai, and Y. Liao, Anal. Biochem. **405**, 121 (2010).

[3] C. A. K. Borrebaeck and C. Wingren, J. Proteomics **72**, 928 (2009).

[4] I. E. Tothill, Semin. Cell Dev. Biol. **20**, 55 (2009).

[5] R. Elnathan, M. Kwiat, A. Pevzner, Y. Engel, L. Burstein, A. Khatchtourints, A. Lichtenstein, R. Kantaev, and F. Patolsky, Nano Lett. **12**, 5245 (2012).

[6] H.-K. Chang, F. N. Ishikawa, R. Zhang, R. Datar, R. J. Cote, M. E. Thompson, and C. Zhou, ACS Nano **5**, 9883 (2011).

[7] C. Alexander, H. S. Andersson, L. I. Andersson, R. J. Ansell, N. Kirsch, I. A. Nicholls, J. O'Mahony, and M. J. Whitcombe, J. Mol. Recognit. JMR **19**, 106 (2006).

[8] K. Mosbach, Trends Biochem. Sci. **19**, 9 (1994).

[9] K. Mosbach and O. Ramström, Nat. Biotechnol. **14**, 163 (1996).

[10] F. P. R. M. I. P. T. N. G. A. Mip. are stable, easy to prepare, and inexpensive, there are still challenges to overcome in their fabrication and use. PDF [715 KB] PDF w/ Links[433 KB] Abstract Citing Articles Add to ACS ChemWorx Karsten Haupt, Anal. Chem. **75**, 376 A (2003).

[11] M. J. Whitcombe, I. Chianella, L. Larcombe, S. A. Piletsky, J. Noble, R. Porter, and A. Horgan, Chem. Soc. Rev. **40**, 1547 (2011).

[12] R. Schirhagl, Anal. Chem. **86**, 250 (2014).

[13] A. Katz and M. E. Davis, Nature **403**, 286 (2000).

[14] S. C. Zimmerman, M. S. Wendland, N. A. Rakow, I. Zharov, and K. S. Suslick, Nature **418**, 399 (2002).

[15] R. H. Schmidt, K. Mosbach, and K. Haupt, Adv. Mater. **16**, 719 (2004).

[16] B. Sellergren, Anal. Chem. **66**, 1578 (1994).

[17] W. J. Cheong, S. H. Yang, and F. Ali, J. Sep. Sci. **36**, 609 (2013).

[18] A. A. Volkert and A. J. Haes, The Analyst **139**, 21 (2014).

[19] A. G. Mayes and M. J. Whitcombe, Adv. Drug Deliv. Rev. **57**, 1742 (2005).

[20] S. R, Pharm. Anal. Acta (2014).

[21] M. Resmini, Anal. Bioanal. Chem. **402**, 3021 (2012).

[22] H. Chen, J. Kong, D. Yuan, and G. Fu, Biosens. Bioelectron. **53**, 5 (2014).

[23] P. S. Sharma, A. Pietrzyk-Le, F. D'Souza, and W. Kutner, Anal. Bioanal. Chem. **402**, 3177 (2012).

[24] G. Vasapollo, R. D. Sole, L. Mergola, M. R. Lazzoi, A. Scardino, S. Scorrano, and G. Mele, Int. J. Mol. Sci. **12**, 5908 (2011).

[25] H. Shi, W. B. Tsai, M. D. Garrison, S. Ferrari, and B. D. Ratner, Nature **398**, 593 (1999).

[26] D. Dechtrirat, N. Gajovic-Eichelmann, F. F. Bier, and F. W. Scheller, Adv. Funct. Mater. n/a (2013).

[27] A. V. Linares, F. Vandevelde, J. Pantigny, A. Falcimaigne-Cordin, and K. Haupt, Adv. Funct. Mater. **19**, 1299 (2009).

[28] A. Nematollahzadeh, W. Sun, C. S. A. Aureliano, D. Lütkemeyer, J. Stute, M. J. Abdekhodaie, A. Shojaei, and B. Sellergren, Angew. Chem. Int. Ed. **50**, 495 (2011).

[29] A. Rachkov and N. Minoura, J. Chromatogr. A **889**, 111 (2000).

[30] D.-F. Tai, M.-H. Jhang, G.-Y. Chen, S.-C. Wang, K.-H. Lu, Y.-D. Lee, and H.-T. Liu, Anal. Chem. **82**, 2290 (2010).

[31] D.-F. Tai, C.-Y. Lin, T.-Z. Wu, and L.-K. Chen, Anal. Chem. **77**, 5140 (2005).

[32] G. Ertürk, L. Uzun, M. A. Tümer, R. Say, and A. Denizli, Biosens. Bioelectron. **28**, 97 (2011).

[33] C.-H. Lu, Y. Zhang, S.-F. Tang, Z.-B. Fang, H.-H. Yang, X. Chen, and G.-N. Chen, Biosens. Bioelectron. **31**, 439 (2012).

[34] O. Hayden, K.-J. Mann, S. Krassnig, and F. L. Dickert, Angew. Chem. Int. Ed. **45**, 2626 (2006).

[35] N. Pérez, M. J. Whitcombe, and E. N. Vulfson, Macromolecules **34**, 830 (2001).

[36] K. Fukazawa, Q. Li, S. Seeger, and K. Ishihara, Biosens. Bioelectron. **40**, 96 (2013).

[37] A. Bossi, S. A. Piletsky, E. V. Piletska, P. G. Righetti, and A. P. F. Turner, Anal. Chem. **73**, 5281 (2001).

[38] M.-M. Titirici and B. Sellergren, Chem. Mater. **18**, 1773 (2006).

[39] D. Cai, L. Ren, H. Zhao, C. Xu, L. Zhang, Y. Yu, H. Wang, Y. Lan, M. F. Roberts, J. H. Chuang, M. J. Naughton, Z. Ren, and T. C. Chiles, Nat. Nanotechnol. **5**, 597 (2010).

[40] Y. Yang, G. Fang, G. Liu, M. Pan, X. Wang, L. Kong, X. He, and S. Wang, Biosens. Bioelectron. **47**, 475 (2013).

[41] T. Chen, M. Shao, H. Xu, S. Zhuo, S. Liu, and S.-T. Lee, J. Mater. Chem. **22**, 3990 (2012).

[42] S. Viswanathan, C. Rani, S. Ribeiro, and C. Delerue-Matos, Biosens. Bioelectron. **33**, 179 (2012).

[43] C. Xie, B. Liu, Z. Wang, D. Gao, G. Guan, and Z. Zhang, Anal. Chem. **80**, 437 (2008).

[44] T. L. Panasyuk, V. M. Mirsky, S. A. Piletsky, and O. S. Wolfbeis, Anal. Chem. **71**, 4609 (1999).

[45] D. Hu, C. Peng, and G. Z. Chen, ACS Nano **4**, 4274 (2010).

[46] D. Cai, L. Ren, H. Zhao, C. Xu, L. Zhang, Y. Yu, H. Wang, Y. Lan, M. F. Roberts, J. H. Chuang, M. J. Naughton, Z. Ren, and T. C. Chiles, Nat. Nanotechnol. **5**, 597 (2010).

[47] S. Viswanathan, C. Rani, S. Ribeiro, and C. Delerue-Matos, Biosens. Bioelectron. **33**, 179 (2012).

[48] C. Malitesta, E. Mazzotta, R. A. Picca, A. Poma, I. Chianella, and S. A. Piletsky, Anal. Bioanal. Chem. **402**, 1827 (2012).

[49] N. J. Ronkainen, H. B. Halsall, and W. R. Heineman, Chem. Soc. Rev. **39**, 1747 (2010).

[50] S. Li, *Molecularly Imprinted Sensors Overview and Applications* (Elsevier, Amsterdam; Boston, 2012).

[51] G. Yang, F. Zhao, and B. Zeng, Biosens. Bioelectron. **53**, 447 (2014).

[52] P. Wang, W. Dai, L. Ge, M. Yan, S. Ge, and J. Yu, The Analyst **138**, 939 (2013).

[53] V. Suryanarayanan, C.-T. Wu, and K.-C. Ho, Electroanalysis **22**, 1795 (2010).

[54] C. Malitesta, E. Mazzotta, R. A. Picca, A. Poma, I. Chianella, and S. A. Piletsky, Anal. Bioanal. Chem. **402**, 1827 (2012).

[55] K. H. Lim, H. Huang, A. Pralle, and S. Park, Biotechnol. Bioeng. **110**, 57 (2013).

[56] A. J. Bard and L. R. Faulkner, *Electrochemical Methods: Fundamentals and Applications*, 2 edition (Wiley, New York, 2000).

[57] T. Chen, M. Shao, H. Xu, S. Zhuo, S. Liu, and S.-T. Lee, J. Mater. Chem. **22**, 3990 (2012).

[58] C. S. Neish, I. L. Martin, R. M. Henderson, and J. M. Edwardson, Br. J. Pharmacol. **135**, 1943 (2002).

[59] G. Shipp, Biotechnol. Healthc. **3**, 35 (2006).

[60] Y.-P. Zhao, G.-C. Wang, T.-M. Lu, G. Palasantzas, and J. T. M. De Hosson, Phys. Rev. B **60**, 9157 (1999).

[61] K. M. Mayer, F. Hao, S. Lee, P. Nordlander, and J. H. Hafner, Nanotechnology **21**, 255503 (2010).

[62] C. Malitesta, E. Mazzotta, R. A. Picca, A. Poma, I. Chianella, and S. A. Piletsky, Anal. Bioanal. Chem. **402**, 1827 (2012).

Concluding Remarks

In summary, this dissertation explored a simple, inexpensive, and unconventional lithographic method of forming nanodevices for sensing applications. In addition to the lithographic method, a molecular imprinting method was used to develop a synthetic matrix on planar geometry for the sensitive detection of biomolecules.

Chapter 1 introduced the nanocoax structure and its potential applications in optics, energy conversion and storage, electronics, sensor devices.

Chapter 2 provided an overview of the most prominent method of nanofabrication used in this dissertation, soft lithography; a family of techniques for replicating micro/nano structures using elastomeric stamps. Starting from the polymer replicas of the Si nanopillars arrays made via soft lithographic processes several structures were fabricated such as arrays of nanocylinders, nanocoaxes and nanotriaxs. Several ancillary techniques were used in the fabrication process: plasma vapor deposition, atomic layer deposition, mechanical polishing, and reactive ion etching.

Chapter 3 described the working principle and experimental setup for nanocoax-based capacitive sensors. The sensing performance of coax arrays having porous, porous + cavity and nonporous + cavity annulus were investigated to determine therole of the porous dielectric in the coax gas sensor. Different approaches were used to address issues associated with instability in capacitance and irreproducibility of the response of the arrays of nanocoax were also presented. Furthermore, we showed evidence for the superiority of the 3D nanocoax configuration over 2D/planar architectures for gas sensing applications.

Chapter 4 detailed the experimental setup and measurement techniques for the development of an electrochemical sensor with a nanoscale electrode gap. Nanocoax arrays with areal density ~10^6 per square millimeter were prepared with different gaps, with smaller gaps yielding higher sensitivity. A coax-based sensor with a 100 nm gap was found to have sensitivity 90 times greater than that of a planar sensor control, which had conventional millimeter-scale electrode gap spacing. We investigated the capability of nanocoax-based *vs.* planar ESs to detect the different concentrations of p-aminophenol.

In Chapter 5 we used self-limited electropolymerization of phenol in 2D planar and 3D nanostructure electrodes to synthesize a thin film of non-conducting molecularly-imprinted polymer film of thickness comparable in size to the template molecule for sensitive and selective detection of biomolecules in an aqueous solution. Various concentrations of the biomolecule, streptavidin, were used to optimize imprinting sites on the polymer film. The molecularly-imprinted polymer-based electrochemical 2D sensors showed excellent response over a wide range (~10^4) of concentrations of the template protein, streptavidin, with a limit of detection of 1 pg L^{-1} (~20 aM) and high selectively with respect to non-imprinted molecules. The results of the several attempts made to develop a molecular imprinted polymer on 3D nanostructures were also presented.

Appendix I will report the fabrication process and optical properties of arrays of hollow metallic structures.

Appendix I

Hollow Metallic Nanocylinders

1 Introduction

Arrays of, hollow metallic nanostructures have received some attention of late due to perceived applicability in biochemical sensing, [1,2] and energy storage, amongst others. Various template techniques have been used to make this type of nanostructure [3–8]. However, it remains a challenge to fabricate metallic nanocylinders without artifacts and defects. Here, we use nanoimprint lithography (NIL) followed by mechanical polishing and reactive ion etching (RIE) processes to make regular arrays of nanocylinders. Optical properties of an array of Au nanocyliders on glass substrates fabricated this way are presented.

2 Fabrication

To make hollow metallic nanostructures, we metallized the surfaces of SU-8 nanopillar arrays using a PVD system (usually putter deposition, though thermal and electron beam evaporation can be employed, albeit with reduced conformality) followed by mechanical polishing to remove metal from the top of the nanopillar, and reactive ion etching (RIE) to remove the polymer from the core of the pillar. To avoid SU-8 nanopillar shape degradation due to plastic flow, this metallization needs, as do all subsequent process steps, to be performed at the lower of the glass transition or polymerization temperature of SU-8. Figure A.1(a) shows an illustration of the fabrication scheme for nanocylinder arrays.

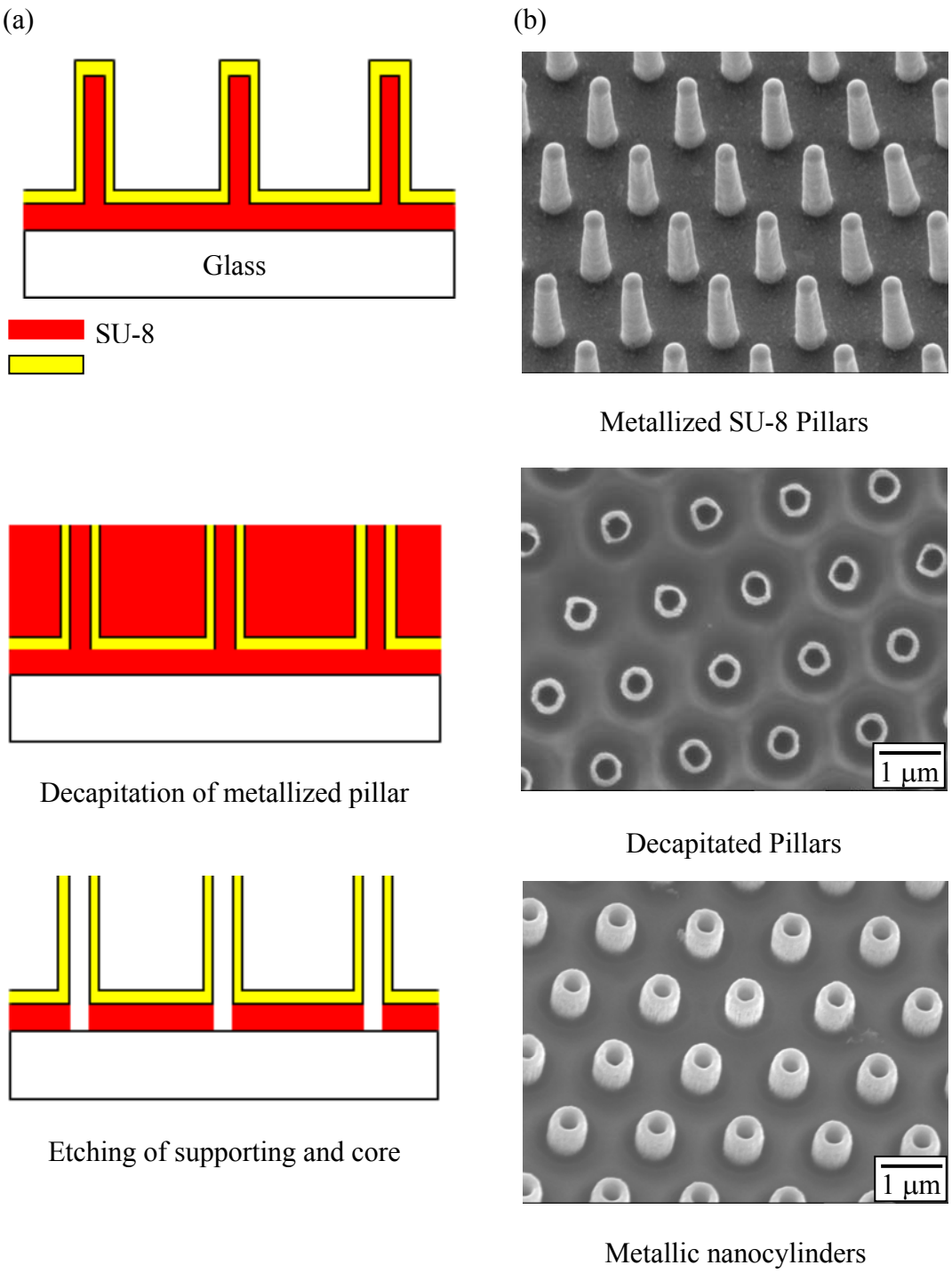

Figure A.1 (a) Schematic representation of fabrication of metallic cylinders. (b) SEM images of a hollow gold cylinder array at different stages of fabrication, from top to bottom: metallized SU-8 nanopillar array of pitch 1.3 μm, polished nanopillar array embedded in SU-8 film, hollow metallic nanocylinder array with 300 nm inner radii and 1.8 μm height.

We used 20–100 nm thick Au, Ag, Cr, Ti and combinations thereof for the metallization step, deposited by sputter deposition, as well as Pt by atomic layer deposition (ALD). The thickness of the sputtered metal coating in vertical nanostructures was not always uniform, being typically 10–20% thicker (measured radially) at the top than at the bottom. Not surprisingly, we found improved conformality of coating on conical, compared to strictly vertical structures. Typically, and depending on pillar height, the radial thickness of the metal on the wall of the conical pillar was one third to one half that of the vertical thickness of the metal on the "floor" between pillars. Before polishing, support for each nanopillar was provided by coating the array with a second SU-8 stabilizing layer, filling the space between the pillars to a thickness comparable to or greater than the height of the pillars. Mechanical polishing is then done by using suspensions of 50 nm alumina nanoparticles on a vibratory polisher, typically for several hours per run. Polishing/inspection cycles continue until the metal on the top of the pillars has been either exposed or fully removed, thus exposing the SU-8 centers. RIE is performed in a Plasma-Therm Versaline inductively-coupled reactive ion etch (ICPRIE) system with 20 SCCM flow of CF_4 at 0.5 Pa pressure, 200W power and 355 V self-bias conditions, which produces an etch rate _5 nm/s for SU-8. Figure A.1 (b) shows SEM images at different stages of fabrication of arrays of hollow metallic (Au) nanocylinders of 1.3 μm pitch, 300 nm inner diameter, 450 nm outer diameter and 1.8 μm height. We have made similar arrays with pitches between 900 nm and 1.5 μm.

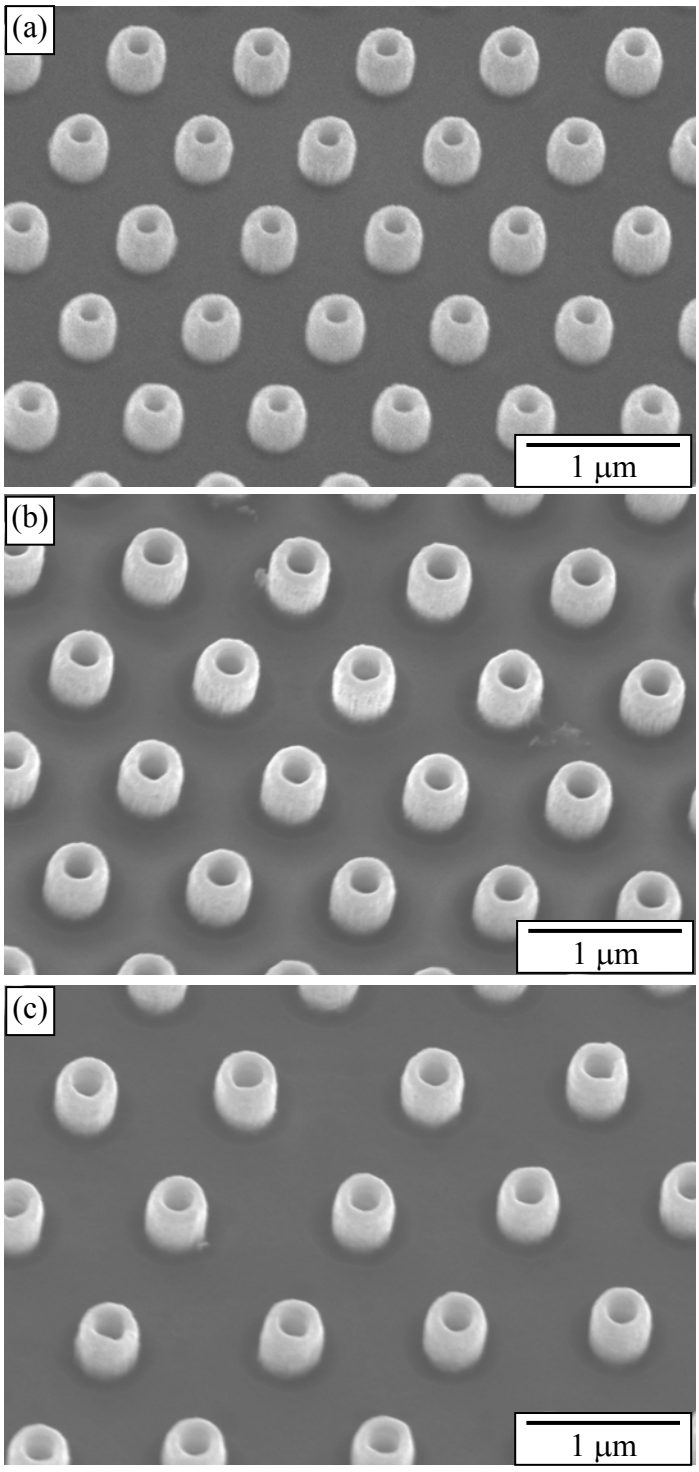

Figure A.2 SEM images of hollow Cr nanocyliders of different pitches, from top to bottom: 900 nm, 1100 nm, and 1300 nm.

In addition, inner diameter tuning is facilitated by isotropic or anisotropic etching of the master Si-NP arrays or of the replicated SU-8 arrays, outer diameter by metal film deposition time, height by polishing time, and depth (inside the metal cylinder) by etch time and/or process (*i.e.* wet or dry etch). As such, this fabrication method has been used to make arrays of different metals, pitch, radius, and height of hollow metallic nanocylinders.The pitch of the arrays always matches that of the master used to make the replica. Our template method may be an improvement over a previously reported method [9], especially to make arrays of nanocylinders of hard metals like Cr and W without artifacts and defects. Figure A.2 shows Cr nanocylinders of different pitches.

3. Optical properties

Hollow metallic nanostructures have interesting optical properties [10,11]. Optical properties of an array of subwavelength diameter Au nanocylinders embedded in polymer on a glass substrate have been studied by using a Nanonics MultiView 4000 nearfield scanning optical microscope (NSOM) and a Leica DM 6000 optical microscope. The top panel of Figure A 3 shows an NSOM image of a Au nanocylinder array (Au thicknesses: 30 nm wall, 90 nm floor), illuminated from below with λ = 532 nm light. The bottom panel is an optical micrograph of the sample, illuminated from below with white light.

These images show light not just emerging from the subwavelength holes, but the mere fact that the microscope formed an image illustrates that the emerging light was able to launch into the far-field. We also measured the optical transmission of an Au nanocylinder array using a double-integrating-sphere photospectrometer.

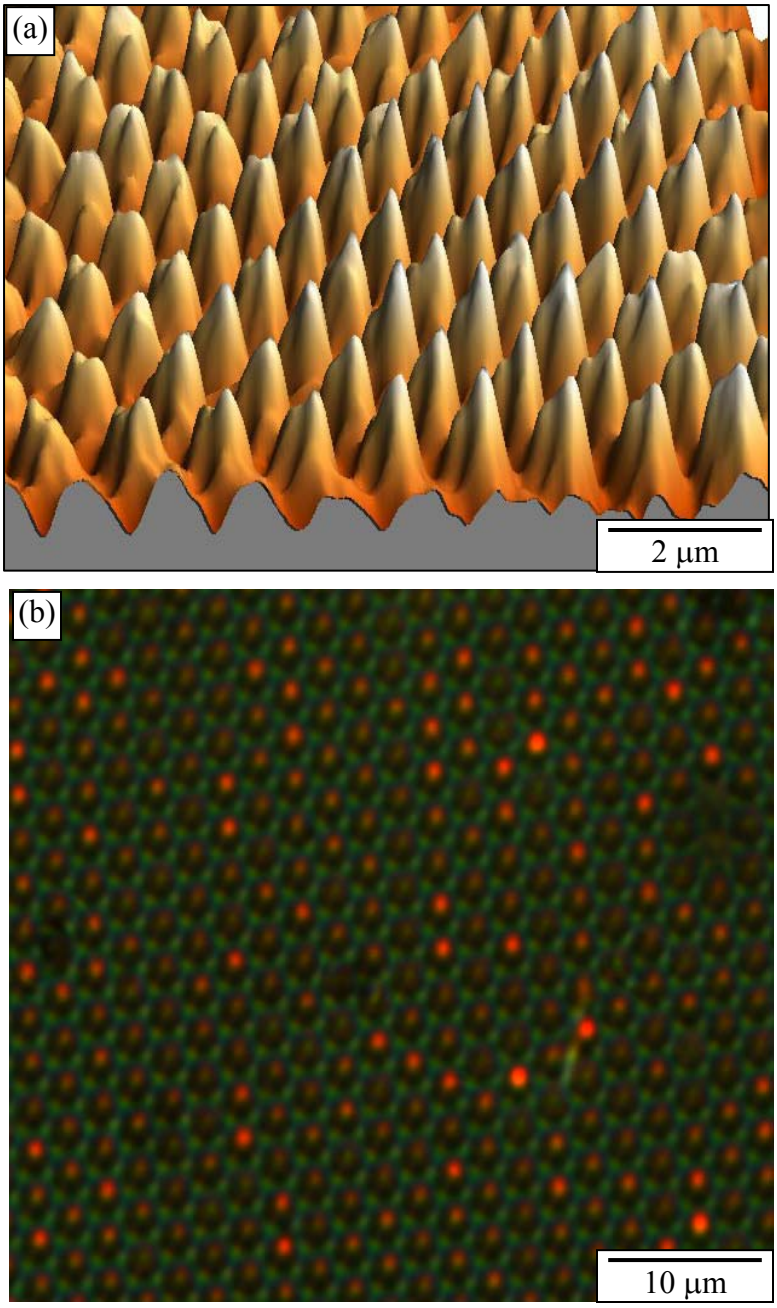

Figure A.3 (a) NSOM micrograph of 532 nm light passing through an array of nanocylinders of 1.3 μm pitch and subwavelength diameter and (b) optical micrograph of the arrays illuminated with white light from below.

As shown in Figure A.4 the transmission is dominated by light in the 600–800 nm wavelength range (red color bright spots on microscope images), significantly larger than the inner radius, of the arrays.This transmission through an array of nanocylinders may be associated with resonant coupling of local surface plasmons in the cylindrical cores with incident light [11]. Thus, arrays of such nanocylinders could serve as a basic tool to study and characterize nanoscale manipulation of light.

Summary

We have fabricated arrays of vertically-aligned, hollow metallic nanocylinders with different pitches and metals starting with NIL-fabricated nanopillars.. We demonstrated anomalous transmission of light from subwavelength-diameter nanocylinders using NSOM and far filed optical microscope. Enhanced optical transmission due to the nanocylinders array may be due to resonant coupling of plasmons in the cores of cylinders with incident light.

References

[1] E. M. Larsson, J. Alegret, M. Käll, and D. S. Sutherland, Nano Lett. **7**, 1256 (2007).

[2] W. Kubo and S. Fujikawa, Nano Lett. **11**, 8 (2011).

[3] N.-G. Cha, B. K. Lee, T. Kanki, H. Y. Lee, T. Kawai, and H. Tanaka, Nanotechnology **20**, 395301 (2009).

[4] M. D. Dickey, E. A. Weiss, E. J. Smythe, R. C. Chiechi, F. Capasso, and G. M. Whitesides, ACS Nano **2**, 800 (2008).

[5] S. G. Jang, H. K. Yu, D.-G. Choi, and S.-M. Yang, Chem. Mater. **18**, 6103 (2006).

[6] D. J. Lipomi, R. V. Martinez, and G. M. Whitesides, Angew. Chem. Int. Ed. **50**, 8566 (2011).

[7] Q. Xu, R. Perez-Castillejos, Z. Li, and G. M. Whitesides, Nano Lett. **6**, 2163 (2006).

[8] S. Soleimani-Amiri, A. Gholizadeh, S. Rajabali, Z. Sanaee, and S. Mohajerzadeh, RSC Adv. **4**, 12701 (2014).

[9] Q. Xu, R. Perez-Castillejos, Z. Li, and G. M. Whitesides, Nano Lett. **6**, 2163 (2006).

[10] T. W. Ebbesen, H. J. Lezec, H. F. Ghaemi, T. Thio, and P. A. Wolff, Nature **391**, 667 (1998).

[11] A. Krishnan, T. Thio, T. J. Kim, H. J. Lezec, T. W. Ebbesen, P. A. Wolff, J. Pendry, L. Martin-Moreno, and F. J. Garcia-Vidal, Opt. Commun. **200**, 1 (2001).

Appendix II

Imprint-Templated Nanocoax Array Architecture: Fabrication and Utilization

B. Rizal, F. Ye, P. Dhakal, T. C. Chiles, S. Shepard, G. McMahon, M. J. Burns, and M. J. Naughton
Nano-Optics for Enhancing Light-Matter Interactions on a Molecular Scale;
edited by
B. Di Bartolo, J. Collins, and L. Silvestri
Springer: Dordrecht, Netherlands, 359 (2013).

ISBN 978-94-007-5312-9

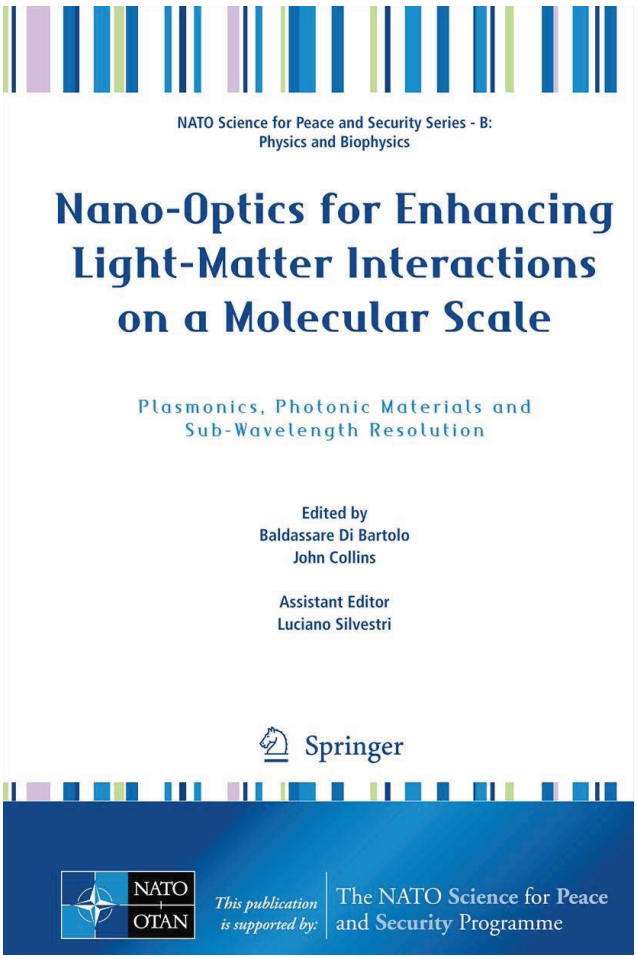

18
Imprint-Templated Nanocoax Array Architecture: Fabrication and Utilization

B. Rizal, F. Ye, P. Dhakal, T.C. Chiles, S. Shepard, G. McMahon, M.J. Burns, and Michael J. Naughton

18.1 Introduction

Arrays of vertically-oriented cylindrical, coaxial and triaxial nanostructures are fabricated from polymer nanopillar arrays prepared by nanoimprint lithography. With particular process modifications, these arrays have wide potential utility, including as molecular-scale biological (biomarker, pathogen, etc.) and chemical (explosives, environmental agents, etc.) sensors, high density neuroelectronic interfaces and retinal prostheses, radial junction photovoltaic solar cells, ultracapacitors, and optical metastructures. We report on their fabrication and example utilizations in the latter of these areas, with arrays of typical area density 10^6 mm^{-2}.

Vertically-oriented metallic nanowire and semiconducting or insulating nanopillar arrays are finding increasing use for a wide range of novel and enabling applications in, for example, electronics [1], photovoltaics [2, 3], optics [4, 5], and biochemical sensing [6–9]. Metal nanowire arrays are usually formed by electrodepositing metal in the pores of a nanoporous template, such as anodized aluminum oxide (AAO) or polycarbonate track-etch membranes, and removing/dissolving the template. Semiconducting nanowire arrays can be formed by etching a crystalline semiconductor such as silicon, or by epitaxially growing wires on a crystalline substrate. AAO-based nanowire arrays are quasi-ordered in the plane, while semiconductor nanopillar arrays can be random or well-ordered.

B. Rizal • F. Ye • P. Dhakal • M.J. Burns • M.J. Naughton (✉)
Department of Physics, Boston College, Chestnut Hill, MA 02467, USA
e-mail: naughton@bc.edu

T.C. Chiles
Department of Biology, Boston College, Chestnut Hill, MA 02467, USA

S. Shepard • G. McMahon
Nanofabrication Clean Room, Boston College, Chestnut Hill, MA 02467, USA

B. Di Bartolo et al. (eds.), *Nano-Optics for Enhancing Light-Matter Interactions on a Molecular Scale*, NATO Science for Peace and Security Series B: Physics and Biophysics, DOI 10.1007/978-94-007-5313-6_18,

Nanoimprint lithography (NIL) is a useful technique for rapid and inexpensive replication of nanostructures [10], including those with 3D features such as the nanowire/pillar arrays of interest here. NIL involves coating a prepared "master" nanostructure with an elastomer to form a mold that serves as the negative of the master. A common elastomer is polydimethyl-siloxane (PDMS). After separation from the master, this mold is used to stamp imprint its shape onto a another resist atop a substrate [11], forming a nearly exact replica of the master. Due to the properties of the stamp, even nontrivial 3D structures can be accurately replicated with NIL. Aside from its nanoscale fidelity, perhaps the greatest advantage of the NIL technique is its ability to produce a large number of replicas from a single master.

One structure in which these virtues are manifest is a nanocoaxial array. That is, NIN-prepared nanopillar arrays can be used as starting points for the fabrication of vertically-oriented mono-axial (solid or hollow cylinders), coaxial, triaxial, *etc.* arrays, which have a number of potential technological uses. Here, we describe the NIL-initiated fabrication of variants of such arrays, and their potential utilization as optical waveguides and metamedia.

18.2 Fabrication

18.2.1 Nil Replication of Nanopillar Arrays

As mentioned, NIL utilizes an elastomer to make a flexible mold from a robust master and a photopolymer, such as a photoresist (PR), to make polymeric replicas of the master. As NIL masters in this report, silicon nanopillar (Si-NP) arrays were prepared by a combination of thermal oxidation and reactive ion etching of silicon substrates that were photolithographically patterned. Typical Si-NP dimensions were 2 μm height and 200 nm diameter, in hexagonal close-packed arrays with periodicity/pitch between 0.8 and 1.5 μm, on substrates containing 10×20 mm^2 areas of Si-NP arrays. In addition to vertical pillars, conical and sloped cross-section pillars were prepared with similar average dimensions. These latter ones can facilitate improved step coverage (conformality) of subsequent coatings, relative to that achievable with strictly vertical pillars. PDMS molds were prepared by NIL using a custom clamp apparatus that also facilitated subsequent thermal and/or photopolymerization of resist for replicas. We used SU-8 [12] resist for the NP replicas, chosen for its relatively low glass transition temperature, low volume shrinkage coefficient, and wide range of operating temperatures. Application of heat and pressure between the mold and the substrate coated with SU-8 helps to transfer the pattern from mold to substrate. A single mold can be used to make many replicas without requiring cleaning, and many replicas can be made from a single master. Figure 18.1 shows scanning electron microscope (SEM) images of a representative Si-NP master/PDMS stamp/SU-8 replica set. Note the high fidelity of the replicant

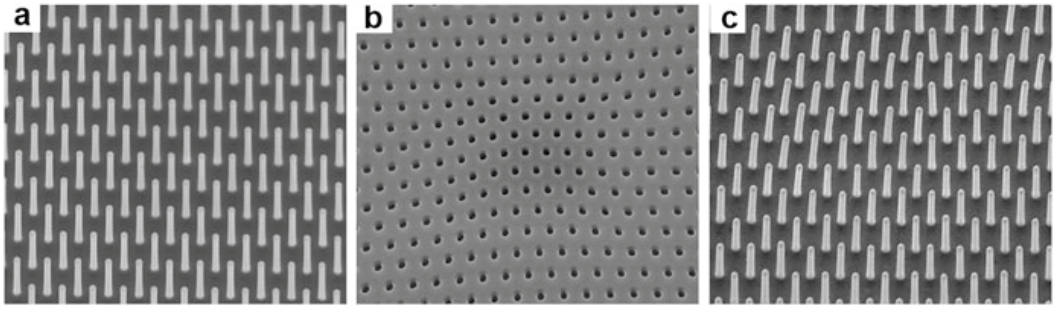

Fig. 18.1 SEM images of the SUV-NIL process. (**a**) Arrays of vertical 2 μm-tall Si nanopillars of period 1.5 μm used as master. (**b**) PDMS mold of the master. (**c**) SU-8 replica of the master

features with respect to the master. Below, we describe the fabrication and potential applications of vertically-oriented arrays of metallic nano-cylinder, coax, and triax arrays of SU-8 nanopillars made by the NIL process.

18.2.2 Fabrication of Hollow Metal Nanocylinders

The simplest nanopillar array-based structure to fabricate via NIL, aside from nanopillar replicas themselves, is a metal cylinder. To make this structure, we metallized the surfaces of SU-8 nanopillar arrays using a PVD system (usually sputter deposition, though thermal and electron beam evaporation can be employed, albeit with reduced conformality) followed by mechanical polishing to remove metal from the top of the nanopillar, and reactive ion etching (RIE) to remove the polymer from the core of the pillar. To avoid SU-8 nanopillar shape degradation due to plastic flow, this metallization needs, as do all subsequent process steps, to be performed at the lower of the glass transition or polymerization temperature of SU-8. Figure 18.2 shows an illustration of the fabrication scheme for nanocylinder arrays. We used 20–100 nm thick Au, Ag, Cr, Ti and combinations thereof for the metallization step, deposited by sputter deposition, as well as Pt by atomic layer deposition (ALD). The thickness of the sputtered metal coating in vertical nanostructures was not always uniform, being typically 10–20% thicker (measured radially) at the top than at the bottom. Not surprisingly, we found improved conformality of coating on conical, compared to strictly vertical structures.

Typically, and depending on pillar height, the radial thickness of the metal on the wall of the conical pillar was one third to one half that of the vertical thickness of the metal on the "floor" between pillars. Before polishing, support for each nanopillar was provided by coating the array with a second SU-8 stabilizing layer, filling the space between the pillars to a thickness comparable to or greater than the height of the pillars. Mechanical polishing is then done by using suspensions of 50 nm alumina nanoparticles on a vibratory polisher, typically for several hours per run. Polishing/inspection cycles continue until the metal on the top of the pillars

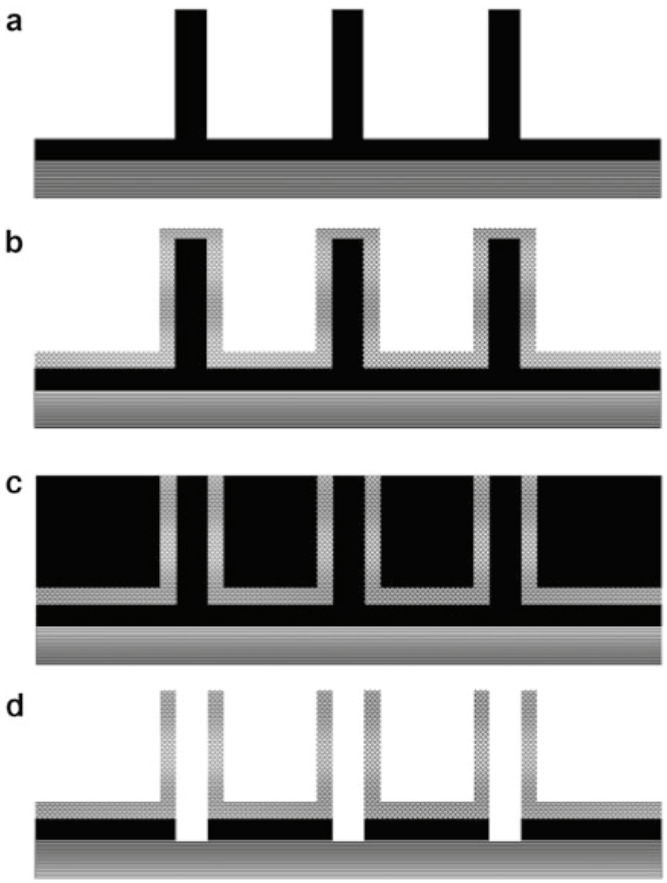

Fig. 18.2 Summary of the procedure used to fabricate arrays of hollow metallic nanocylinder from the polymer pillars. (**a**) Polymer nanopillar array. (**b**) Inner metal coating. (**c**) Polymer coating; (**d**) Etching of polymer

has been either exposed or fully removed, thus exposing the SU-8 centers. RIE is performed in a Plasma-Therm Versaline inductively-coupled reactive ion etch (ICP-RIE) system with 20 SCCM flow of CF_4 at 0.5 Pa pressure, 200 W power and 355 V self-bias conditions, which produces an etch rate ~5 nm/s for SU-8. Figure 18.3 shows SEM images at different stages of fabrication of arrays of hollow metallic (Au) nanocylinders of 1.3 μm pitch, 300 nm inner diameter, 450 nm outer diameter and 1.8 μm height. We have made similar arrays with pitches between 800 nm and 1.5 μm. In addition, inner diameter tuning is facilitated by isotropic or anisotropic etching of the master Si-NP arrays or of the replicated SU-8 arrays, outer diameter by metal film deposition time, height by polishing time, and depth (inside the metal cylinder) by etch time and/or process (*i.e.* wet or dry etch).

As such, this fabrication method has been used to make arrays of different metals, pitch, radius, and height of hollow metallic nanocylinders. The pitch of the arrays always matches that of the master used to make the replica. Our template method may be an improvement over a previously reported method [13], especially to make arrays of nanocylinders of hard metals like Cr and W without artifacts and defects. Figure 18.4 shows two examples with Cr.

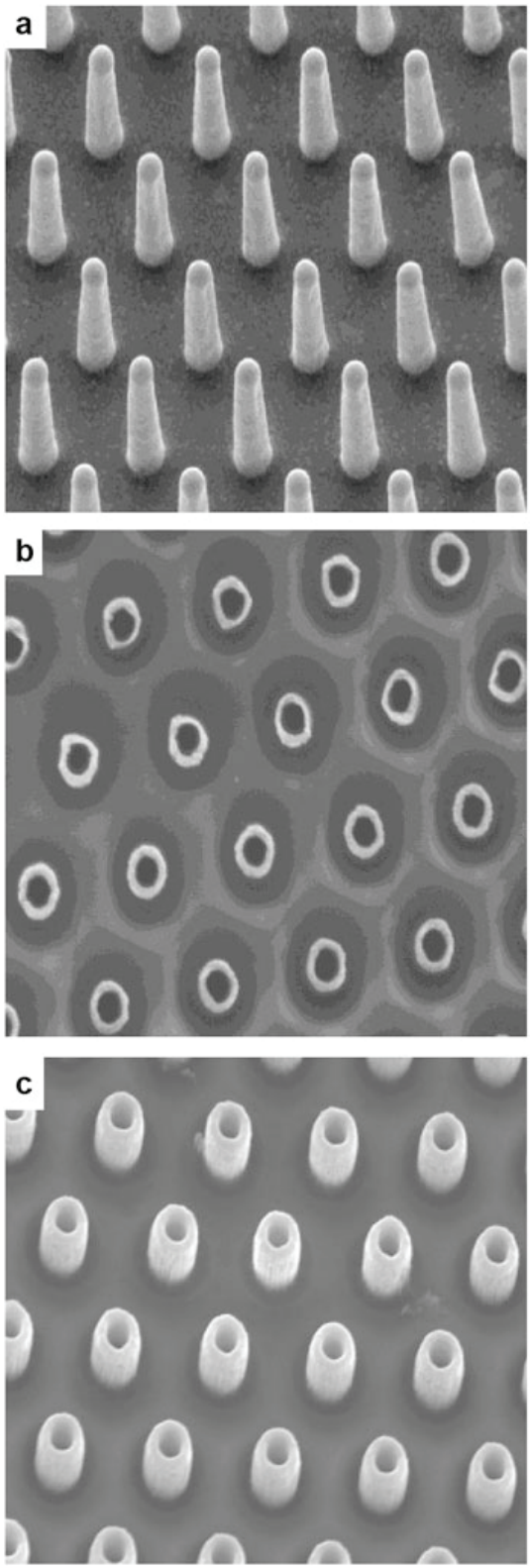

Fig. 18.3 SEM images of a hollow gold cylinder array at different stages of fabrication. (**a**) Metallized SU-8 nanopillar array of pitch 1.3 μm. (**b**) Polished nanopillar array embedded in SU-8 film. (**c**) Hollow metallic nanocylinder array with 300 nm inner radii and 1.8 μm height

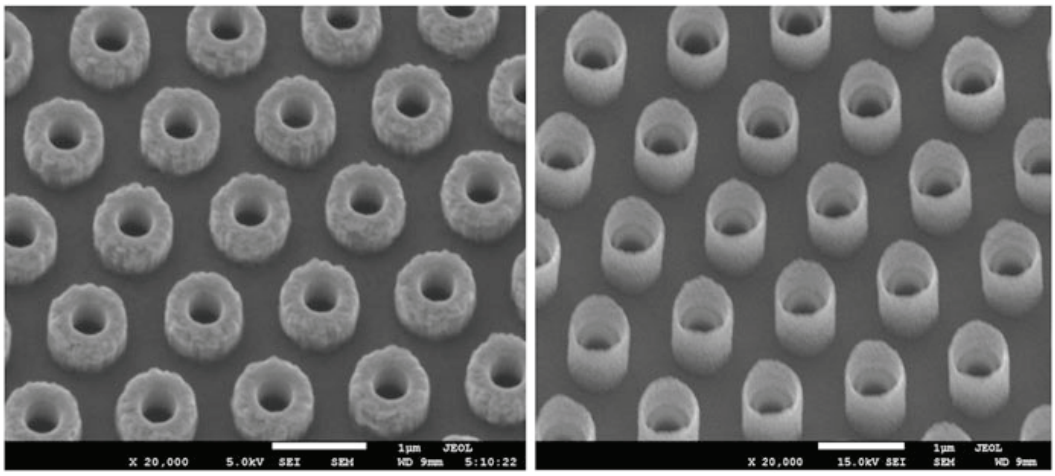

Fig. 18.4 Hollow metallic (Cr) cylinder arrays of various dimensions. Scale bars = 1 μm

18.2.3 Fabrication of Nanocoaxes

To form nanocoaxes, the first steps are as stated above through NP metallization (*i.e.* Figs. 18.2b and 18.3a). Figure 18.5 depicts the steps involved to fabricate arrays picking up from this point. After the initial metallization, we deposit a dielectric layer. We have deposited different kinds of dielectrics using different methods, including ALD, plasma enhanced chemical vapor deposition (PECVD), sputtering, and spin-coating, to deposit films anywhere between 10 and 200 nm thick (measured radially) of porous or nonporous dielectrics such as Al_2O_3, SiO_2, Si_3N_4, polymer, *a*-Si, *etc*. For ALD of Al_2O_3, we used trimethylaluminum (TMA) as precursor, whereas for PECVD SiO_2, and Si_3N_4, a gas mixture with ratio SiH_4/N_2O : 2/9 has been used at 200 °C. Reactively-sputtered Al_2O_3 deposition is done by introducing O_2 gas in ratio 1:6 to Ar during deposition of Al at room temperature. Of the three deposition methods, ALD and spin-coating yield the most conformal and dense coatings of dielectrics, especially on strictly vertical structures. In an early nanocoax application, the dielectric annulus was prepared as a radial *p-i-n* junction with amorphous silicon (*a*-Si), so that the array functioned as a photovoltaic solar cell [2].

Next, an outer metal film is deposited, of typical thickness 20–100 nm to form a nanocoaxial structure. For many applications, such as biological, chemical and neurological sensing, and for the study of nanoscopic effects of light propagation, the top ends of coax structures are removed ("decapitated" by mechanical polishing), forming open-ended nanocoaxes, as depicted in Fig. 18.5. In some cases, the arrays are processed further by etching the annuli and/or the cores inside the inner coax metal, by processes similar to those employed in the fabrication of hollow nanocylinder arrays, Figs. 18.2, 18.3, and 18.4 above. Such examples are shown in Fig. 18.6 (including full process steps) and Fig. 18.7 below.

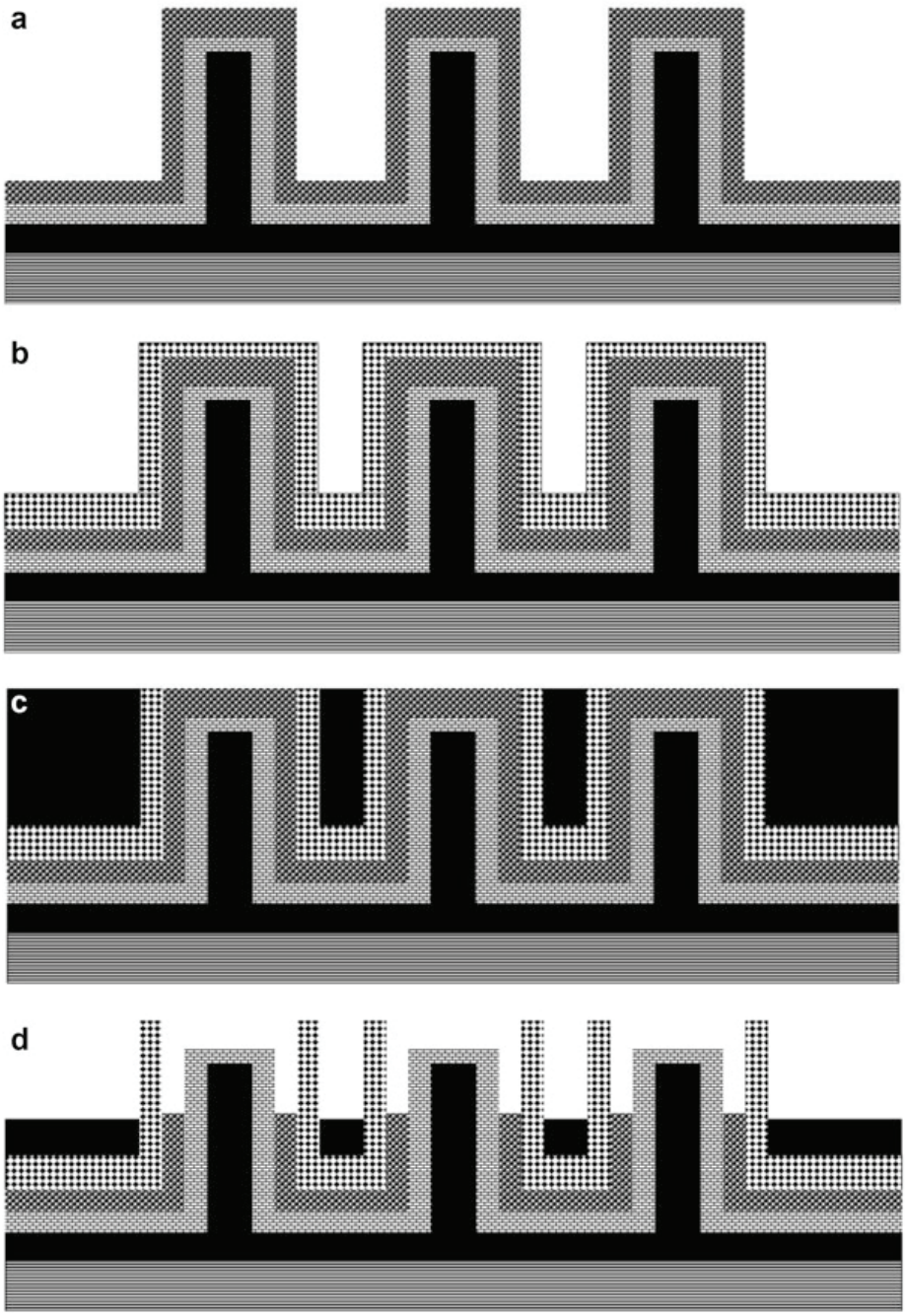

Fig. 18.5 Schematic representations of fabrication process for nanocoax arrays. (**a**) Dielectric coating. (**b**) Outer metal coating. (**c**) Polymer coating. (**d**) Etching of dielectric

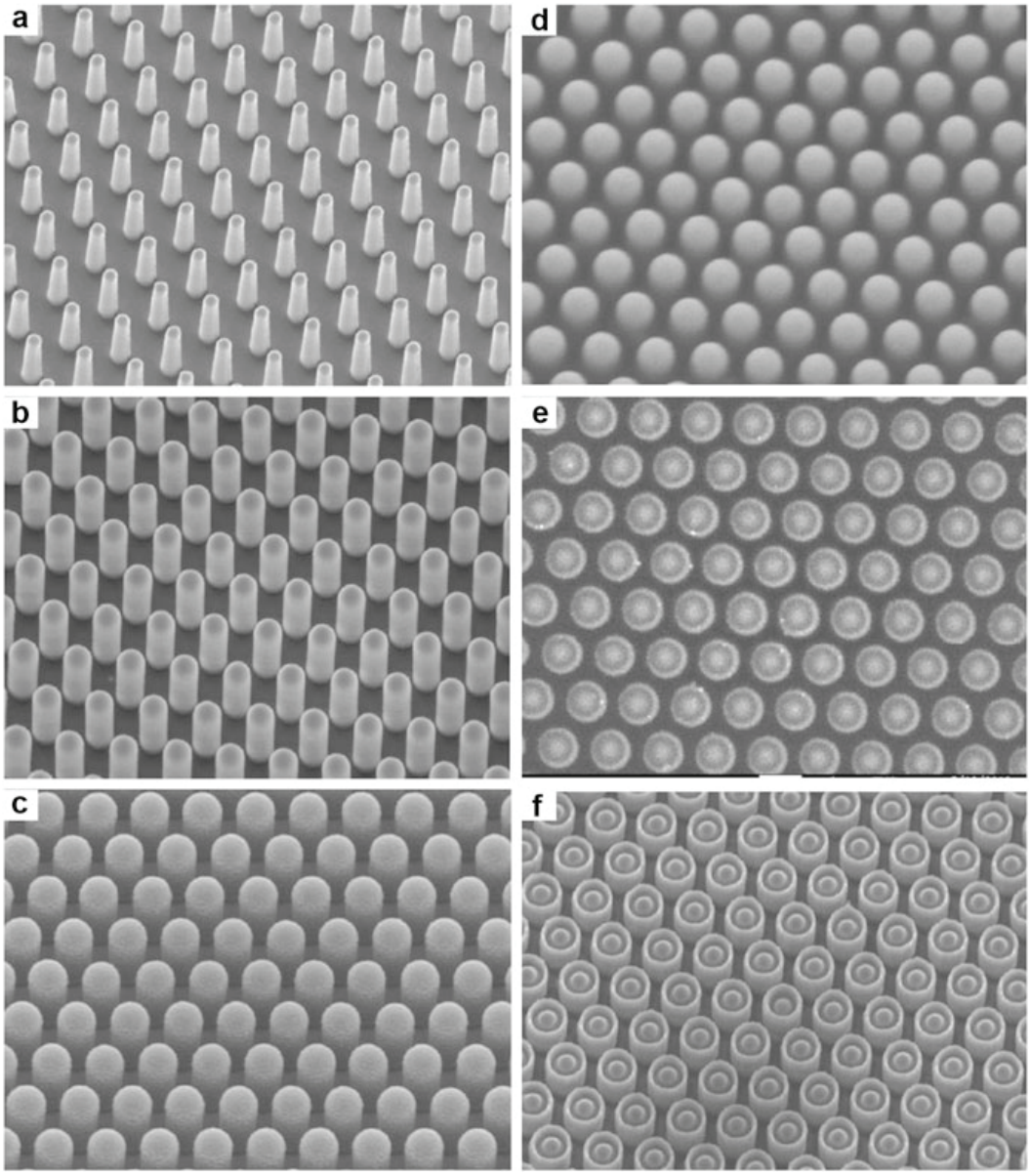

Fig. 18.6 SEM images of the fabrication process for open ended nanocoax structure of 1.3 μm pitch and 2 μm height. (**a**) Inner metal coating. (**b**) Dielectric coating. (**c**) Outer metal coating. (**d**) SU-8 coating. (**e**) Mechanical polishing. (**f**) Etching of dielectric

18.3 Optical Utilization

18.3.1 Light Transmisson Through Hollow Metallic Nanocylinders

Hollow metallic nanostructures have interesting optical properties. The top panel of Fig. 18.8 shows the results of finite-difference time-domain (FDTD) simulation of 500 nm light through an array of conical Au nanocylinders of 1.3 μm pitch, 1.8 μm

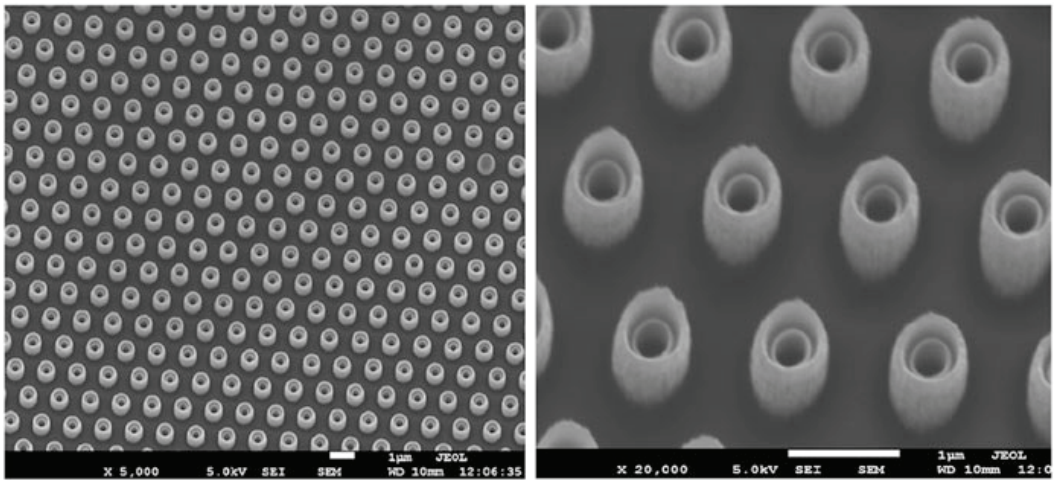

Fig. 18.7 Nanocoax array with hollow core and hollow annulus. Scale bars = 1 μm

height, and 300 nm base diameter. Despite the nanocylinders dimensions being subwavelength in diameter, the simulations indicate that light should be able to propagate through them. This is confirmed in the center panel of Fig. 18.8, in a near-field scanning optical microscope (NSOM/SNOM) image of a sample illuminated from below with $\lambda = 500$ nm light. The bottom panel is an optical micrograph of the sample, illuminated from below with white light, clearly showing light not just emerging from the subwavelength holes, but the mere fact that the microscope formed an image illustrates that the emerging light was able to launch into the far-field. The transmission is dominated by light in the 600–700 nm wavelength range (bright spots are red in color), significantly larger than the inner radius, such that some degree of subwavelength propagation into the far field occurs. This transmission may be associated with resonant coupling of local surface plasmons in the cylindrical cores with incident light [14]. Thus, arrays of such nanocylinders could serve as a basic tool to study and characterize nanoscale manipulation of light.

18.3.2 Light Transmisson Through Nanocoaxes

The coaxial cable is known to be an ideal geometry for the efficient propagation of electromagnetic waves, being one of only two configurations (the other being a semi-infinite parallel plate) that propagates a transverse electromagnetic mode (TEM). For perfect electrical conductors, this mode has no cutoff free, while the TE_{mn} modes cut off at wavelengths larger than the average of the circumferences of the inner and outer conductors [15]. A nanoscale version of a coax, a nanocoax, operates similarly [16], with the exception that, for high enough frequency (*i.e.* visible), the radiation can interact with the metals comprising the waveguide. Transmission in a nanoscale coax as been shown theoretically to propagate in a

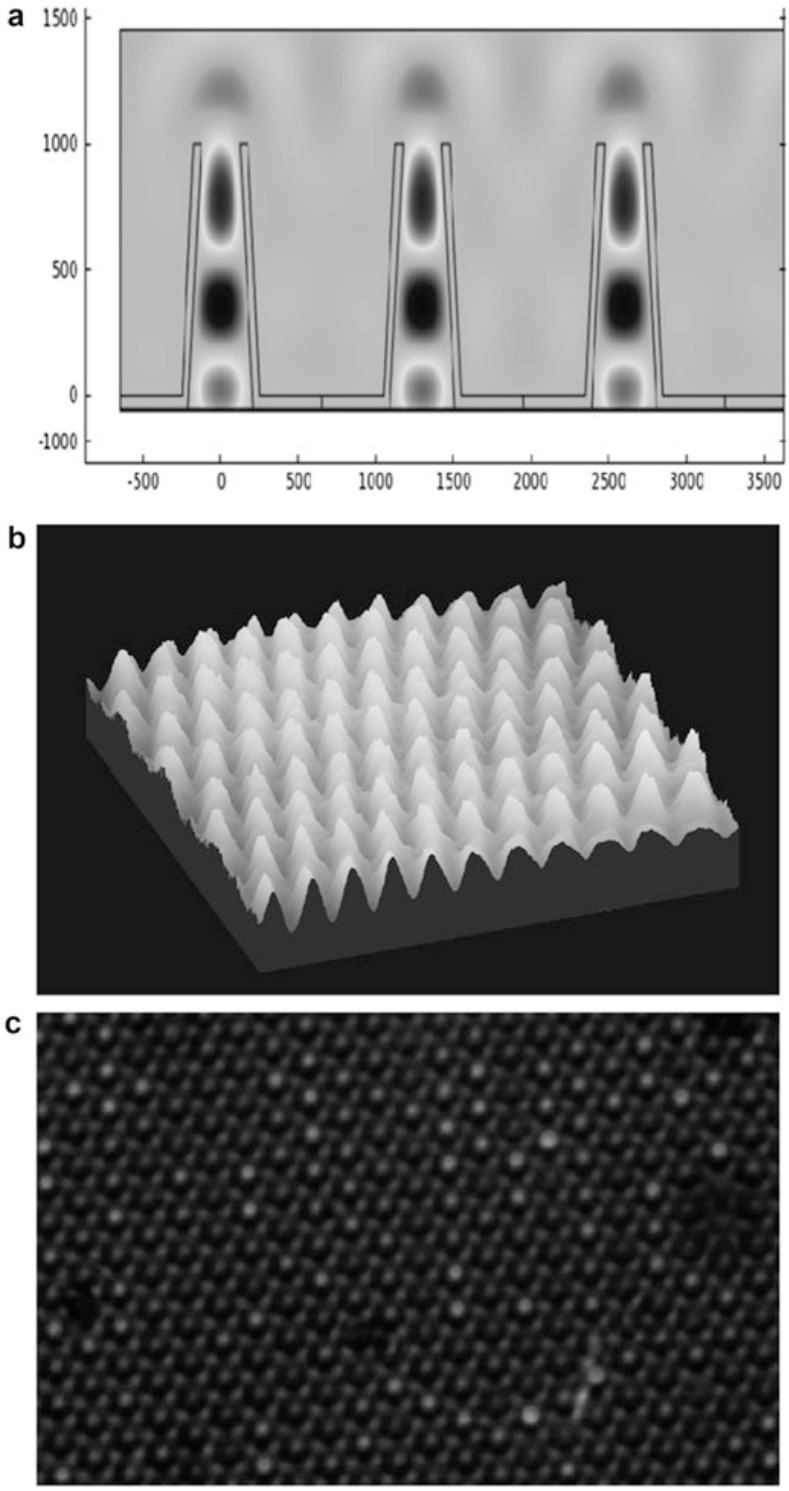

Fig. 18.8 (**a**) Simulation of light passing through an array of subwavelength nanocylinders as described in the text. (**b**) NSOM micrograph of 500 nm light passing through an array of subwavelength nanocylinders. (**c**) Optical micrograph of an array of subwavelength nanocylinders illuminated with light from below, showing transmission peaked in the bright spots

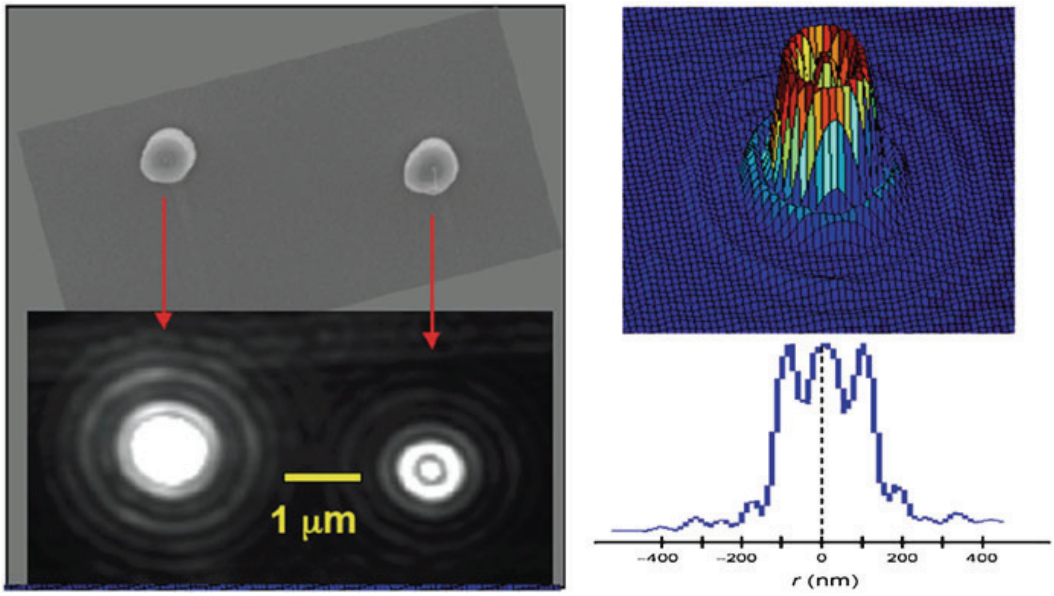

Fig. 18.9 (**a**) SEM top view of two isolated nanocoaxes with 150 nm diameter core and 100 nm thick annulus. (**b**) Optical micrograph of light emanating out the tops of the two coaxes, illuminated from below. (**c**) Light intensity map of right coax. (**d**) Line cut along a radial direction of transmitted light intensity

TM_{00} mode, which reduces to the TEM in the appropriate wavelength regime [17]. Nanocoaxes fabricated for optical purposes at Boston College indeed have been shown to transmit light for wavelengths larger than the nanocoax [5].

In Fig. 18.9, we show a scanning electron micrograph of two vertically-oriented nanocoaxes surrounded by an optically-opaque (150 nm thick W) film. The dielectric in the annuli of these coaxes is 100 nm thick ALD-deposited Al_2O_3, and the tops were exposed by focused ion beam milling. Immediately below this SEM is an optical micrograph of the same two nanocoaxes while illuminated by white light from below the opaque film. One can see in the optical image the transmission of the light, including Airy's rings [18] due to the diffraction-limited detection of the optical microscope that is observing the far field radiation emanating from the ends of the nanocoaxes. In the right panels, we show a 3D intensity map of the right nanocoax's emission pattern, and a line cut though the center of that pattern. This latter graph also shows Airy rings as spatial oscillations with a spacing of about 100 nm in the image.

In summary, we used imprint-templated lithography to replicate arrays of silicon nanopillars in SU-8 polymer, and used those replicated arrays to form arrays of metal nanocylinders and nanocoaxes (as well as nanotriaxes, *etc*., not discussed here). These structures can be employed in a variety of sensing applications, and for the nanoscale manipulation of light, including as radial-junction solar cells and nanophotonic waveguides. Examples of the latter were presented herein.

Acknowledgment This work was supported by the W.M. Keck Foundation and the US National Cancer Institute.

References

1. Duan X, Huang Y, Cui Y, Wang J, Lieber CM (2001) Indium phosphide nanowires as building blocks for nanoscale electronic and optoelectronic devices. Nature 409:66–69
2. Naughton MJ, Kempa K, Ren ZF, Gao Y, Rybczynski J, Argenti N, Gao W, Wang Y, Peng Y, Naughton JR, McMahon G, Paudel T, Lan YC, Burns MJ, Shepard A, Clary M, Ballif C, Haug F-J, Söderström T, Cubero O, Eminian C (2010) Efficient nanocoax-based solar cells. Phys Status Solidi Rapid Res Lett 4:181–183
3. Paudel T, Rybczynski J, Gao YT, Lan YC, Peng Y, Kempa K, Naughton MJ, Ren ZF (2011) Nanocoax solar cells based on aligned multiwalled carbon nanotube arrays. Phys Status Solidi A 208:924–927
4. Sirbuly DJ, Law M, Yan J, Yang P (2005) Semiconductor nanowires for subwavelength photonics integration. J Phys Chem B 109:1519–15213
5. Rybczynski J, Kempa K, Herczenski A, Wang Y, Naughton MJ, Ren ZF, Haung ZP, Cai D, Giersig M (2007) Subwavelength waveguide for visible light. Appl Phys Lett 90:021104
6. Zhao HZ, Rizal B, McMahon G, Wang H, Dhakal P, Kirkpatrick T, Ren ZF, Chiles TC, Naughton MJ, Cai D (2012) Ultrasensitive chemical detection using nanocoax sensor. ACS Nano 6:3171–3178
7. Kabashin AV, Evans P, Pastkovsky S, Hendren W, Wurtz GA, Atkinson R, Pollard R, Podolskiy VA, Zayats AV (2009) Plasmonic nanorod metamaterials for biosensing. Nat Mater 8:867–871
8. Holgado M, Barrios CA, Ortega FJ, Sanza FJ, Casquel R, Laguna MF, Banuls MJ, Lopez-romero D, Puchades R, Maquaieira A (2010) Label-free biosensing by means of periodic lattices of high aspect ratio SU-8 nanopillars. Biosens Bioelectron 25:2553–2558
9. Kubo W, Fujikawa S (2011) Au double nanopillars with nanogap for plasmonic sensor. Nano Lett 11:8–15
10. Chou SY, Krauss PR, Renstrom PJ (1996) Imprint lithography with 25-nanometer resolution. Science 272:85–87
11. Gates BD, Xu Q, Stewart M, Ryan D, Willson CG, Whitesides GM (2005) New approaches to nanofabrication: molding, printing, and other techniques. Chem Rev 105:1171–1196
12. Microchem Corporation, Newton, MA
13. Xu Q, Perez-Castillejos R, Li ZF, Whitesides GM (2006) Fabrication of high-aspect-ratio metallic nanostructures using nanoskiving. Nano Lett 6:2163–2165
14. Krishnan A, Thio T, Kim TJ, Lezec HJ, Ebbesen TW, Wolff PA, Pendry J, Martin-Moreno L, Garcia-Vidal FJ (2001) Evanescently coupled resonance in surface plasmon enhanced transmission. Opt Commun 200:1–7
15. Pozar D (2012) Microwave engineering, 4th edn. Wiley, New York
16. Kempa K, Wang X, Ren ZF, Naughton MJ (2008) Discretely guided electromagnetic effective medium. Appl Phys Lett 92:043114
17. Peng Y, Wang X, Kempa K (2008) TEM-like optical mode of a coaxial nanowaveguide. Opt Express 16:1758–1763
18. Airy GB (1835) On the diffraction of an object-glass with circular aperture. Trans Camb Philos Soc 5:283–291

Appendix III

Nanocoax-Based Electrochemical Sensor

B. Rizal, M. M. Archibald, T. Connolly, S. Shepard, T. C. Chiles, M. J. Burns, and M. J. Naughton

Analytical Chemistry **85**, 10040 (2013)

analytical chemistry

Technical Note

pubs.acs.org/ac

Nanocoax-Based Electrochemical Sensor

Binod Rizal,[†] Michelle M. Archibald,[‡] Timothy Connolly,[‡] Stephen Shepard,[§] Michael J. Burns,[†] Thomas C. Chiles,[‡] and Michael J. Naughton*,[†]

[†]Department of Physics, [‡]Department of Biology, [§]Integrated Sciences Cleanroom Facility, Boston College, Chestnut Hill, Massachusetts 02467, United States

Supporting Information

ABSTRACT: We have used a facile polymer imprint process to fabricate a three-dimensional electrochemical nanosensor, the sensitivity of which is two decades higher than that of planar controls. The device is composed of an array of vertically oriented nanoscale coaxial electrodes, with the coax cores and shields serving as integrated working and counter electrodes, respectively, each with a nanoscale separation gap (coax annulus width). Arrays of ~10^6 devices per square millimeter were prepared with different gaps, with smaller gaps yielding higher sensitivity. A coax-based sensor with a 100 nm gap was found to have sensitivity 90 times greater than that of a planar sensor control, which had conventional millimeter-scale electrode gap spacing. We suggest that this enhancement is due to the combination of rapid diffusion of molecules between the closely spaced electrodes and the large number of nanoscale electrochemical cells operating in parallel, both of which enhance current per unit surface area compared to planar or other nanostructured devices.

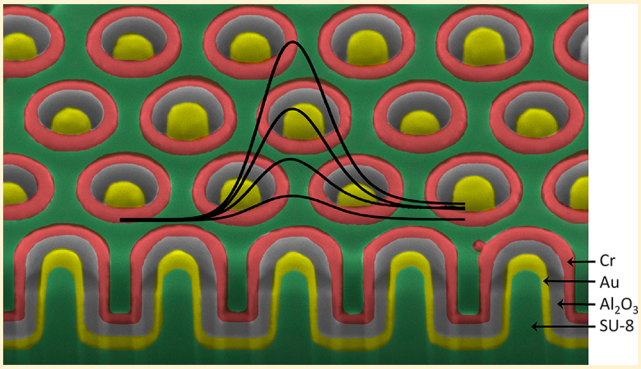

Considerable effort has been directed toward increasing target sensitivity in electrochemical sensors (ES) by developing "nanogap" electrodes that can provide real-time ultrasensitive detection of chemical and biological agents. Reduction of the distance between the electrodes has received considerable attention as this is thought to improve mass transport and Faradic-to-capacitive signal ratio, as well as decrease the response time and the effect of the solution resistance.[1−6] Lithographic techniques such as electron-beam,[7−9] dip-pen,[10] transmission electron beam ablation,[11] and focused ion beam (FIB) milling[12,13] can be used to make nanoscale gap electrodes. However, these methods are commonly used for planar, two-dimensional structures and are inevitably serial, costly, and time-consuming processes. Other techniques such as electromigration,[14,15] electrochemical deposition,[16,17] and electro-breakdown[18] are simpler and faster than the aforementioned techniques for planar nanogap electrode fabrication, but have limited flexibility in controlling the size and shape of the gap between the electrodes. Although different methods have been developed, it remains a challenge to fabricate highly ordered arrays of nanogap electrodes with confined geometries over a large area and to do so in a reproducible and cost-effective manner. We have developed a simple and reliable method for fabricating highly ordered arrays of electrodes with well-defined nanogaps over a large area for use in ES devices, maintaining the advantage of nanogap sensing while overcoming previous limitations. No formal lithographies (photo- or electron beam) are employed in the fabrication.

Our design for a simple, miniaturized ES consists of arrays of vertically oriented coaxial electrodes, termed "nanocoaxes". Variants of this structure have previously been employed in nanophotonic,[19,20] photovoltaic,[21,22] and capacitance-based chemical sensing[23] applications. It consists of two concentric electrodes separated by a dielectric layer or air gap. We fabricated ESs using these two electrodes as the working electrode (WE) and counter electrode (CE). ES arrays with different electrode gaps were prepared by changing the thickness of the dielectric layer and then removing it, with the resulting effect on the Faradic current examined via differential pulse voltammetry (DPV).

EXPERIMENTAL SECTION

Chemicals. 1*H*,1*H*,2*H*,2*H*-Perfluorodecyltrichlorosilane (96%) and *n*-heptane (99%) were purchased from Alfa Aesar. Acetone (99.5%), sulfuric acid (96%), and hydrogen peroxide (30%) were purchased from J.T. Baker. Polydimethylsiloxane (Sylgard 184 silicone elastomer kit) was purchased from Dow Corning. SU-8 2002 was purchased from MicroChem Corp. Transetch-N was purchased from Transene Co. Ferrocene carboxylic acid was purchased from Sigma-Aldrich. Phosphate buffered saline was purchased from Fisher Scientific.

Received: August 2, 2013
Accepted: October 3, 2013
Published: October 3, 2013

Preparation of Silicon Nanopillar Arrays. Silicon nanopillar (SiNP) arrays were prepared by a combination of thermal oxidation and reactive ion etching of [100] silicon substrates that were photolithographically patterned. Typical SiNP dimensions were 2 μm height and 200 nm diameter, with hexagonal close-packed arrays of 1.3 μm periodicity/pitch, on substrates containing 10 × 20 mm^2 areas of pillars. This results in a pillar density of approximately $10^6/mm^2$.

Application of Release Coating. A release coating was applied to the SiNP arrays, which were used as imprint masters. The master array was immersed in a solution containing 1*H*,1*H*,2*H*,2*H*-perfluorodecyltrichlorosilane (FDTS) and *n*-heptane in the ratio of 1:1000 (v/v), followed by immediate transfer of the master to acetone for another 5 min, and then baked for 5 min at 110 °C on a hot plate. The measured thickness of the FDTS using ellipsometry (J.A. Woollam VASE) was 1.76 nm ± 0.12 nm, which is comparable to the previously reported value for a single layer of FDTS.[24]

Fabrication of Molds. Polydimethylsiloxane (PDMS) was mixed in the ratio of 10:1 (w/w) with its curing agent and degassed in a bell−jar desiccator connected to a vacuum pump for 30 min. It was then poured onto the Si master, cured at room temperature for 12 h, and baked for 1 h on a hot plate at 90 °C. The PDMS mold was then peeled off and treated with release coating and used for imprinting in subsequent steps. Typical thickness of the PDMS mold was ∼2 mm.

Imprinting of SU-8 Pillar Arrays. A thin film of SU-8 2002 was spin-coated on a piranha-cleaned Si wafer at 500 rpm with acceleration of 110 rpm/s for 6 s and then at 3000 at 550 rpm/s for 36 s, followed by soft baking at 65 °C for 1 min and at 95 °C for at least 2 min to remove any residual solvent. The film was cooled to room temperature, and the mold was placed on top of it. To ensure conformal contact between the mold and the film, an overpressure of ∼10^5 Pa was applied between them using a homemade apparatus. The PDMS mold and SU-8 were then held at 95 °C on a hot plate for 5 min and exposed to UV light in a mask aligner (MA6, Karl Suss) at 12 mW/cm^2 for 90 s. A postexpose bake was then done for 5 min, and the sample was allowed to cool to room temperature before peeling off the PDMS elastomer mold to release the now-formed SU-8 nanopillar array.

Fabrication of Hollow Nanocoax Arrays. A thin film (∼125 nm) of Au was deposited as the SU-8 pillar array (to later serve as the coax inner conductors) using sputter deposition (AJA International) with 250 W dc power and 0.75 nm/s deposition rate. Atomic layer deposition (ALD) (Savannah S100, Cambridge Nanotech) was then used to deposit Al_2O_3 at 200 °C (to serve as coax annulus), followed by a second sputter deposition of ∼150 nm of Cr (for the outer coax conductor) with 200 W dc power and 0.1 nm/s deposition rate. A second layer of SU-8 was then spin-coated onto this newly formed coax array, followed by UV exposure at 12 mW/cm^2 for 90 s and a hard bake at 200 °C for 1 h. This is to provide mechanical support for the nanocoaxes. A mechanical polisher (Vibromet 2, Buehler) with a suspension of 50 nm diameter alumina nanoparticles was used for 2.5 h to remove the top part of the outer metal of the coax. After this decapitation, the Al_2O_3 in the annuli of the coaxes was etched to a time-controlled depth at room temperature at a rate of ∼20 nm/h by immersion in Transetch-N.

Characterization. Scanning electron microscope (SEM) images of the pillar and coax arrays were taken using a JEOL JSM-7001F SEM. FIB milling was done on a JEOL JIB-4500 FIB. The thicknesses of the thin films were measured by a profilometer (Dektak 150, Veeco). Electrochemical characterization was performed using a potentiostat (Reference 600, Gamry Instruments).

RESULTS AND DISCUSSION

We employed the above stamp imprint method in the fabrication of our nanocoax array electrochemical cells. Imprinting (also referred to as soft lithography or nanoimprint lithography[25]) is a useful technique for rapid and cost-effective replication of micro- and nanostructures, including those with 3D features such as the vertical nanopillar arrays of interest here. Aside from its nanoscale capability, perhaps the greatest advantage of the imprinting technique is its ability to produce a large number of large area replicas with high fidelity from a single master. We thus used imprint-prepared nanopillar arrays as the basis for the fabrication of vertically oriented nanocoax arrays.[19] For the imprint masters, we used SiNP arrays prepared as above. We used SU-8 photoresist for the nanopillar replicas for its relatively low glass transition temperature and volume shrinkage coefficient and its wide range of operating temperatures. After fabricating nanocoax arrays as ESs, we used them to explore the effect of the working-counter electrode gap on the Faradic current of the device.

Figure 1 depicts SEM images of a representative SiNP master and SU-8 replica. To form arrays of nanocoaxes, the first step is

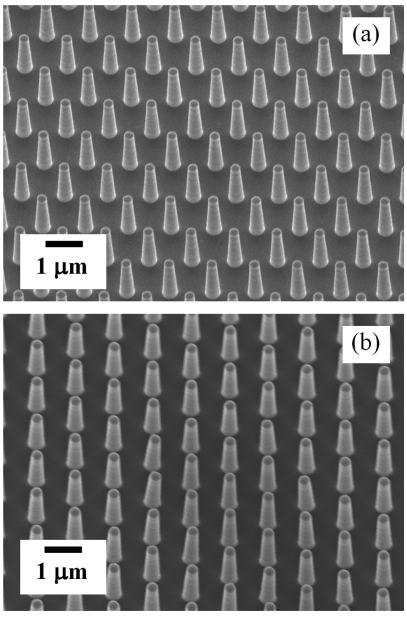

Figure 1. SEM images of arrays of (a) 2 μm tall Si nanopillars of period 1.3 μm prepared via lithographic techniques followed by chemical etching for use as a master for imprinting and (b) SU-8 replica of the master made using a PDMS mold.

metallization of the SU-8 NPs, to serve as the coax cores. After this initial metallization, we deposited a dielectric layer to function as the coax annulus, followed by a second metal deposition to act as the coax shield. To use the coax structure as an ES, the top part of the outer metal was removed by polishing, exposing the dielectric core. These arrays were further processed by partially wet etching the annuli of the coaxes to open a cavity between the coax inner and outer electrodes, into which an analyte solution can ultimately fill and

dx.doi.org/10.1021/ac402441x | *Anal. Chem.* 2013, 85, 10040−10044

be detected, as depicted in Figure 2. Further fabrication details can be found in the Supporting Information.

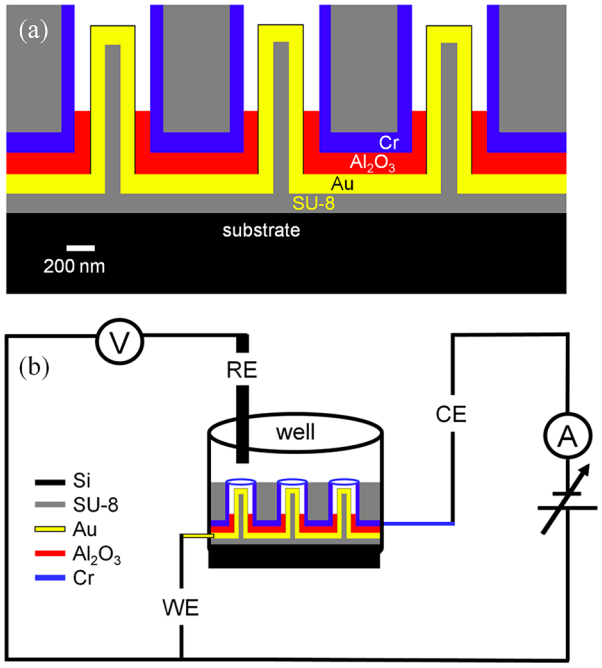

Figure 2. Schematic representations of (a) a partially hollowed nanocoax array and (b) a coax-based ES made using inner and outer electrodes of the coax array as WE and CE, respectively, of an ES.

We sputter-deposited 120 nm of Au for the metallization of the SU-8 nanopillars. To improve conformality of the coating, we used conical rather than strictly vertical nanopillars, as shown in Figure 1. For the dielectric layer, we deposited aluminum oxide (Al_2O_3) of defined thickness, typically 100 to 400 nm, by ALD. In ALD, trimethylaluminum is used as the organometallic precursor with a 200 °C deposition temperature. Next, a Cr film of ∼150 nm thickness was sputtered as an outer metal to form the nanocoaxial structure. Depending on pillar height, the horizontal thickness of the metal on the walls of the conical pillars typically ranged from 1/3 to 1/2 that of the vertical thickness of the metal at the base between pillars.

Before polishing, an important consideration is structural support for the nanocoaxes in the arrays. This was provided by coating the array with a second SU-8 stabilizing layer, filling the space between coaxes to a thickness comparable to or greater than the height of the array. Mechanical polishing was then performed using suspensions of Al_2O_3 nanoparticles on a vibratory polisher. Polishing/SEM inspection cycles continued until the outer metal on the top of coaxes was fully removed, thus exposing the Al_2O_3 annuli. The dielectric in the annulus was removed by wet etching with Transetch-N solution at room temperature, yielding a cavity of ∼500 nm vertical depth into the annulus. Figure 3 shows SEM images of nanocoax arrays of 1.3 μm pitch, 200 nm annulus thickness, and ∼500 nm annulus depth, as well as a cross-sectional view of a portion of an array obtained by FIB milling. We have fabricated similar arrays with annulus thickness ranging from 100 to 400 nm to investigate the effect of electrode separation on subsequent ES performance.

After fabrication, arrays of coaxes were isolated using a custom-made polypropylene gasket to create a reservoir for

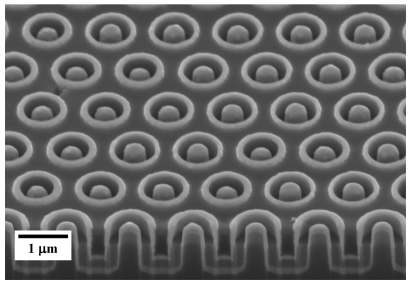

Figure 3. SEM image of an array of partially hollow nanocoaxes of 1.3 μm pitch, 200 nm annulus thickness, and 500 nm annulus depth with Au inner and Cr outer electrodes. Bottom portion shows a cross-section of one row of the array prepared by FIB milling.

liquid on top of the arrays. The reservoir (or well) was filled with a redox reagent, 1 mM ferrocene carboxylic acid (FCA) in phosphate buffered saline (PBS). A three-electrode ES was then configured by using the inner and outer coax electrodes as the WE and CE, respectively, and a Ag/AgCl electrode immersed in the reservoir as a reference electrode (RE), as shown in Figure 2. For comparative study, we also constructed an ES with a planar Au WE, Pt CE, and Ag/AgCl RE (not shown), which had the same projected WE area as the coax arrays (1.8 mm^2).

For analytical purposes, DPV was employed as the electrochemical measurement technique. A factor which plays an important role in reducing the background charging current in pulse techniques, especially at higher measuring speeds, is the *RC*-time constant of an electrochemical cell. This is defined by the factor R_uC_d, where R_u is the uncompensated resistance, and C_d is the double layer capacitance. The maximum value of uncompensated resistance of an electrolyte solution of conductivity σ, confined between two electrodes separated by a distance d, is $R_u = d/\sigma A$, where A is the area of the inner electrode. There is an electric double layer capacitance density C_d due to the charged species and oriented dipoles at the metal−solution interface, whose typical value is in the range of 10−40 μF/cm^2.[5] For a physiological solution such as PBS of bulk conductivity 0.14−0.18 S/m,[26] the value of uncompensated resistance R_{ui} for a nanocoax with 250 nm diameter inner electrode, 200 nm annulus width, and 500 nm annulus depth is $R_{ui} \sim 3$ MΩ. The number of coaxes within a 1.5 mm diameter array area is $n \sim 1.2 \times 10^6$. For resistive analysis, coax arrays can be treated as a parallel combination of n resistors, with an equivalent resistance $R_u = R_{ui}/n \sim 1$ Ω. For such arrays, we calculate the value of the double layer capacitance to be $C_d \sim 0.1$ μF. With these values, the cell *RC*-time constant of a nanocoax ES within the 1.5 mm diameter area employed is $\sim 10^{-7}$ s. For comparison, the *RC*-time constant of a planar cell with the WE and CE separated by mm-scale distance is $\sim 10^{-3}$ s.

Following the standard practice of using a DPV pulse time ∼10 times greater than the *RC*-time constant, the coax-based ES reduces the limit of the experimental time scale to 10^{-6} s (1 μs) for the commonly used biological medium PBS. Such a rapid time scale could only be achieved for other microstructures by using a medium with high electrical conductivity.[27] Thus, the low value of the time constant of the coax-based ES provides the unique ability to study voltammetric signals in media with low conductivity. In principle, an ES with a time of ∼1 μs can also be used to measure the redox potentials of highly reactive intermediates and the rate constant of rapid

dx.doi.org/10.1021/ac402441x | *Anal. Chem.* 2013, 85, 10040−10044

heterogeneous charge transfer, as well as to analyze complex mechanisms including chemical steps.[28−32]

To observe the effect of electrode (WE−CE) separation on Faradic current, DPV measurements were carried out using initial and final potentials of 0.0 and 0.5 V, respectively, pulse size of 50 mV, pulse time of 0.05 s, step size of 2 mV, and sample period of 0.1 s, for the redox chemical 1 mM FCA in PBS. Measured values of coax-based ESs with different electrode gaps (coax annulus widths) are shown in Figure 4,

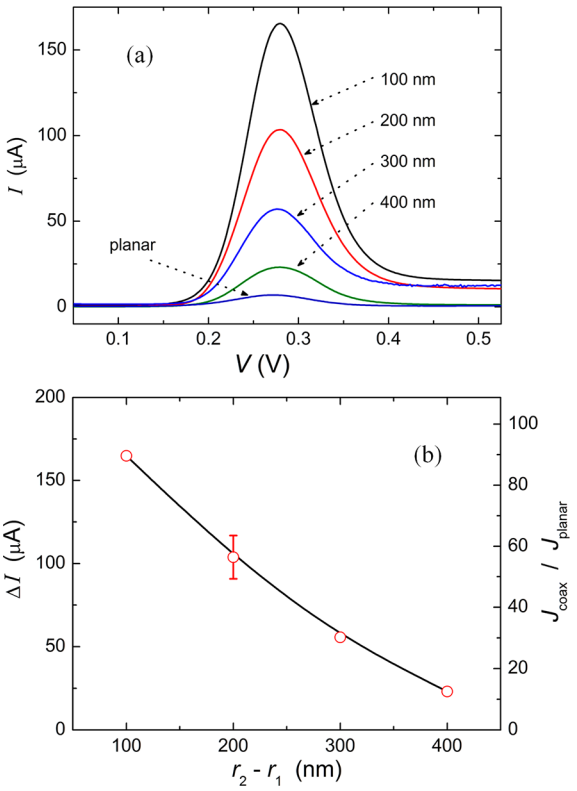

Figure 4. DPV signal from different annulus thickness, coax-based electrochemical sensors. (a) Current in nanocoax-based ES with 100 to 400 nm gaps between WE and CE, plotted vs. WE potential. Data for a planar ES control having millimeter-scale WE−CE gap is also shown. (b) Left axis: Difference between peak current and current at 0.1 V WE potential vs. gap (r_2−r_1) between WE and CE for nanocoax-based ES. Right axis: Ratio of current density in coax-based ES cell to that in planar ES vs. gap between WE and CE of nanocoax-based ES.

as well as results for the planar WE cell. Figure 4a shows that all coax and planar ESs had a well-defined peak at 280 mV vs. (Ag/AgCl), which corresponds to the redox reaction of FCA. The width of the peak at half height for all curves is $\delta I_{1/2} \sim 92$ mV, close to a previously reported value of 90.4 mV[33,34] for a one electron process at 25 °C. However, in all cases, the coax-based devices displayed higher current than the planar control. In Figure 4b, we show the dependence of the peak value of the current on the coax-based WE−CE separation $d = r_2 - r_1$, where r_1 is the outer radius of the inner coax conductor and r_2 is the inner radius of the outer coax conductor. For consistency of measurement for all values of electrode separation, we subtracted the background current at 0.1 V from the peak current value, indicated as ΔI in Figure 4b. This is less than a 1% effect on the overall result. The current at d = 200 nm is the average of three identically prepared ES arrays, with the error bar indicating the standard deviation. As anticipated, the value of the peak current increases inversely with decreasing distance between electrodes. This can be explained by assuming a linearly varying concentration gradient of the redox molecules within the diffusion layer between the two electrodes. Under this condition, current can be expressed[5] as $I \sim (r_2 - r_1)^{-1}$. The ratio of current density for the coax-based ES to that for the planar device is also shown in Figure 4b. The coax-based ES with 100 nm electrode gap is seen to have a signal nearly 2 orders of magnitude greater than that of the conventional, planar ES (i.e., $J_{coax}/J_{planar} = 90$), while the noise level in each ES is approximately the same.

We suggest that the observed improvement in signal-to-noise ratio in the coax-based ES compared to the planar ES, and with decreasing electrode gap in the coax-based ES, is due to two effects: rapid diffusion of redox species between the closely spaced electrode surfaces and the large number of nanocoaxes in our device. The small gap between the WE and CE facilitates efficient diffusion of redox molecules between electrodes, with the result that species reduced at the counter electrode rapidly return back to the working electrode and vice versa, providing positive feedback to the signal.[35−37] This process presents a large flux of redox species between electrodes, which yields a higher value of current compared to a sensor with a large electrode gap. The small dimensions of each nanocoax and their close spacing is such that each 1.5 mm diameter ES device contains more than 10^6 nanocoax ESs operating in parallel (whose signals are thus additive). Also, in this coaxial structure, the inner electrode is circumferentially surrounded by the outer electrode, such that molecules always diffuse radially (i.e., horizontally) between the electrodes. In combination, this means that we are within the linear diffusion regime such that the electrochemical processes are not mass diffusion limited, a problem found in other nanogaps ES devices.[8] This is evidenced by a conventionally shaped cyclic voltammogram (not shown), in contrast to peak-shaped curves in the planar-diffusion dominated nanodevices.[8]

While our devices are in array form, one can employ smaller subarrays or even individual coaxes as a micro- or nanoscale ES, after electrically addressing each coax or subarray. Such a device could then be employed, for example, to map variations in local concentration of the brain-signaling molecules in vitro/silico/vivo, which could be more facile and sensitive than the traditional manner of monitoring the concentration of the molecules using ultramicroelectrodes.[38] In addition, with further development to incorporate microfluidics for liquid exchange, the coax device could be developed into a cost-effective, portable device for rapid molecular analysis in broader applications such as environmental monitoring of chemicals and toxins, pathogen detection, and biomarker detection for the diagnosis of human disease, such as early stage cancer. As the open volume (in the hollow annulus) of each nanocoax is ~50 aL, very small analyte volumes could be employed (e.g., 1 fL for a 5 × 5 coax array).

CONCLUSION

In conclusion, we have demonstrated a novel fabrication method for arrays of nanocoaxes using replicated arrays of silicon nanopillars in polymer, prepared by a stamp imprint technique. We modified the arrays to obtain arrays of open-ended, partially hollow nanocoaxes, with the coaxes' inner and outer electrodes serving as working and counter electrodes of a nanoscale electrochemical sensor. The width of the coax annulus controls the distance between electrodes in the sensor.

dx.doi.org/10.1021/ac402441x | Anal. Chem. 2013, 85, 10040−10044

An observed increase in electrochemical signal with decrease of electrode distance (annulus width) is due to improvement in molecular diffusion, which depends inversely on electrode gap, robust radial diffusion ensured by the cylindrical geometry, and the high site density of nanoscale electrochemical sensors in the device. These result in a ∼100× signal enhancement of the nanocoax over that of planar ES having millimeter separation between electrodes. Such a coaxial architecture can be employed to increase sensitivity of a range of electrochemical sensors, including label-free biosensors.

■ ASSOCIATED CONTENT

Supporting Information

Additional information as noted in text. This material is available free of charge via the Internet at http://pubs.acs.org.

■ AUTHOR INFORMATION

Corresponding Author

*E-mail: naughton@bc.edu. Fax: 617-552-8478.

Notes

The authors declare no competing financial interest.

■ ACKNOWLEDGMENTS

This work was supported by the National Institutes of Health (National Cancer Institute award No. CA137681 and National Institute of Allergy and Infectious Diseases award No. AI100216). Assistance from Dr. Gregory McMahon for FIB milling is acknowledged.

■ REFERENCES

(1) Oja, S. M.; Wood, M.; Zhang, B. *Anal. Chem.* **2013**, *85*, 473−486.
(2) Li, T.; Hu, W. *Nanoscale* **2011**, *3*, 166−176.
(3) White, R. J.; White, H. S. *Langmuir* **2008**, *24*, 2850−2855.
(4) Singh, K. V.; Whited, A. M.; Ragineni, Y.; Barrett, T. W.; King, J.; Solanki, R. *Anal. Bioanal. Chem.* **2010**, *397*, 1493−1502.
(5) Bard, A. J.; Faulkner, L. R. *Electrochemical Methods*, 2nd ed.; Wiley: New York, 2001.
(6) Mirkin, M. V.; Fan, F. R. F.; Bard, A. J. *J. Electrochem. Soc.* **1992**, *328*, 47−62.
(7) Broers, A. N.; Lean, E. G.; Hatzakis, M. *Appl. Phys. Lett.* **1969**, *15*, 98−101.
(8) Li, T.; Su, L.; Hu, W.; Dong, H.; Li, Y.; Mao, L. *Anal. Chem.* **2010**, *82*, 1521−1526.
(9) Montelius, L.; Tegenfeldt, J. O.; Ling, T. G. I. *J. Vac. Sci. Technol.* **1995**, *13*, 1755−1760.
(10) Zhang, H.; Chung, S.-W.; Mirkin, C. A. *Nano Lett.* **2003**, *3*, 43−45.
(11) Fischbein, M. D.; Drndic, M. *Nano Lett.* **2007**, *7*, 1329−1337.
(12) Gazzadi, G. C.; Angeli, E.; Facci, P.; Frabboni, S. *Appl. Phys. Lett.* **2006**, *89*, 173112−1−173112−3.
(13) Nagase, T.; Kubota, T.; Mashiko, S. *Thin Solid Films* **2003**, *438*, 374−377.
(14) Johnston, D. E.; Strachan, D. R.; Johnson, A. T. *Nano Lett.* **2007**, *7*, 2774−2777.
(15) Park, H.; Lim, A. K. L.; Alivisatos, A. P.; Park, J.; McEuen, P. L. *Appl. Phys. Lett.* **1999**, *75*, 301−303.
(16) Chen, F.; Qing, Q.; Ren, L.; Wu, Z.; Liu, Z. *Appl. Phys. Lett.* **2005**, *86*, 123105−1−123105−3.
(17) Kim, J. H.; Moon, H.; Yoo, S.; Choi, Y. K. *Small* **2011**, *7*, 2210−2216.
(18) Jung, M.; Song, W.; Sung Lee, J.; Kim, N.; Kim, J.; Park, J.; Lee, H.; Hirakawa, K. *Nanotechnology* **2008**, *19*, 495702.
(19) Rizal, B.; Ye, F.; Dhakal, P.; Chiles, T. C.; Shepard, S.; McMahon, G.; Burns, M. J.; Naughton, M. J. In *Nano-Optics for Enhancing Light-Matter Interactions on a Molecular Scale*; Di Bartolo, B., Collins, J., Silvestri, L., Eds.; Springer: Dordrecht, Netherlands, 2013; pp 359−370.
(20) Rybczynski, J.; Kempa, K.; Herczynski, A.; Wang, Y.; Naughton, M. J.; Ren, Z. F.; Huang, Z. P.; Cai, D.; Giersig, M. *Appl. Phys. Lett.* **2007**, *90*, 021104−1−021104−3.
(21) Naughton, M. J; et al. *Phys. Status Solidi-RRL* **2010**, *4*, 181−183.
(22) Paudel, T.; Rybczynski, J.; Gao, Y. T.; Lan, Y. C.; Peng, Y.; Kempa, K.; Naughton, M. J.; Ren, Z. F. *Phys. Status Solidi* **2011**, *A208*, 924−927.
(23) Zhao, H.; Rizal, B.; McMahon, G.; Wang, H.; Dhakal, P.; Kirkpatrick, T.; Ren, Z.; Chiles, T. C.; Naughton, M. J.; Cai, D. *ACS Nano* **2012**, *6*, 3171−3178.
(24) Choi, J.; Kenichi, S.; Kato, T. *Surf. Interface Anal.* **2010**, *42*, 1373−1376.
(25) Xia, Y.; Whitesides, G. M. *Annu. Rev. Mater. Sci.* **1998**, *28*, 153−184.
(26) Phosphate buffered saline 1×; Catalog No. BP2438-20; Fisher Scientific: 300 Industry Drive, Pittsburg, PA.
(27) Forster, R. J. *Chem. Soc. Rev.* **1994**, *23*, 289−297.
(28) Engstrom, R. C.; Weber, M.; Wunder, D. J.; Burgess, R.; Winquist, S. *Anal. Chem.* **1986**, *58*, 844−848.
(29) Robinson, R. S.; McCurdy, C. W.; McCreery, R. L. *Anal. Chem.* **1982**, *54*, 2356−2361.
(30) Sun, P.; Mirkin, M. V. *Anal. Chem.* **2006**, *78*, 6526−6534.
(31) Zevenbergen, M. A. G.; Wolfrum, B. L.; Goluch, E. D.; Singh, P. S.; Lemay, S. G. *J. Am. Chem. Soc.* **2009**, *131*, 11471−11477.
(32) Bi, S.; Liu, B.; Fan, F. R. F.; Bard, A. J. *J. Am. Chem. Soc.* **2005**, *127*, 3690−3691.
(33) Koehne, J.; Li, J.; Cassell, A. M.; Chen, H.; Ye, Q.; Ng, H. T.; Han, J.; Meyyappan, M. *J. Mater.Chem.* **2004**, *14*, 676−684.
(34) Parry, E. P.; Osteryoung, R. A. *Anal. Chem.* **1965**, *37*, 1634−1637.
(35) Wipf, D. O.; Bard, A. J. *J. Electrochem. Soc.* **1991**, *138*, 469−473.
(36) Fan, F. R. F.; Bard, A. J. *Science* **1995**, *267*, 871−874.
(37) Fan, F. R. F.; Bard, A. J. *Science* **1997**, *277*, 1791−1793.
(38) Lama, R. D.; Charlson, K.; Anantharam, A.; Hashemi, P. *Anal. Chem.* **2012**, *84*, 8096−8101.